Integrated terahertz systems for satellite applications

Esam Yousef O Zafar

Submitted in accordance with the requirements for the degree of
Doctor of Philosophy

The University of Leeds
School of Electronic and Electrical Engineering

January 2021

The candidate confirms that the work submitted is his own, except where work which has formed part of jointly authored publications has been included. The contribution of the candidate and the other authors to this work has been explicitly indicated below. The candidate confirms that appropriate credit has been given within the thesis where reference has been made to the work of others.

The waveguide-integration concept and described in Chapter 5 and LOCUS system payload have been published in B. N. Ellison *et al.*, '3.5 THz quantum-cascade laser emission from dual diagonal feedhorns', *International Journal of Microwave and Wireless Technologies*, vol. 11, no. 9, pp. 909–917, Nov. 2019. Associated conference proceedings are detailed in the List of publications. B. N. Ellison, O. Auriacombe, N. Brewster, and M. L. Oldfield, designed and fabricated the waveguide structure, which was analysed and simulated by E. Zafar. Y. Han, and L. H. Li developed the QCL source; D. Gerber, G. Savini, M. Emes, B. Winter, D. Walker and E. Saenz developed the satellite system design; E. H. Linfield, A. G. Davies, and A. Valavanis led the QCL development and contributed to characterisation and analysis of the data.

Acknowledgements

First and foremost, I would like to thank my PhD project supervisors, Dr Alexander Valavanis and Dr Paul Dean, for providing me with continuous guidance and support throughout. I would also like to express my sincere gratitude to Prof. Edmund Linfield, for his valuable guidance, advice, and important comments and assistance given in supervision meetings from my second year until the last period of my program. Thanks, are also due to Prof. Giles Davies for his important comments and feedback given in the annual meetings. I would also like to thank Dr Mark Rosamond and Dr Chris Wood for their organisation and operation to run the cleanroom smoothly. My thanks also extend to Dr Yingjun Han and Dr Mohammed Salih for their assistance and guidance with various fabrication techniques throughout my project. All the work that has been done for my project in the cleanroom became achievable due to the training and help from Dr Li Chen. Wafers of material through my project have been gratefully supplied Dr Lianhe Li. I would like to thank THz atmospheric & space research team for their support during my project. I cannot forget to thank Sue Hobson for her administrative help and support. I would like to thank my friends in the United Kingdom, Dr Mansour Alharthy, Dr Raed Alsofyani, Marwan Farrash, Bandar Alkhozaim, Salih Alghamdi, Nawaf Alhulian, and Majed Elenezy who provided me with positive energy and constant motivation throughout my study. Special thanks to my brothers Hazim and Ameen and my sister Nada, my friends Yahia, Hamza, Samer, Zaher, Amer, Abdulrahman who, despite their remoteness, were my support and help to overcome all the moral and psychological difficulties and challenges and were one of the main reasons for my success. To my soulmate and partner in my path, who endured a lot for me and created all the right conditions for me so that I could achieve my aspiration, thank you my wife. Lastly, I would like to thank my parents for all their help and support.

Abstract

Terahertz technology has numerous potential applications in trace-gas analysis, and in atmospheric and space research. A new Earth observation system satellite concept, ‘Keystone’, has been proposed, which aims to explore and study the distribution of key gas species in the Earth’s upper atmosphere using terahertz-frequency (THz) heterodyne spectrometers, based upon quantum cascade lasers (QCLs) as compact, yet powerful local oscillators (LOs).

In this work, THz QCLs have been fabricated and characterised, in both semi-insulating single plasmon and double metal waveguides. Their performance has been assessed against the requirements for a spaceborne LO in terms of power, operating temperature, and their spectral resolution. Improvement of the output power and operating temperature has been achieved through the development of a high reflectivity coating applied to the QCL rear facet, and a silver-based waveguide.

The second part of this work focuses on the integration of the QCLs with other components of the THz detection system. This has been done through electromagnetic-field analysis of a THz QCL integrated with a mechanically micro-machined waveguide cavity and diagonal feedhorn. A hybrid finite-element/Fourier transform approach enables analysis of both the near-field and far-field regions and is shown to agree well with experimental observations. The far-field antenna patterns show enhancement of the beam profile when compared with an unmounted QCL, in terms of beam divergence and side-lobe suppression ratio. Furthermore, we demonstrate integration of the QCL with dual diagonal feedhorns, enabling simultaneous access to both facets of the QCL, underpinning future integration with a satellite-based receiver and frequency-stabilization subsystem.

List of publications

The following journal article, and associated conference proceedings were produced during the course of this study.

[1] B. N. Ellison *et al.*, ‘3.5 THz quantum-cascade laser emission from dual diagonal feedhorns’, *International Journal of Microwave and Wireless Technologies*, vol. 11, no. 9, pp. 909–917, Nov. 2019.

[2] E. Zafar *et al.*, “Electromagnetic modelling of a terahertz-frequency quantum-cascade laser integrated with dual diagonal feedhorns,” presented at the 2019 Infrared Terahertz Quantum Workshop (ITQW 2019), Ojai, California, USA, Jul. 2019, Accessed: Oct. 05, 2020.

[3] E. Zafar *et al.*, “Electromagnetic-field analysis of diagonal-feedhorn antennas for terahertz-frequency quantum-cascade laser integration,” in *2019 44th International Conference on Infrared, Millimeter, and Terahertz Waves (IRMMW-THz)*, Sep. 2019, pp. 1–2.

[4] A. Valavanis *et al.*, “Development of Terahertz Quantum-Cascade Lasers for Satellite-Borne Measurement of Key Gas Species,” in *2019 Conference on Lasers and Electro-Optics (CLEO)*, May 2019, pp. 1–2.

[5] B. N. Ellison *et al.*, “3.5-THz quantum-cascade laser emission from dual diagonal feedhorns,” in *12th European Conference on Antennas and Propagation (EuCAP 2018)*, London, UK, 2018, p. 248 (4 pp.)-248 (4 pp.).

[6] E. Zafar *et al*., “Quantum-Cascade Laser emission at 3.5 THz from dual diagonal feedhorns,” in *UK Semiconductors* 2018, 4–5 Jul 2018, Sheffield, UK.

Table of contents

List of Figures

List of Tables

List of abbreviations

- BTC Bound-to-Continuum
- CSL Chirped Superlattice
- CW Continuous Wave
- DFB Distributed Feedback
- DFG Difference Frequency Generation
- DM Double Metal
- EOS Earth Observing System
- EM Electromagnetic
- FDS Frequency-Domain Spectroscopy
- FEM Finite-Element Method
- FFT Fast Fourier Transform
- FTIR Fourier Transform Infrared
- FTS Fourier Transform Spectroscopy
- HERO Heterodyne Receiver for the Origins Space Telescope
- HFSS High-Frequency Structure Simulator
- HR High Reflectivity
- IF Intermediate Frequency
- IPA Isopropyl Alcohol
- LEO Low-Earth Orbit
- LIV Light–Current–Voltage
- LO Local Oscillator
- LOCUS Linking Observations of Climate the Upper Atmosphere and Space weather
- LO phonon Longitudinal-Optic phonon
- MBE Molecular-Beam Epitaxy
- MLS Microwave Limb Sounder
- MLT Mesosphere and Lower Thermosphere
- NEO Near-Earth Orbit
- QCL Quantum-Cascade Laser
- QW Quantum Well
- RP Resonant Phonon
- SI-SP Semi-Insulating Surface-Plasmon
- TDS Time-Domain Spectroscopy
- TE/TM Transverse Electric/Magnetic
- UV Ultraviolet
- WCE Wet-Chemical Etching

Chapter 1

Introduction

Terahertz radiation is a band of the electromagnetic spectrum that has frequencies in the far-infrared range from 0.3–10 THz. The wavelength of such radiation varies between 1 mm and 0.03 mm, and hence it also known as sub-millimetre waves [1]. Distinct THz spectral signatures are observed in a considerable number of materials in the solid and gaseous phases, which underpin a wide range of potential applications [1]–[3].

Owing to its location in the electromagnetic spectrum, which exist between the infrared and the microwave radiation as shown in Figure 1.1, THz radiation has some notable properties. In common with mm-waves, THz waves can penetrate non-metallic materials such as paper, plastic, clothing, and ceramic. However, the relatively short wavelength allows higher resolution imaging [3], [4]. This feature makes it potentially suitable for security applications, such as surveillance at airports, to detect weapons, drugs, and explosives.

Another characteristic of THz wave is that it is potentially safer than *x*-rays as it is non-ionising due to the low photon energy (1 THz ~ 4 meV). In addition, THz waves are absorbed strongly by water and hence penetrate only a small distance into living tissues [3]. Therefore, biomedical applications can potentially benefit from THz waves to discriminate between tissue types, and identify diseases, e.g. skin cancers, with better tissue contrast when compared with *x*-rays, and better imaging resolution than microwaves [5].

THz waves potentially offer ultra-fast information transfer rates for short-range communications, where it can be used as a signal carrier with rates up to terabits per second, owing to the frequency range ~1000 times higher than microwave transmission [3].

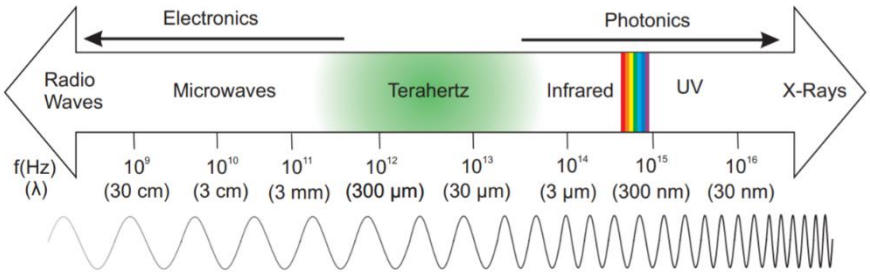

Figure 1.1 Electromagnetic spectrum. Image adapted from [6]

Nevertheless, THz technology remains in its infancy, when compared to the microwave and infrared, due to the gap in use of the existing conventional electronic and optical devices to generate and detect frequencies in that range. Electronic oscillators are limited to less than 1 THz owing to the need for very short transit time that leads to the need for small device areas to reduce the capacitance of the device [7]. On the other hand, the concept of the diode lasers cannot be extended into the mid-infrared regime, because

the light is generated by the recombination of electrons in the conduction band and holes in the valence band across the bandgap of the active material. The bandgaps of conventional semiconductors are more than 1THz therefore low energy photons (mid-IR or THz) cannot be generated through interband transitions [7]. The engineering of THz laser devices is also challenging, as the required separation of energy levels (~10 meV) is small, and thermal excitation of carriers can easily prevent a population inversion from being achieved. Thus, the discovery of reliable THz sources was a significant challenge, and that required new mechanisms, components, and devices to be developed.

Historically, 1975 was the year that witnessed the development of the first compact THz emitter, which is the photoconductive terahertz antenna [8]. Further improvement and optimizations have been applied on the device in terms of the electrode structure and semiconductor substrate [9], [10], which resulted in a rapid advancement of THz technology. By taking advantage of such devices, the capability to generate terahertz emission became more reliable in the 1980s with the emergence of femtosecond lasers. In addition, the field of THz science has been spurred positively by the rapid development of THz quantum cascade lasers (QCLs) since their first demonstration in 2002 [2].

Therefore, the generation and detection of the THz radiation has progressed tremendously in the last decade [11], which, in turn, led to an acceleration of research into potential THz applications.

In this thesis, THz QCLs are exploited for their potential application in satellite-born studies of atmospheric gases. This chapter introduce the core scientific and technical concepts that underpin this study.

1.1 THz sensor technology

THz gas sensing applications have one of two typical system configurations: either as active or passive sensing, as shown in Figure 1.2. In active sensing, THz radiation from a radiation source is directed onto a sample that need to be analysed or studied, and then into a detector. The number of these parts and their arrangements might vary based on the application purposes and objectives [12]. Passive sensing is typically based on a heterodyne detection system, in which the measured signal results from mixing an incoming radio frequency signal with a local oscillator (LO). Passive sensing is used in applications such as astronomy and has potential applications in mapping of atmospheric emission spectra as will be explained later in this chapter.

The focus of this work will be on terahertz sources, with an emphasis on the THz quantum cascade laser (THz QCLs), which is described in detail in the following chapter. In addition, terahertz components and detectors will briefly be discussed to understand the overall context of the THz system.

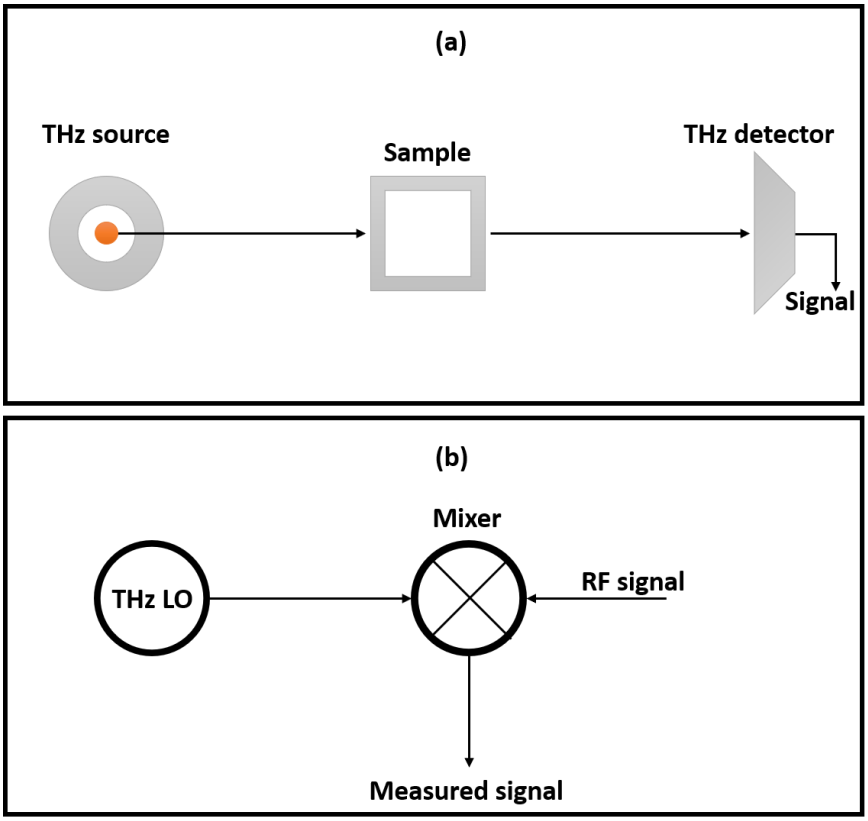

Figure 1.2 Typical THz gas spectroscopy configurations. (a) Active sensing for applications such as imaging, spectroscopy and others [12]. (b) Passive sensing for applications includes heterodyne detections such as astronomy.

1.1.1 THz sources

There are many natural sources of terahertz radiation starting with the thermal blackbody radiation emitted by all objects in the universe. The spectrum of these emissions is determined by the temperature of the object, with THz frequencies being obtained from objects with temperature range between10 K and 100 K, such as the cold dust and gas clouds in the interstellar medium [1], [13], [14]. Passive, remote sensing systems in atmospheric and astronomical systems aim to detect and analyse these natural spectra and detect signatures of key constituent gases.

Blackbody emitters are also used in the simplest and most common laboratory-based THz sources, in which radiation is produced through heating [12]. More advanced approaches are needed though, for high-precision remote sensing, and a range of THz sources have been developed based on solid-state electronic devices, optical THz generation, and THz quantum cascade lasers [15], [16].

1.1.1.1 Solid-state electronic devices for THz applications

Solid-state electronic THz sources are typically based on classical oscillations of charge within a device. The frequency of the emitted radiation corresponds to the charge oscillation frequency, and as such is limited by the transient time for charge transport. In practical devices, the capacitance and

size of the device results in the amplitude of the emitted frequency rolling-off rapidly at frequencies >1 THz [13]. However, the efficiency of high-frequency electronic devices has been continuously improved. Frequency conversion techniques are commonly used, in which frequencies are either up-converted from millimetre-waves [17]–[19], or down-converted from the infrared bands [13], [16]. One promising solid-state electronic sources is the Gunn diode [20]–[23] which yields a frequency range between 0.2 THz and 0.8 THz. Although though the Gunn diode is small and portable and can be manufactured with low cost, it has poor temperature stability and high-power dissipation due to the high operating current. For applications in which high speed switching is required such as in amplifiers and oscillators, another type of solid-state electronic source is used based on high-frequency transistors [24]–[28].

Visible or near-infrared lasers may also be used to produce terahertz radiation by optical pumping, either working continuously or in pulsed mode. Frequencies in the terahertz range can be obtained by mixing two continuous visible or near-infrared lasers such as diode lasers, dual-mode lasers, multi-mode lasers [12]. Photomixers are based on the periodic THz generation of free carriers of electrons and holes in semiconductors through the absorption of two laser beams [29], this interface would modulate the intensity of the laser beam in THz frequency, so that:

$$\boldsymbol{w_{\mathrm{THz}} = |w_2 - w_1|} \qquad (1.1)$$

The photomixer approach can provide continuous THz generation with precise tuning by adjusting w_1 and w_2. However, low output power in the microwatt range is produced from conventional photomixer designs based on low-temperature-grown GaAs (LT-GaAs) grown on GaAs substrates as absorbing regions. The output power of the photomixer is mainly limited by the increase in the temperature of the device due to the combination of optical and Joule heating localised near the surface of the device. An alternative photomixer design has been proposed to enhance the magnitude of continuous-wave THz generation using a metamaterial approach to generate THz powers in the milliwatt range [30].

1.1.1.2 Broadband THz sources

Broadband sources generate THz radiation by using ultrashort laser pulses to excite an emitter, either by photoconduction or optical rectification [15]. An ultrafast photocurrent is generated in a high-speed photoconductive switch or semiconductor based on the carrier acceleration by an electric field within the material [15], [16], where the bandgap energy of the material is smaller than the photon energy of the laser pulses ($E_{\mathrm{g}} < hv$). Thus, a recombination of electron–hole pairs will occur inside the photoconductor. A transient photocurrent will be formed from the acceleration of the free carriers which will cause electromagnetic radiation [15]. Alternatively, THz radiation can be generated by optical rectification, where the radiation is limited by the excitation of the femtosecond laser [16]. Although the resulting output power

by this method is less than that of photoconductors, a high bandwidth up to 50 THz can be achieved by using such approach [15]. These sources are widely used in THz time-domain spectroscopy.

1.1.1.3 Narrowband THz sources

Over the past century, the development of narrowband sources has accelerated research in THz technology remarkably, due to its significant number of applications including high-resolution spectroscopy, telecommunications, and high bandwidth inter-satellite links. Their development typically depends on the conversion techniques that are mentioned in the solid-state electronic devices part [15]. Extensive details and reviews about these techniques are available in [13], [31] . One of the promising techniques for narrowband THz sources is the use of semiconductor lasers, which depends on the population inversion between the energy gaps of the semiconductor [15]. Fundamentally, the lasing can be achieved due to the electrons decay from the conduction band to the valence band, which lead to a photon emission. Thus, the band gaps of the semiconductor material are what identifies the wavelength of the emitted photon, and they can be changed widely based on the used material [32]. However, practical materials such as GaAs have $E_g > 1\ \mathrm{eV}$, and as such the emission wavelength is in the infrared or visible band and this interband transition approach cannot be used to generate THz radiation. Nevertheless, semiconductor lasers have significant advantages, due to their distinctive properties including the small size of the active laser itself, their capability to be integrated with other semiconductor devices, and the ability to alter the output of the laser by adjusting junction current. Additionally, the operational requirements for semiconductor lasers are very low, with small terminal voltages, and relatively high power efficiencies (up to 80% for infrared diode lasers) [32].

An alternative approach, enabling long-wavelength emission is the Quantum Cascade Laser (QCL), which is based on electronic transitions between closely spaced energy levels within the conduction band, rather than across the bandgap. The QCL was first demonstrated at mid-infrared wavelengths in 1994 [33], and subsequently at THz frequencies in 2002 [34]. These sources are extremely attractive for satellite-based applications, owing to their relatively high output power, electrical efficiency, and compact size. As such, the systems developed in this thesis are based around QCL technology. Chapter 2 discusses the functionality of the QCLs, their operational methods, fabrication, and performance in detail.

1.1.2 THz optical components and interfaces

In addition to the generation and detection of THz radiation, it is essential to direct, focus and couple radiation between components without introducing excessive dispersion or loss [12]. Microwave systems typically use metallic waveguides to guide and couple radiation, whereas infrared systems typically use fibres, lenses, and mirrors. However, in the THz band, both approaches

have limitations because many of the materials used for visible and infrared optics are opaque or have strong resonances at THz frequencies. The relatively short wavelength of THz radiation leads to the requirement for extremely small, precision-machined waveguides. As such, a significant part of the research in this thesis relates to the development of suitable THz waveguide technologies for use in satellite applications, and the analysis of THz emission. These are discussed in detail in Chapter 5.

A range of THz optics have been developed to date. Mirrors are conventionally made of metals with other emerging materials having been tested such as doped and undoped GaAs [35] and a hybrid of polypropylene and high-resistivity silicon [36]. Other optical elements such as lenses have also been developed over the years, starting with the traditional THz lenses based on plastic, to the less conventional lens designs such as grooved-dielectric Fresnel zone plates [37], plasmonic-resonance lenses based on gold and silicon [38], adjustable focal length lenses [39] and other types that have been developed recently including dielectric lenses, silicon lenses and artificially fabricated metal lenses [3].

1.1.3 THz detectors

Terahertz detectors convert THz signals into an electrical signal that can be analysed and investigated based on the application purposes. Before immersing into the development history of THz detectors, it is important to highlight some important characteristics that affect the detection performance for any detector. These characteristics can be either interaction properties with the received signal, or properties based on the practical construction and operation [40].

Bandwidth and frequency resolution: Every detector has a specific frequency range, and only THz radiation in that range can be received by the detector. This range known as the spectral range or the spectral bandwidth, and it is determined by the detector sensitivity to photons of the received terahertz frequencies. The frequency resolution is a measure of the ability to distinguish between photons of different frequencies. Certain detection methods have an intrinsically high spectral resolution, while others need to be coupled with further frequency-selective components. Detectors with narrow frequency band are preferable for some applications, while for others the responsivity to a wide frequency band is more adequate [40].

Noise: Practically, the incident signal to the detectors is usually disturbed with background fluctuations, and additional noise is introduced (e.g., thermally) within the detector itself. As such, the output signal is contaminated with undesired noise [40]. This can be expressed by the signal-to-noise ratio (SNR), in which the level of the original signal is being compared to the level of background noise.

Responsivity: The responsivity of the THz detectors is determined based on the magnitude of the output signal as an electrical potential difference that is stated by the input of the THz signal. This can be expressed as the following:

$$\boldsymbol{R_V} = \frac{\mathbf{d}\boldsymbol{V}}{\mathbf{d}\boldsymbol{P}} \tag{1.2}$$

$$\boldsymbol{R_I} = \frac{\mathbf{d}\boldsymbol{I}}{\mathbf{d}\boldsymbol{P}} \tag{1.3}$$

which means that either a change of voltage in volts or current in amperes relative to the change of power in watts defines the responsivity, and it is more desirable to have large value of the responsivity [40].

Response time: The simple definition for the response time of the detector is the period that the detector needs to response to the THz radiation to produce a correlated output, which depends on the existence of a constant terahertz radiation either continuous or interrupted pulses. The time constant that is needed to obtain the output would be the fraction of $(1 - 1/e)$ of the final output [40].

Coherence: Coherent detection schemes are sensitive to the phase of the received THz radiation and are needed for interference measurements, while incoherent detection is only sensitive to the magnitude of the incoming THz signal. The purpose of the application would determine which scheme is desirable.

Polarization: Like the coherence property, some detectors are sensitive to the polarization of the incoming THz signal. in other words, some detectors are sensitive only to either the vertical or the horizontal polarisation of the THz radiation, so that it will only detect signal with the same polarity. Some detectors are not intrinsically sensitive to the polarization and might use a polarizing element before it to detect the desired polarity.

Linearity: Generally, a linear detector is preferable over a nonlinear one for direct power measurements, as there is a linear relationship between the output and input ($\mathrm{d}V/\mathrm{d}P = V/P,\ \mathrm{d}I/\mathrm{d}P = I/P$) [40].

Practical properties: There are other characteristics that can state the practicality of the detectors in terms of its operation and construction. Most of these properties would depends on the application and how they are being used.

For example, the size of the detectors is preferred to be small for most applications, which implies that detectors are also preferred to be portable. This means that such detectors do not need special environmental conditions to be operated and hence do not require special operating procedures [40]. However, for other applications, the size of detectors might be large, and the operating environmental conditions are considered, in which the range of conditions such as temperature, pressure and humidity would limit the operation of the detector. Similarly, the requirement for the power supply for some detectors might be high. There are other characteristics that also affect the practicality of the detectors such as the mechanical robustness, lifetime, and ease-of-use. A last significant property is the expenses of purchasing and

operating the detector, which would depend on all the previous characteristics that have been mentioned above [40].

The bolometer is one of the earliest THz detectors in which its operating principle depends on the change in electrical resistance with temperature. Bolometers require a cryogenic environment to operate [12], [40], which provides high sensitivity and low noise, makes it suitable for applications that required high resolution detection.

Another detector that is also based on a thermometric property of a material is the Golay cell, in which the intensity of the received radiation is measured by the expansion of a gas in a flexible chamber based on a change in the temperature. Such detectors are distinguished by its capability to operate at room temperature. Despite that, this would limit its detectivity due to the thermal fluctuation and the response time is relatively slow [40].

Pyroelectric detector is also another type of the thermal detectors, in which the polarisation of the pyroelectric materials depends on the change on the temperature of the absorbed heat. The electric field across opposite faces of the pyroelectric material is being changed when temperature of the absorbed heat is increased. and this changing is being monitored by using dielectric material inserted in a capacitor, and hence the electrical signal will be generated in the form of current based on the magnitude of the temperature and the coefficient of the pyroelectric material. more details about the implementations and metrology of the pyroelectric detector can be found in [40].

Another thermal detector based on a microelectromechanical systems (MEMS) are also being developed to provide more sophisticated detection, which discussed in detail in [41]–[43].

THz detection can also be achieved using a non-linear electronic device, such that a THz optical field induces a direct current as well as a set of harmonics in the current through the device. To rectify terahertz radiation in this way, the Schottky diode is the most common device being used, which consist of a metal-semiconductor junction. the operation of such detectors at room temperature are extremely fast, and they are appropriate for narrowband applications such as astronomy, makes suitable for the proposed satellite payload in this thesis.

For some applications, the source that produce the THz radiation act at the same time as a detector, such as in self-mixing imaging applications, in which the emitted THz radiation is backscattered from the target and reinjected into the laser cavity, this would change the operation of the source and hence change the amplitude and the phase of the feedback signal. A recent development in self-mixing terahertz imaging based on a pulsed-mode terahertz quantum cascade laser has been demonstrated, in which the QCL works as a source and detector at the same time [44].

1.2 THz spectroscopy systems

Terahertz spectroscopy can be systematically divided into two analytical methods: frequency domain spectroscopy (FDS), or time domain spectroscopy (TDS), which can both be used to analyse the optical properties of the materials [15], [16]. Moreover, high-resolution FDS methods can probe the energetic structure of molecules and atoms [45]. A wide range of potential applications have been proposed including within biological, medical and pharmaceutical sciences, security, astronomy, climate meteorology, and other semiconductors and industrial applications [15], [16].

1.2.1 THz time-domain spectroscopy (TDS):

THz-TDS is the most widely used THz spectroscopy technique for broadband measurements. The operating principle of THz-TDS, shown in Figure 1.3, depends on utilising short pulses of broadband THz radiation [15]. To do that, an ultrafast laser is used to provide femtosecond pulses. The laser radiation is then split into two signals by a beam-splitter. The first signal is used to pump a THz emitter to generate short THz pulses, which are directed onto a sample and then into a THz detector. The detector measurement is gated by the second part of the femtosecond laser beam, providing an instantaneous measurement of the THz electric field [15]. An optical delay between the pump and the probe beam is used to repeatedly sample the THz field, and hence provide an accurate time-domain plot of the THz pulse. The THz spectrum can be obtained by taking a Fourier transform of this pulse. In this respect, the detector in the system is not able to operate independently of the source, and the system can only stand by considering a connection between both. Such technique gives rise to the concept of the THz transceiver [46]–[49].

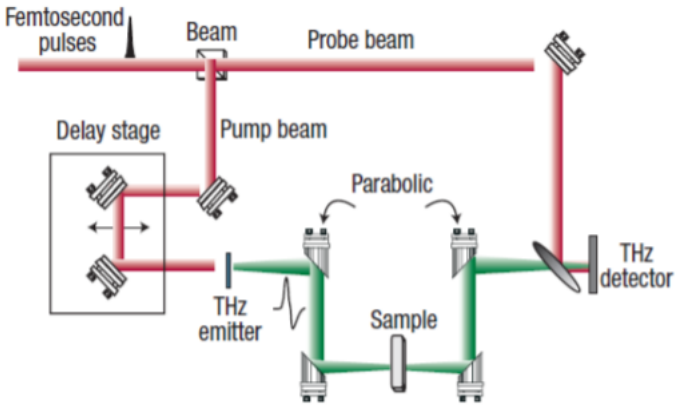

Figure 1.3 Schematic of a THz-TDS pump probe system. Reproduced from [15].

THz radiation is therefore generated and detected coherently by using such system [1], [15], [50], which results from the use of ultrafast lasers to synchronise the measurement [50]. TDS is therefore resilient against background noise [50]. However, the spectral content of the signal is strongly

affected by reflections and overlaps between the THz pulses and thus signal processing is often needed to improve the measurement [15], [50].

Wider spectral range can be achieved by Fourier transform spectroscopy (FTS), which could obtain material characterization from THz frequencies to fit into the infrared due to its wide bandwidth feature [15].

The operation of a typical far-infrared FTS system is based on two-beam interferometry. An incoherent high-pressure mercury arc lamp (broadband thermal source) is used to illuminate the sample, this far-field illumination is then divided into two equal parts using a far-infrared beam splitter [15], [51]. The first part of the signal comes from the first arm of the optical interferometer system, where the sample is located, that has a fixed transmission coefficient and phase shift. The second part comes from the second arm of the interferometer which has a varied path length that can provide a changeable phase of $2\pi f\Delta$, where Δ is the path length of the arm. The interference between these two signals is detected by a thermal detector. A data acquisition system is then used to apply Fourier transform on the signal to get the power spectra density of the sample [15], [51]. FTS techniques have the advantage of not requiring synchronisation between the THz source and detector. As such, there is no need for a costly femtosecond laser, and the technique can be used with *any* kind of THz source. Indeed, this method is used in this work to perform Fourier Transform Infrared (FTIR) measurements of QCL spectra, whose emission characteristics are unknown. It is also used in astronomical measurements, where the THz source is a distant astronomical object.

Nonetheless, the spectra resolution for both FTS and TDS techniques is limited by the length of the optical delay stage, and the spectral power density of the sources is typically very low, meaning that transmission spectra can only be acquired for thin, weakly absorbing samples.

1.2.2 THz frequency domain spectroscopy (FDS)

THz-FDS is frequently used to observe and record the thermal emission lines of molecules, mostly in astronomy applications.

Heterodyne spectroscopy can be utilised at the THz frequency to achieve high spectra resolution. This is essentially based on the intermediate frequency (IF), which can be acquired from the difference between two different sources of frequencies, through a non-linear element to get frequency in GHz range. Remote sensing in astronomy or atmospheric research is considered as the most important applications for the heterodyne spectroscopy. In addition, the Earth's atmosphere and planetary atmospheres and comets can be investigated significantly by THz heterodyne receivers. To do that, the main signal that needs to be analysed, from an astronomical source, for example, is subtracted from the reference signal that is generated by a local oscillator (LO) [45].

THz heterodyne receivers are designed based on two main subsystems, which are the front-end and the back-end subsystems as shown in Figure 1.4 [52]. The front-end subsystem deals with coupling the incoming THz radiation signal and a reference frequency generated by the LO into the mixer. This provides the IF because of the subtraction between the incoming signal and the LO frequencies. Some heterodyne receivers utilise optical components, such as beam splitter, to couple the incoming signal with LO radiation before directing it to the mixer, while others, such as in our satellite payload mission, couple these signals directly with the mixer using waveguides. The down-converted IF signal is then dealt with in the back-end subsystem using two main components, which are an IF processor to amplify the signal that generated by the mixer, and a spectrometer to study and analyse the IF signal.

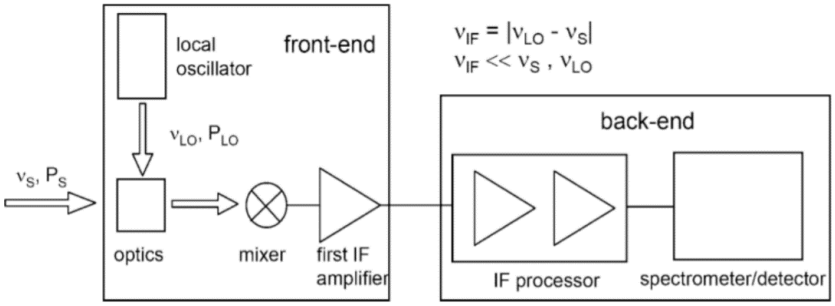

Figure 1.4 Simplified diagram of THz heterodyne receiver subsystems in which an optical component (such as a beam-splitter / combiner) is used to direct the incoming signal and the LO radiation toward the mixer. Reproduced from [52].

Heterodyne technique has two distinctive aspects that makes it suitable for its uses at THz frequencies. First, the ability to use low-frequency amplifiers owing to the down-conversion technique for the incoming signal, which makes it even appropriate to be used at very high-frequency to overcome the lack of high-speed amplifiers in which the direct amplification is not possible. Moreover, choosing the bandwidth of the detection similar to the signal bandwidth would help to reduce the noise.

The key elements of the front-end are the mixer and the LO, which both require specialised components at THz frequencies. The most widely used mixers in such systems are Schottky diodes due to their strong non-linearity and their operation in narrowband range.

Furthermore, there are some important requirements that the LO must have it to be suitable to work as a THz source. This thesis is concerned with the development of satellite-based instruments, in which components must have low mass, volume and power consumption. More generally, a THz LO needs to be tunable and have linewidth less than that of the detected signal. Finally, it must be able to provide enough power to operate the mixer. All these requirements can be achieved by using a THz quantum cascade laser as the

LO. One of the objectives of this work is related to the QCL to enhance device THz performance as will be discussed later.

1.3 THz radiometry and its application

Terahertz sensing technology is of great importance in astronomy and atmospheric research. For example, the spectra of interstellar dust clouds have their principal features between wavelengths of 1 mm to 100 µm. Additionally, about 98% of the emitted photons in galaxies are located within the range of the submillimetre- wavelength and far-infrared spectrum. This has been demonstrated by observing the spectral distribution of the residual energy from the big bang [13], [31]. Therefore, the interstellar medium, including the dust, light, and heavy molecules within the cold and dark regions, can be observed unobstructed with THz measurements [11].

Moreover, key gases within the atmospheres of Earth, and other planets and objects in the solar system have distinctive spectral signatures [11]. Within the Earth's atmosphere, for example, the temperature and chemical composition of the Mesosphere and Lower Thermosphere (MLT) are strongly responsive to the ozone depletion and greenhouse gases, which implies that analysis of MLT gas species can be a highly sensitive indicator of global climate change effects [53].

A range of spaceborne THz sensors have been used for atmospheric and astronomical measurements. These have been in different orbits and combined with other associated payloads. The altitude range of between 160 km and 2000 km, known as Low Earth orbit (LEO), is often used as it is easily reachable and enables global measurements to be undertaken [11].

Additionally, THz space observation missions, e.g. WMAP [54], Herschel [55] and Planck [56], have been located at Lagrangian points [57] to provide adequate and stable observations.

Usually, the size of the satellites vehicles is relatively large and would require high budget to launch, and hence the mass and volume of these satellites need to be essentially minimised [11]. In addition, such payload resources are usually powered by solar panels, and strictly limited to a few Watts per instrument in most applications that are associated with in situ planetary sounding and near-Earth object (NEO) rendezvous such as Juno-MWR [58] and Rosetta-MIRO [59]. Moreover, a multi-year hibernation period might be required for some applications before reaching the destination of the spacecraft mission [11].

Therefore, scientific research and commercial interests have been supported by the development of the THz spaceborne payloads over the years. A simple example is weather forecasting, which is fed by data that is collected from continuous monitors based on THz sensors [11].

The main concepts of the new THz missions are that they required continuously phase coherence, signal correlation systems, and low cost using a mixture of semiconducting and superconducting sensors in order to provide

advanced Earth observation systems, and hence study the indicators of climate change by performing a global mapping of atmospheric species [11], [60]. Moreover, providing highly compact and power efficient instrumentation are also required for the deep space planetary [61] and NEO probes to cover a wider range of the existing global weather monitoring services and enhance it with wider frequencies bands, radiometric sensitivity and calibration accuracy [62]. Other aspects that need to be taken in consideration for the satellite missions' components are the reproducibility, longevity, and payload compliance with rapid small satellite deployment. Thus, the development of next generation spaceborne THz payloads encounter substantial challenges that need to be fulfilled prior to the approval for any scientific or commercial applications, these challenges include operational frequency, sensitivity, component durability, system integration; signal processing and support infrastructure. All that must be examined through stages of demonstration to check the performance and test their technical predisposition [11].

The operational objectives for any THz spaceborne deployment would depends on the purposed application and determined by the sensing methodology, which is divided into two main detection methods: coherent and incoherent detection as shown in Figure 1.5. The core instrumentation characteristics for each of these are defined by using an appropriate sensor and a correlated system design. Incoherent detection is preferable for applications that require broad spectral response, while coherent and heterodyne sensing is appropriate for purposed applications of high-resolution spectroscopy [11].

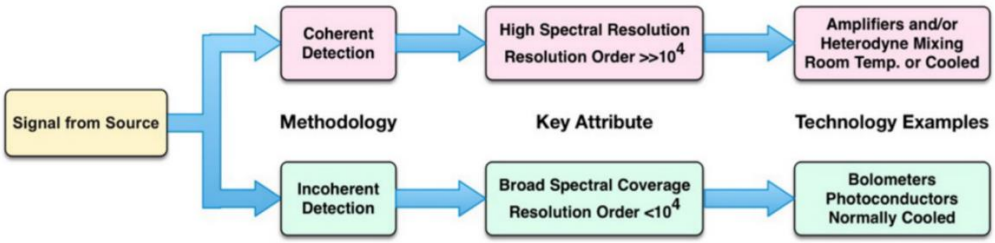

Figure 1.5 Sensing methodologies and their related selection path. Reproduced from [11].

Additionally, with the high frequencies, these challenges are even greater due to the need to miniaturise the THz components to minimise parasitic effects that might limit the sensor response and sensitivity. Thus, material properties of the sensor such as carrier velocity, dielectric effects, and resistive losses must be taken into consideration. For astronomy, there are more challenges that need to be addressed including advanced mechanical machining to ensure optimal integration for the system components and hence optimum signal matching. Lightweight composites, and improved cooling technologies are other aspects that also considered with the evolution of the THz detectors to ensure more operational technical enhancements [11].

To ensure further minimisation of the mass and volume of the system, the optical components must be implemented in a compact form, this includes mirrors, frequency selective surfaces, polarisers, and precision calibration mechanisms. Another considerable challenge includes the reduction of the consumed power by increasing the speed of the digital sampling, which means the need to enhance the signal-processing system. In addition, the realisation of state-of-the-art payload technology would require mechanical micro-miniature fabrication techniques which will be explained later in Chapter 5.

1.4 Proposed Earth-observation satellite payloads

THz receivers can be used to measure distinctive spectral “fingerprints” for several key gas-phase species, and as such there is strong interest in developing satellite payloads for atmospheric research. One example of this is the potential for measuring the distribution and variation of gas concentrations in the Mesosphere–Lower Thermosphere (MLT) region of the Earth’s atmosphere, which lies at 50–150-km altitude [63]. This is considered, in some respects, as the gateway area between the Earth’s atmosphere and the near-space environment, and its chemical composition is believed to be high responsive toward climate change effects. The MLT is composed mainly of atomic oxygen (O) in the lower mesosphere and hydroxyl radicals (OH) in the centre of the layer [63], [64]. In addition, nitric oxide (NO) results from interactions between the radiation and energetic particles from the Sun and molecules of oxygen and nitrogen within the lower thermosphere are also affected by climate processes [64]. Moreover, there are other gases within the MLT that can be considered as indicators of climate change, such as carbon monoxide (CO), ozone (O_3), and water (H_2O) [63]. Studying the MLT species could therefore provide considerable information regarding climate change phenomena in the Earth’s atmosphere, and quantitative inputs to atmospheric models [63], [64]. These trace gases have distinctive spectral features within the THz band, (i.e. H_2O, O_3, O_2, NO, CO) with a wavelength range from sub-millimetre up to THz [65]. 4.7 THz and 2.1 THz are the two emission lines of the atomic oxygen, while the OH emission lines are 2.5 THz and 3.5 THz [65].

Atmospheric sensing of such species has been very limited, due to the lack of compact, and robust satellite-compliant THz sensor instrumentation [53]. However, a range of Earth Observation systems (EOS), based on THz sensing technology, have been developed and proposed for this purpose [11], [16]. For example, in 2004, the EOS Aura satellite included a Microwave limb sounder instrument (EOS-MLS) [66]. THz fingerprints gases have also been found by utilising high-resolution lab-based heterodyne radiometer systems at frequencies ranging approximately between 0.1 THz and 2.5 THz [13], [16].

A new EOS satellite concept, ‘Keystone’, has been proposed. This was formerly known as LOCUS (‘Linking Observations of Climate, the Upper Atmosphere and Space weather’) [53], [60]. This satellite payload aims to undertake a global mapping of key species within the MLT, using a set of THz heterodyne receivers (see Section 1.2.2) [63], [65]. These will use QCLs as

LOs along with infrared filter radiometers to undertake limb-sounding of the atmosphere at regular intervals in a sun-synchronous orbit, and low Earth orbit over an altitude between about 80 km and 120 km [63], [65].

The first THz QCL worked as LO was part of GREAT (the German Receiver for Astronomy at Terahertz Frequencies) in 2014, when it became operational on board of SOFIA (the Stratospheric Observatory for Infrared Astronomy), The main objective of SOFIA is to study the atmospheres of the solar system and beyond at mid-and far-infrared wavelengths by gathering data about planets, comets and asteroids and to examine the chemical composition of the interstellar medium [67], [68]. The development of the LO has been carried out afterward, and the LO capability to pump seven hot-electron bolometric mixers has been achieved in 2016. SOFIA now uses these LOs routinely, in which the platform of the system is based on heterodyne spectroscopy, where the QCL is used as a compact LO that provides sufficient output power to pump the hot-electron bolometer which is used as a mixer [69]. Furthermore, QCL is considered to be used as LOs for other balloon or spaceborne missions, such as GUSTO (the Galactic/Extragalactic Ultra long Duration Balloon Spectroscopic-Stratospheric Terahertz Observatory), FIRSPEX (the Far Infrared Spectroscopic Explorer for probing the lifecycle of the interstellar medium), and HERO (the Heterodyne Receiver for the Origins Space Telescope) [69]. These high-level missions at the horizon underpins the development of LOs based on THz QCLs by improving their operational performance, and overcome technical issues related to the space adequacy.

The concept of the Keystone/proposed satellite THz payload, as shown in Figure 1.6, consists of four heterodyne THz receivers, which downconvert the frequencies that are received from a Cassegrain telescope antenna mounted on an aluminium optical bench by subtracting them from QCL LOs through a Schottky barrier diode mixer [63], [65]. A closed-cycle cooler is used to cool down the temperature of the THz receivers to below 100 K, to enable operation of the QCLs. Then, the signal is amplified, and by filtered to provide the intermediate frequency (IF) from each receiver. The power spectrum of the incident signal is then measured with 1-MHz spectral resolution by sampling the IF through a wideband fast Fourier transform spectrometer (FFT) [61],[63].

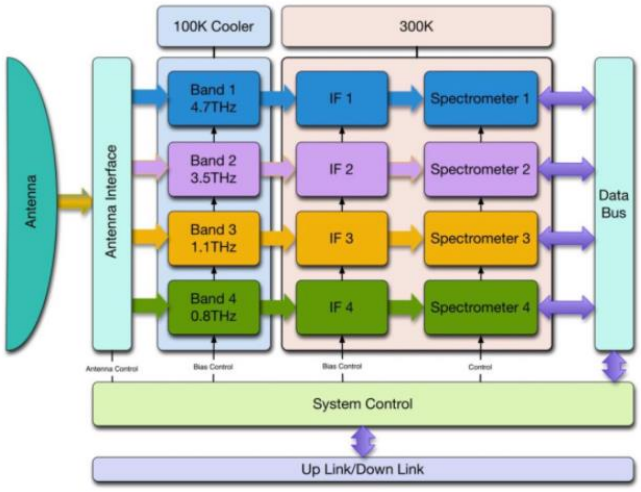

Figure 1.6 Stage's layout of LOCUS THz receiver [63].

1.5 Project objectives and thesis structure

While QCLs currently considered as an efficient compact THz source that could provide high power and tunable source of radiation, some of the system requirements still need to be achieved to be suitable for satellite applications including improvement on the operating temperatures, sufficient power, and an appropriate integration system.

Therefore, the aim of the work described in this thesis is to produce desired performance and single mode emission from THz QCLs for satellite applications. It also includes proposing a suitable waveguide design that will be used to integrate the QCL with other system components in a satellite mission. Chapter 2 presents the fundamental theory of the laser technology and the waveguide structures and designs followed with the basics of the quantum well heterostructure lasers. Then, the functioning of the QCLs has been described along with a brief review on the THz QCLs and their designs. Chapter 3 describes the general fabrication methods for both semi-insulating single plasmon and double metal QCLs. It is also describing the characterisation techniques used to test the fabricated devices. Chapter 4 describes two techniques used to optimize the performance of the THz QCLs in terms of operating temperature and power. Chapter 5 investigates the electromagnetic field of the THz QCL through a proposed diagonal feedhorn waveguide design that will be used to integrate the QCL with other system components in a satellite mission, which is done by analysing the propagation through it. Chapter 6 summarises the results obtained from the previous chapters and outlining future work.

Chapter 2

THz Quantum Cascade Lasers

This chapter explain the theory behind the development of the laser by explaining the fundamentals of the laser technology and the waveguide structures and designs. From that, an introductory to the quantum cascade laser has been explained through the basics of the quantum well heterostructure lasers. Then, the functioning of the QCLs has been described along with a brief review on the THz QCLs and their designs.

2.1 Introduction to laser technology

LASER is the acronym of the light amplification by stimulated emission of radiation. To understand the working principle, it is important to recall the fundamentals of the atomic energy levels. As we know that electrons move in certain orbits around a positively charged nucleus, and each one of its atomic orbitals has a specific amount of energy. The electrons move faster or change their orbits to a higher-energy one if the atom has absorbed some energy. After a period of time, they lose the same amount of the absorbed energy and return to their lower-energy orbits [70]. In a simple system with two electron energy levels that represents different allowed energy levels in an atom, electrons can response to an incident energy (e.g. photon) in three different ways: *absorption*, in which the incident photon has amount of energy equal to the energy between two levels ($E_{12} = E_2 - E_1$), which will excite the electrons of the atom to move from the ground state E_1 to the excited state E_2 as shown in Figure 2.1(a) [70]. The energy of the photon is given by $E = hc/\lambda$, where h is Planck`s constant, c is the speed of light, and λ is the light wavelength. Thus, the photon can only be absorbed if its wavelength corresponds to the energy-level difference of the atom. Moreover, the atom can also lose energy of the excited state and transferred to other atoms either as a heat, or as a photon that has wavelength correspond to the lost energy. This is caused when an electron of the atom moves from higher energy level to a lower one. The photon can be emitted either spontaneously or it can be stimulated to do that by another photon [70].

In the spontaneous emission, when the electron in an atom absorbs a photon in E_1 and excited to E_2, it stays in the excited state E_2 for a period then spontaneously drops to the lower energy state E_1 and lose the energy as a photon. This period known as the spontaneous lifetime. The spontaneous emission, shown in Figure 2.1(b), happens in a random direction and random time with energy equal to ($E_{12} = E_2 - E_1$) [70].

In stimulated emission, another photon which is identical to the absorbed one induce the electron in the excited level of the atom to move from E_2 to the lower level E_1 during a period shorter than the spontaneous lifetime. This resulted in two photons coming out from the atom which are coherent, implies same amplitude, phase and frequency as shown in Figure 2.1(c).

In order to achieve a net gain, we require to have more electrons in the higher energy level, such that stimulated emission exceeds absorption, i.e., population inversion [70], [71]. However, the population inversion cannot be achieved in a two-energy level system, because the incident photon will cause as many upward excitations as downward stimulated emission. Therefore, this process is usually done in a three-level energy system as shown in Figure 2.1. Here, electrons are pumped either optically or electrically from E_1 to E_3, creating population inversion between E_3 and E_2 or E_2 and E_1.

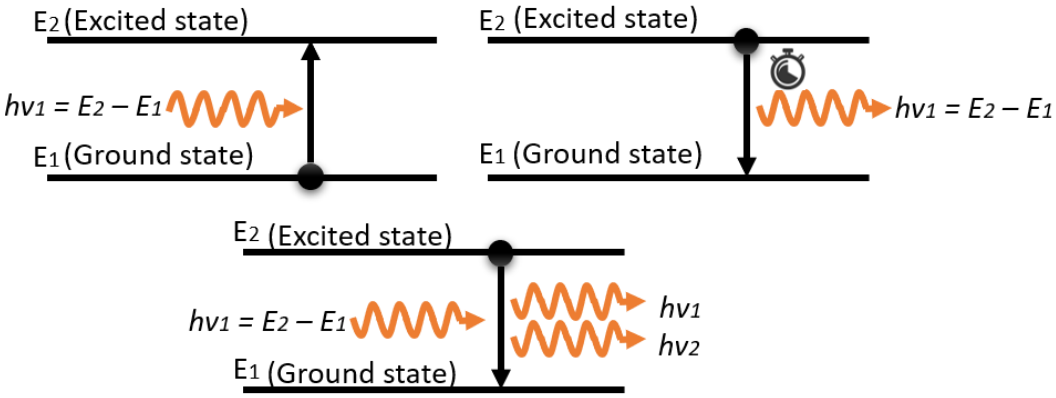

Figure 2.1 Schematic representation of a simple two-level system (a) Electron will absorb the energy of the incident photon and excited to the next level if the photon energy equal $\boldsymbol{E_2 - E_1}$, (b) Electron will drop from the higher energy level to the lower after a spontaneous lifetime and emit a photon with energy equals to $\boldsymbol{E_2 - E_1}$, (c) photon from external source (e.g., optical or electrical) induce the electron to drop to the lower energy level, and therefore resulted in two photons that are coherent ($\boldsymbol{hv_1 = hv_2}$) [70].

In the case of optical pumping, the incoming photons must have energy equal to the difference between the highest and lowest energy levels ($hv_{13} = E_3 - E_1$) to boost the atoms up to level 3, which is known as pump energy level. Electrons in the pump level spontaneously rapidly decay to level 2. Level 2 is known in most lasers as the upper laser level that, where electrons tend to accumulate and causing the population inversion between the upper laser level and the ground state owing to the long spontaneous lifetime of the upper laser level. The stimulated emission will be produced by a photon of one atom that is emitted after a spontaneous lifetime and goes to the neighbouring atom. The repetition of the process with the next atoms will result at the end in coherent photons. This explains the word LASER, because one photon will be amplified to become a large group of photons by the radiation of the stimulated emission [71].

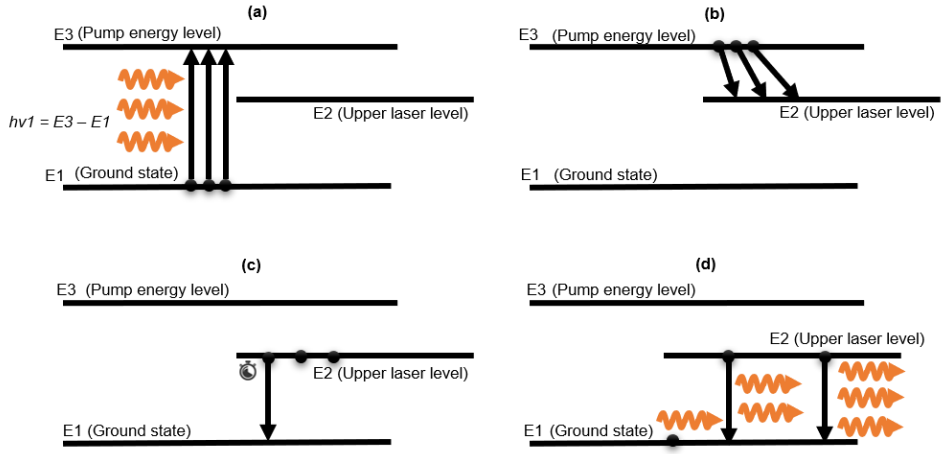

Figure 2.2 Schematic representation of a three-level energy system (a) Electrons are pumped to the pump energy level by incoming energy $\boldsymbol{h\nu_1 = E_3 - E_1}$, (b) Electron will decay from the pump energy level to the upper laser level rapidly and accumulate at this level (c) when one electron decay spontaneously from the upper laser level, it emits photon. (d) the emitted photon will go to the next electron and execute the stimulated emission and the process is repeated [70], [71].

Conventionally in semiconductor lasers, the upper laser level and the ground state are represented in the conduction and valence band respectively as shown in Figure 2.3, and the population inversion occurs when electrons are pumped to the conduction band by external source either electrically or optically. Therefore, the band gap of the material determines the energy of the emitted photon and thus its frequency, and such lasers known as interband lasers [72].

Accordingly, to ensure further stimulated emission is being induced through the material and ensure the lasing process in any lasers, two main design parameters must be achieved, which are: population inversion, and high photon density. To achieve the population inversion between the energy levels of the laser, there are some factors that must be engineered to design the active region properly. These factors are energy levels, wavefunctions and scattering rates of the electrons within the subbands as will be explained later in Section 2.4.1 [73].

The waveguide is required to produce internal reflection and confines the propagated light of the laser within an optical resonant cavity to provide large photon field energy density. This can typically be done by using cladding material, that ensures the reflection of the radiation, and the active material sandwiched between the cladding material, where the radiation is confined.

To get more understanding of the propagation of the electromagnetic wave in optical waveguides, the theory of the concept and main equations are explained in the following section.

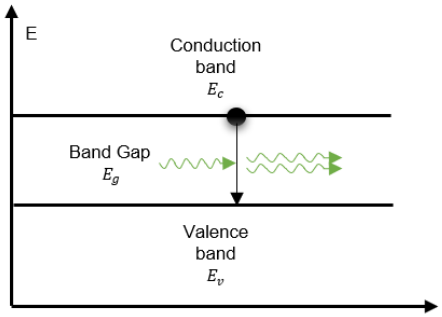

Figure 2.3 Schematic representation of interband transition in a semiconductor laser.

2.2 Waveguide theory and designs

2.2.1 Waveguide structure

In conventional dielectric waveguides, the internal reflection of the electromagnetic field within the waveguide structure occurs only when the radiations of the active material travel in an optically dense medium towards less optically dense medium. In other words, the refractive index of the active material n_1 must be more than the refractive index of the cladding n_0 as shown in Figure 2.4, where generally the refractive index of the material is represented by the ratio between the speed of light in the cladding over the speed of light in the core [123]. When this condition is achieved, we have guided modes in which the wave is repeatedly and constructively reflected between the two interfaces [74], [123]. The total internal reflection can be achieved by obtaining the critical condition as the following:

$$\boldsymbol{\theta_{max} = \theta \leq \sin^{-1}\sqrt{n_1^2 - n_0^2}} \tag{2.1}$$

Where,$\theta_{\max}$ is the maximum acceptance angle of the waveguide, while θ is the incident angle and it is related to the reflected angle ϕ as the following:

$$\boldsymbol{\sin\theta = n_1 \sin\phi \leq \sqrt{n_1^2 - n_0^2}} \tag{2.2}$$

Based on the average of the difference of the refractive index between the active material and the cladding ($n_1 - n_0 \approx 1\%$), we can simplify the equation to be:

$$\boldsymbol{\theta_{max} \cong \sqrt{n_1^2 - n_0^2}} \tag{2.3}$$

Generally, in any optical waveguide, the contrast of the refractive index is measured by the relative refractive index difference between the active material and the cladding as the following:

$$\Delta = \frac{\boldsymbol{n_1^2 - n_0^2}}{\boldsymbol{2n_1^2}} \cong \frac{\boldsymbol{n_1 - n_0}}{\boldsymbol{n_1}} \tag{2.4}$$

and therefore, the maximum acceptance angle related to the relative refractive index difference as the following:

$$\boldsymbol{\theta_{max}} \cong \boldsymbol{n_1}\sqrt{2\Delta} \quad (2.5)$$

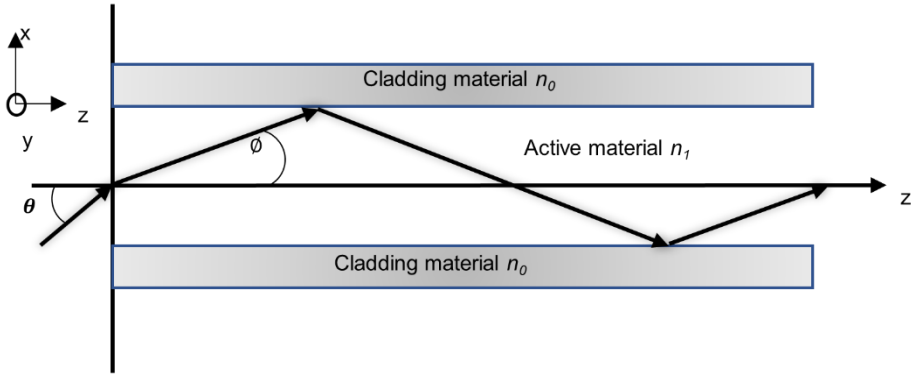

Figure 2.4 Refractive index profile for a basic optical waveguide structure [123].

However, these theories are mostly used for dielectric waveguide where λ of the waveguide is much smaller than the device, and hence it does not work for THz QCLs, and a surface plasmonic layer is required. Since the use of thick dielectric waveguide is inappropriate for THz frequency, using thin metal layer or a highly doped semiconductor layer that adjacent to the active region of the QCL will act as a surface plasmon layer as demonstrated in [75], [76].

Generally, a surface plasmon is defined as excited free electrons that resulted from the coupling between a conducting and dielectric materials, and travel as wave oscillation. In addition, an electromagnetic field that carries energy is trapped at interface, since the plasmon consists of oscillating electric charges.

Fundamentally, the amplified light in lasers can be treated as an electromagnetic field, which consist of two main components that are propagating perpendicular to each other through the space as shown in Figure 2.5 [77]. These components are the electric field $\underline{E}$ and magnetic field $\underline{H}$. The flow of electromagnetic wave is guided in a waveguide structure in which it is confined by cladding materials within the active region of the device and propagate as waveguide modes with specific phase velocity and polarisation along the waveguide [74], [77]. The phase velocity (v_{ph}) or the phase speed is the speed of propagation of the phase of a single frequency component of the travelling wave and can be calculated as the following [77]:

$$\boldsymbol{v_{ph}} = \boldsymbol{f\lambda} \quad (2.6)$$

From here, the phase velocity has a direct relationship with the wavelength which makes it an important parameter for the applications that considering the wavelength as an impact factor such as semiconductor lasers. By contrast, the group velocity is the speed at which a wave packet containing a range of frequency components, propagate through a medium. In general, this can be determined from the dispersion curve of the medium:

$$\boldsymbol{v_{gr}} = \frac{\partial \mathrm{w}}{\partial \mathrm{k}} = \frac{c}{n + w\,\frac{\partial \mathrm{n}}{\partial \mathrm{w}}} \quad (2.7)$$

For a packet of electromagnetic energy travelling along a waveguide with length l in a relatively short time t, it can be calculated as the following:

$$\boldsymbol{v_{gr}} = \frac{\boldsymbol{2l}}{\boldsymbol{t}} \tag{2.8}$$

The group velocity is usually either less than or equal to the phase velocity and in a vacuum waveguide, the relationship between the velocities can be expressed as:

$$\boldsymbol{v_{ph}v_{gr}} = \boldsymbol{c^2} = \boldsymbol{9 \times 10^{16}} \times \frac{\mathbf{m^2}}{s^2} \tag{2.9}$$

In a dielectric waveguide, the group velocity will be affected by the effective refractive index of the waveguide mode.

One of the important distinctions of waveguide theory is the difference between the wavelength in the waveguide λ_g and in the free space λ_0, which is greater in the first because the phase velocity in waveguide is greater than the velocity in free space. Thus, it can be calculated as the following:

$$\boldsymbol{\lambda_g} = \boldsymbol{\lambda_0}\left(\frac{\boldsymbol{v_{ph}}}{\boldsymbol{c}}\right) \tag{2.10}$$

However, in a dielectric waveguide, the wavelength of the travelled waves is reduced by an inverse of the square root of the dielectric constant of the material ($\boldsymbol{\lambda_g} = \boldsymbol{\lambda_0}/\sqrt{\varepsilon_r}$), which makes it travel slower.

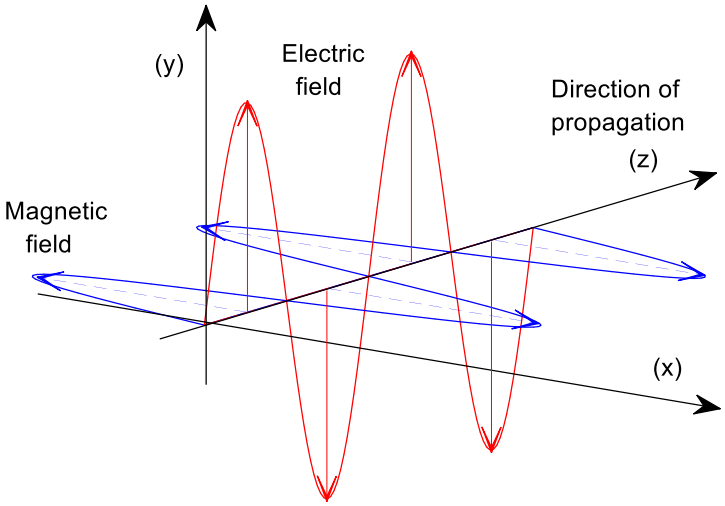

Figure 2.5 The electromagnetic field in the space.

2.2.2 Cut-off frequency and waveguide modes

For each waveguide, there is a minimum cut-off frequency, below which a wave with frequency less than that minimum will not propagate through the guide. this minimum frequency called the cut-off frequency. The QCLs in the keystone receivers will be coupled to the mixer using hollow rectangular metal waveguide. For a rectangular metallic waveguide at specific frequency, the relationship between λ_g and f_c in the air-filled waveguide can be written as:

$$\boldsymbol{\lambda_g = \frac{c}{\sqrt{f^2 - {f_c}^2}}} \tag{2.8}$$

When related to the phase velocity, we can write it as the following:

$$\boldsymbol{v_{ph} = c\left(\frac{\lambda_g}{\lambda_0}\right) = \frac{c}{\sqrt{1 - \left(\frac{f_c}{f^2}\right)^2}}} \tag{2.9}$$

Accordingly, when speaking generally in a complex-number sense, it is evident from this expression that the wave will not propagate if $f < f_c$ because v_{ph} is imaginary.

Since our focus is on semiconductor laser applications, non-planar waveguides are the commonest type used in such applications, specifically the channel/rectangular waveguides [74], [77]. The transverse dimension or the width (a) of such waveguide is greater than the height of the waveguide (b) as shown in Figure 2.6(a).

The transverse dimension relates to the wavelength and the cut-off frequency of the series of rectangular metallic waveguides based on IEEE standard [78] ranges between WM-2540 to WM-86 can be calculated as the following:

$$f_c = \frac{c}{2a} \tag{2.10}$$

$$\lambda_c = 2a \tag{2.11}$$

Thus, this relation states that the maximum transverse dimension of the guide needs to be half the wavelength to ensure the propagation of the wave through the guide. It is important to mention that for the dielectric waveguide, the cut-off frequency is affected by the corresponding dielectric constant ε_r so that the more precise value would be $f_c = \frac{c}{\varepsilon_r} \times \frac{1}{2a}$.

Fundamentally, the classification of modes within the waveguide are determined by the longitudinal field elements, which are [74], [77], [79]:

Transverse-Electric mode (TE): the electric vector of the field in this type is perpendicular to the direction of the propagation as illustrated in Figure 2.6(a).

Transverse-Magnetic mode (TM): the magnetic vector of the field in this type is perpendicular to the direction of the propagation as illustrated in Figure 2.6(a).

Transverse-Electromagnetic mode (TEM): the electric vector and the magnetic vector are perpendicular to the direction of propagation.

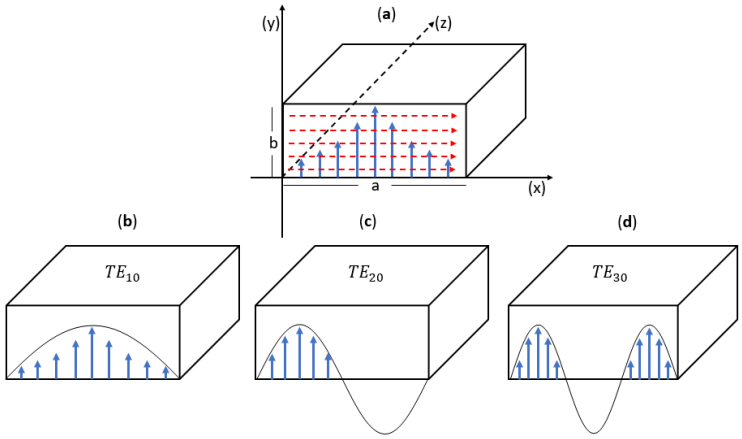

Figure 2.6 Transverse representation of the electromagnetic field in a rectangular waveguide. (a) the blue lines are the electric field, which is perpendicular to the direction of propagation and to the cross-section walls of the guide. The red lines are the magnetic field, which is perpendicular to the direction of propagation and to the side walls of the guide. (b) shows the fundamental mode TE_{10} in the rectangular waveguide, the maximum is in the midway of the cross-section dimension. (c and d) show higher mode in the rectangular waveguide.

The waveguide dimensions determine which modes can propagate through the guide, and for most of the applications that require high precision narrow band signals, a single-mode pattern is the most desirable mode of propagation, in which it can be found just above the f_c and up to $2f_c$ [75], [78]. This mode is usually called the fundamental mode or the dominant mode. In rectangular waveguides, the order of the modes from a single one to higher modes are represented by two suffix numbers (m, n) , which represent the

number of the halves of the wave across the cross-section and the height of the waveguide respectively, and they are written with the modes type such as TE_{mn} or TM_{mn}**.** The dominant mode denoted as TE_{10} because it has only one half-wave across the width and non along the height as shown in 0 (b). It is also worth noting that it is the lowest supported mode within rectangular waveguide.

The representation of the mode as an electric and magnetic field can be expressed as the following [77]:

$$\boldsymbol{E_x(z,t) = E_0 \sin(\omega t - k_z t + \phi_0)} \quad (2.12)$$

$$\boldsymbol{H_y(z,t) = H_0 \sin(\omega t - k_z t + \phi_0)} \quad (2.13)$$

Where, E_0 and H_0 is the amplitude of the mode profile and for TE_{10}, it is maximum at the half of the waveguide cross-section and decreases to zero at the walls. ω is the angular frequency, k_z is the propagation constant or the wavenumber, and ϕ_0 is the phase constant of the wave. According to IEEE standard [78], the suggested waveguide dimensions for frequencies range between 3.3 and 5 THz, which is the frequencies needed for our proposed satellite payload, is 86–57-µm width and 43–28.5 µm height. Therefore, this would require a precision micromachining process, as will be discussed in Chapter 5.

2.3 Quantum well heterostructure lasers

Heterostructures are based on a composition of multiple heterojunctions in which two semiconductors that have different bandgaps are joined [72]. In other words, it made from a thin layer of a semiconductor material *A* with narrow bandgap with width *L* sandwiched between two thick layers materials *B* with wider bandgaps as shown in Figure 2.7 [72]. Hence, electrons are confined and restricted to a finite region, a single quantum well or a particle in box is formed because the potential energy of the electron inside the box equal to zero (PE = 0) and would needs infinite kinetic energy (KE) to escape from the box [71], [72], [80].

Fundamentally, when electrons confined to a certain region ($0 < x < L$), there are two boundary conditions need to be applied: ***Firstly,*** the box boundary condition, in which the wave function $\psi(x)$ vanish at the boundary, so that:

$$\boldsymbol{\psi(0) = \psi(L) = 0} \quad (2.14)$$

$$\boldsymbol{k_m = \frac{\pi n}{L}, n = 1, 2, 3, \ldots} \quad (2.15)$$

Where, k is the wavenumber and equals to $\frac{2\pi}{\lambda}$, λ is the wavelength and by solving the two equations:

$$\boldsymbol{\lambda = \frac{2L}{n}} \quad (2.16)$$

Therefore, the width of the well must be at least half the wavelength of the wavefunction, and this condition only works for a single infinite quantum well as shown in Figure 2.7(a), the energy for such system could be found as the following:

$$\boldsymbol{E_n = \hbar\omega} \tag{2.20}$$

Since the relationship between the frequency and the wavenumber is given by:

$$\boldsymbol{\omega = \frac{\hbar}{2m}\, k^2} \tag{2.17}$$

we substitute this value in equation 2., so we get:

$$\boldsymbol{E_n = \frac{\hbar^2}{2m}\, k^2 = \frac{\hbar^2}{2m}\left(\frac{2\pi}{\lambda}\right)^2} \tag{2.18}$$

Finally, we substitute equation 2.16 to the last one, therefore:

$$\boldsymbol{E_n = \frac{\hbar^2\, \pi^2\, n^2}{2mL^2}} \tag{2.19}$$

where, $\hbar = \frac{h}{2\pi}$, and h is the Planck constant and equals to 6.62607015×10^{-34} J.s, m is the mass of the electron, n is the quantum number of states. Therefore, electrons can only be distributed in certain values of energy states and thus the wider well resulted in close energy states and vice-versa. Thus, the emission energy can be engineered by selection of an appropriate well width.

However, as the transition occurs between conduction band and valence band, the minimum photon energy is equal to the bandgap energy. For GaAs, this limits us to E_{photon} more than 1.4 eV, and therefore wavelength less than 1 µm.

Therefore, THz lasers require a different approach to enable much larger wavelength emission.

Secondly: the periodic boundary condition, in which multiple quantum wells are periodically repeated with the same wavefunction in each system. In this condition, electrons have the possibility to leak out to the next well through the barriers if they are thin enough, which will be resulted in a resonant state rather than bound state. Furthermore, these interactions and coupling of the multi QWs resulting in a something called superlattice, which provides periodic layers of wells and barriers that allow electrons to tunnel and transit from one well to its neighbours through sub-bands [80].

The energy of the emitted photon in this form of lasers is not limited by the semiconductor bandgap because the light amplification process occurs within the conduction band, where a population inversion is generated between different subbands of the superlattice as shown in Figure 2.7(c), which can be tuned by varying the thickness of the wells and barriers. This process known

as intersubband transition and led to the invention of quantum cascade lasers [80].

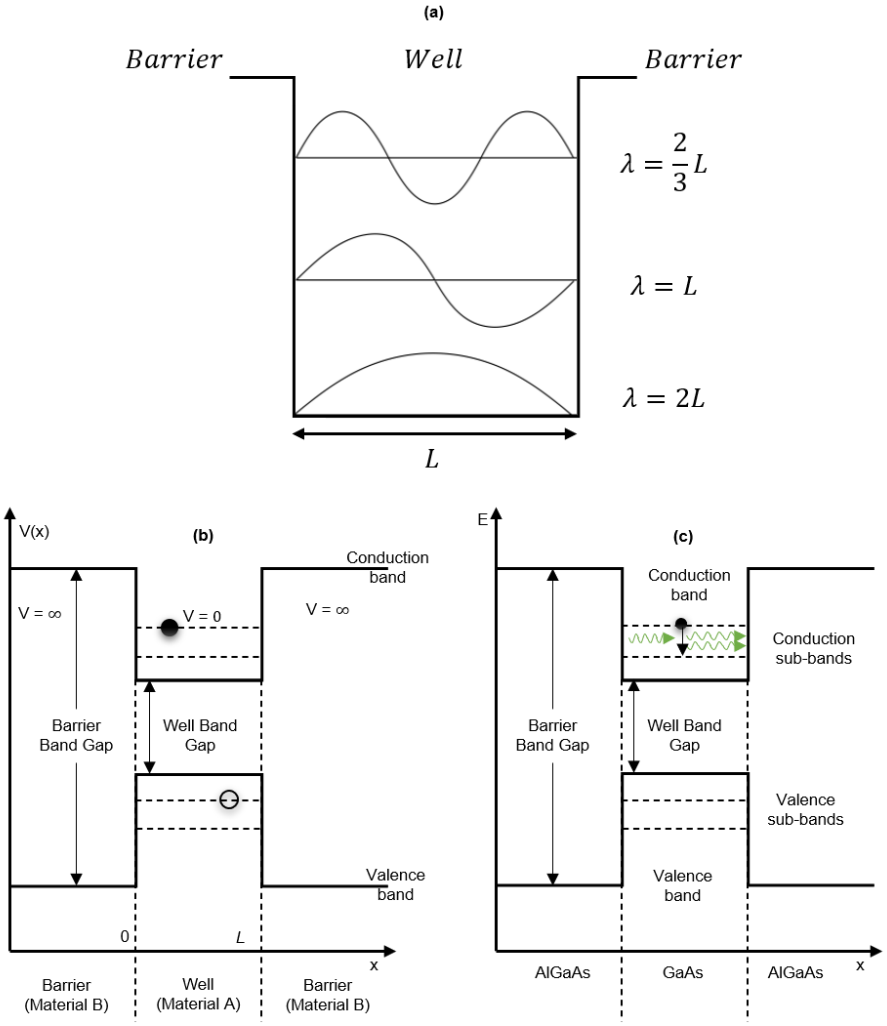

Figure 2.7 Schematic representation of quantum wellsWave functions in a single infinite well for lowest 3 energy levels (b) Infinite Quantum Well with electron trapped within a finite region (c) Energy bands structure in a simple single quantum well based on two materials, e.g., AlGaAs/GaAs. The optical transition of the photons occurs between the conduction sub-bands. Such process known as intersubband transition [72], [80]

2.4 Quantum cascade lasers

The Quantum Cascade Laser (QCL) has been firstly demonstrated in 1994 [33] as a unipolar device based on multi-quantum wells structure from semiconductor materials on nanometre scale. The cascading structure is made up by using Molecular Beam Epitaxy (MBE) that is capable of growing hundreds from repeated quantum wells with good operational high precision quality and long-time stability [81]. The operation of the QCL depends on the electrons transitions between subbands of the multiple Quantum Wells within only the conduction band of the energy bands level, which is known as intersubband transitions as explained previously in Figure 2.7(c) [13], [83].

2.4.1 The functioning of the QCLs

A full operational period of the active region of the QCLs needs at least two QWs as demonstrated in [83], [84]. In addition, three quantum wells are used to have three states in each period, which are: the upper laser level 3 or the injector, the lower laser level 2, and level 1 which is called the extractor state as shown in Figure 2.8. When an electric field is applied to the device, the band structure of the device is bent and an elastic electron-phonon scattering occurs, in which crystal lattice vibrate and electrons can change the subbands state without changing in their total energy. Subsequently, electrons are injected into the upper laser level through the injector barrier. Afterward, when electrons decay to the lower laser level, an optical intersubband transition occurs, resulting in photon with energy equals to the difference between the upper and lower laser levels. Then, the extractor will pull out the electrons from the lower laser level using phonon-scattering and injected to the next QW. The cascading through multiple QWs will result to emit coherent photons by falling from a higher energy level to a lower one as illustrated in Figure 2.8 [32], [33].

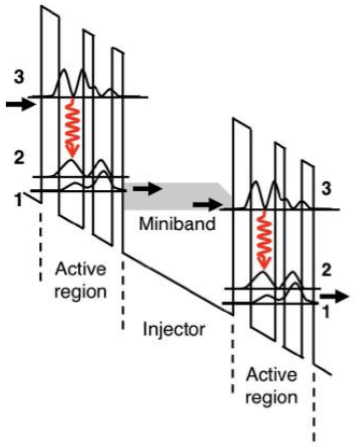

Figure 2.8 The representation of the QCL with three QWs. The upper laser level 3 is the injector, the lower laser level 2, and level 1 which is called the extractor state. Adapted from [85].

The separation between the states in each period is affected by the injection barriers, thin barrier will make large splitting between the states and fast injection and vice-versa. Thus, the performance of such laser depends on the electronic engineering technologies on the band structure design, in which the energy of the emitted photon can be controlled by the adjusting the thickness of the quantum wells and barriers [13], [82], which means that the wavelength of the QCL is essentially depended on that thicknesses [51], [52]. Moreover, large bandwidth of the emitted frequency can be tuned within the same semiconductor material system [86], and the number of the generated photons depends on the number of QWs stages [32], [82].

Based on the injection efficiency η, current density J, and the lifetime τ_{ij} of the initial and final transition ij between the subbands respectively, the following equations describe the scattering rate at each level:

$$\frac{\partial n_3}{\partial_t} = \frac{\eta J_{in}}{e} + \frac{n_1}{\tau_{13}} + \frac{n_2}{\tau_{23}} - \frac{n_3}{\tau_{31}} - \frac{n_3}{\tau_{32}} \quad (2.20)$$

$$\frac{\partial n_2}{\partial_t} = \frac{n_3}{\tau_{32}} + \frac{n_1}{\tau_{12}} - \frac{n_2}{\tau_{21}} - \frac{n_3}{\tau_{23}} \quad (2.21)$$

$$\frac{\partial n_1}{\partial_t} = \frac{n_2}{\tau_{21}} + \frac{n_3}{\tau_{31}} - \frac{n_1}{\tau_{12}} - \frac{n_1}{\tau_{13}} - \frac{J_{out}}{e} \quad (2.22)$$

in the equilibrium state, equation 2.21 can be simplified as the following:

$$\frac{n_3}{\tau_{32}} = \frac{n_2}{\tau_{21}} \quad (2.23)$$

By neglecting any absorption of the electrons, the population inversion will be occurring between level 3 and 2, which is an important condition to obtain the lasing for the system as explained previously.

Therefore, there are state-of-art active region and waveguide designs, which will be reviewed in the next sections, that have efforts on the development of the QCLs.

2.5 THz QCLs

Nowadays, THz QCLs have been further improved to be work at spectral range of 0.8–5.4 THz [81]. This is started when the QCLs became compact and well-established devices that can provide coherent and powerful radiation because of rapid development since its first demonstration in Bell labs in 1994, with short wavelength of 4 μm and 75 THz [33]. Since then, they become a paramount source of the semiconductor lasers with spectral range within the mid-infrared bands between 3 μm and 24 μm [73]. However, the development of THz QCLs encountered some challenges in their early stages owing to the free carrier absorption and the long wavelength, which leads to substantial material losses and optical model size is large. Not only that, but also the excited state of the laser transition has a relatively short lifetime due to the closely space subbands, which makes it difficult to achieve the required population inversion for the gain [73], [81]. The structure of the QCLs consist of the active region and the laser waveguides. Lasers waveguide must be optimally designed to achieve an efficient heat extraction and provide strong optical confinement. The systems of the active region, which is made of hundreds of thin layers, are based on either InP or GaAs substrate [87]. Thus, the performance of the THz QCL has been improved by developing several active regions design. There are various semiconductor material systems that affect the performance of the QCLs, which are GaInAs/AlInAs grow on InP substrates, InGaAs/AlInAsSb, InGaAs/GaAsSb or InGaAs/AlInGaAs grown on InP substrates [82], [88], [89], and the material system for the first THz QCL, GaAs/AlGaAs, grown on GaAs substrates that has been developed in 2002 and made a breakthrough in the THz technology and have become capable to emit THz radiation with wavelength of 68 μm and 4.4 THz. The active region of the device was based on the chirped superlattice semi-insulating surface- plasmon (SI-SP) waveguide design [34].

2.5.1 Active region designs

To achieve the population inversion between the energy levels of the laser, there are some factors that must be engineered to design the active region properly. These factors are energy levels, wavefunctions and scattering rates of the electrons within the subbands as explained previously in Section 2.4.1.

2.5.1.1 Chirped Superlattice (CSL)

As mentioned before that the active region of the device is formed by the growth of multi-Quantum wells based on different material systems, e.g., GaAs/AlGaAs grown on GaAs substrate. The chirped superlattice is created by coupling a number of Quantum Wells together as shown in Figure 2.9, which will result in the formation of the minibands [73]. The width of these minibands is controllable and can be adjusted by changing the barrier and wells thicknesses. When the QCL exposed to a convenient electric field, a photon will be emitted because of electron transition between the lowest energy state of the upper miniband and the highest energy state of the lower miniband. The population inversion in this type occurs due to elastic scattering of electrons within each miniband [13], [73].

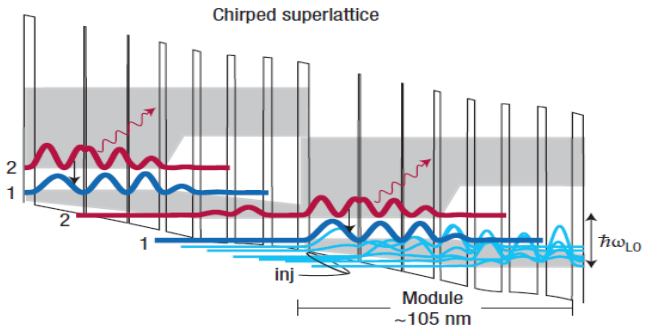

Figure 2.9 The CSL conduction-band diagram shows the transition between the lowest states of the upper miniband ‘2’, to the top state of the lower miniband ‘1’. Adapted from [73].

2.5.1.2 Bound-to-Continuum (BTC)

The depopulation process of the minibands and the lower radiative state of the BTC design is like the CSL, but the main difference is related to the upper radiative state, which is made to be a bound state next to the injection barrier inside a mini gap as shown in Figure 2.10. The strong coupling of the upper miniband state gives rise to better injection and extraction efficiency of the upper and lower states respectively, and the undesirable transition between the injector state and lower lasing level will be supressed [13], [73]. Therefore, the thermal backfilling will be reduced and lead to a higher operating temperature and more output power.

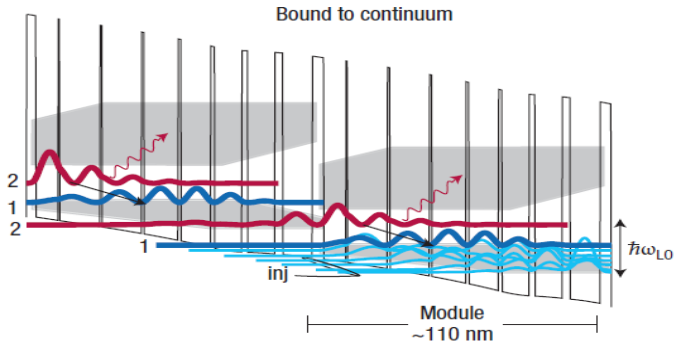

Figure 2.10 The Bound-To-Continuum active region design of QCLs. Adapted from [73].

2.5.1.3 Resonant-Phonon

The design of the third type of active regions, shown in Figure 2.11, depends on utilising the resonant tunnelling to couple the low radiative state with the upper radiative state of a neighbour quantum well, and depopulating the carriers faster via Longitudinal optical phonon (LO phonon) scattering to overcome the close subbands energy spacing issue. This implies that the low radiative state would have an energy equal to the LO phonon energy (~36 meV in GaAs), so that the energy of collector and injector must be smaller. Thus, higher optical gain can be achieved in RP design due to the shorter module length. However, owing to the very little overlap of the upper radiative state with the injector, the lifetime of the low radiative state will be reduced while the lifetime of the upper state will be preserved longer [73].

The operation of THz QCL with very long wavelength can be achieved by utilising a hybrid design structure (Shown in Figure 2.12), which is based on the incorporation between the BTC transition and phonon-assisted depopulation.

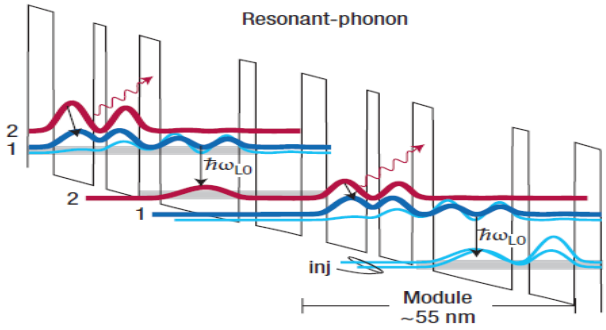

Figure 2.11 Resonant-Phonon structure. Adapted from [73].

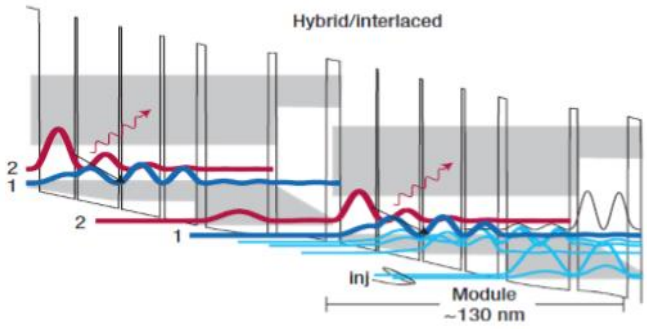

Figure 2.12 Hybrid design structure. Adapted from [73].

Since then, the performance of THz QCLs has been improved by designing different active regions that have been explained previously and an encyclopaedic literature review about it can be found in [73], [82]. When comes to the operation mode of the QCL, there are two types which are pulse mode and continuous wave mode. Using a single ridge waveguide in continuous wave (CW) mode, the peak power of the THz QCL achieved up to 0.23 W at 15 K, and more than 2 W in pulsed mode and with bound-to-continuum transition active region design as reported in [90], [91] respectively.

In terms of the operating temperature, the gain of the THz QCL degrades at high temperatures and still needs cryogenic cooling to obtain high power, which is considered as the main hindrance for further developments of the THz QCL. Seemingly, when coming to the THz QCL design development, it is always a trade-off between the operating temperatures and the output powers of the device. Thus, the effort on the improvement of the operating temperature leads to have about 200 K, but with power less than 0.1 W. The active region was based on resonant phonon based three-well design, and the material system was GaAs/AlGaAs as reported in [92]. Moreover, the generation of THz emission at room temperature has been achieved with the wastage of the output power that significantly dropped down to few microwatts when using the CW operation mode. However, the highest THz peak power up to ~ 0.2 W is recorded at room temperature using the pulsed mode operation. This is accomplished using difference-frequency generation (DFG) based on InP-based QCL as reported in [93]. Furthermore, an improvement on the temperature performance has been achieved when alternative material systems been used such as InGaAs/GaAsSb [94], InGaAs/InAlAs [95], InGaAs/ AlInGaAs [96], and Ge/SiGe heterostructures [97]. Recently, the development of THz QCLs leads to have high-power portable terahertz laser system at ~4 THz with a maximum operating temperature of 250 K operate with few milliwatts [98]. However, the laser was operated in pulsed mode but with 1% duty cycle and required high current to be operated and hence operating temperature would be limited in CW operation. The operation modes including the pulsed and CW will be explained later in details in Chapter 3.

To this point, it is indisputable that to achieve good performance THz QCL, we still need a cryogenic cooling, and thus increasing the size of the system

and the power consumption. Nevertheless, using a portable Stirling cooler as an alternative solution will make it suitable for many applications [81].

There are other characteristics that determine the performance of the THz QCL and play an important role in many applications. Our focus here is using the THz QCL as a local oscillator in a heterodyne receiver as explained previously in Chapter 1, so using it as a source for astronomy applications. Accordingly, to ensure an efficient coupling with the mixer in the heterodyne system, it must have a desirable good quality beam profile, which can be achieved by designing high resolution narrowband THz QCL to make sure that it works at the required frequency. The design parameter recommendations for a practical QCL-based local oscillator according to the development of the QCL report conducted in the University of Leeds are concluded in Table 2.1.

Table 2.1 Design parameter recommendations for a practical QCL-based local oscillator.

Design element	Recommendation	importance	notes
Active region	Hybrid design	Recommended	• Higher operating temperature that BTC • Better CW performance than RP designs • Higher output power than BTC or RP
Waveguide geometry	Double metal	Essential	• ≈80 K improvement in operating temperature over single metal • Decrease in threshold current
Waveguide material	Au-Au or Cu-Cu or Ag-Ag	Essential	Copper has better operating temperature, then silver, then gold
Active region thickness	10 μm	Recommended	Thinner active region can reduce power consumption, but at expense of operating temperature, threshold current, and output power
Ridge width	100-200 μm	Recommended	Wider ridges can give much larger output power, at expense of higher threshold current.
Beam-shaping method	Direct coupling to mixer block	Recommended	Additional beam-shaping elements are needed only for far-field coupling

However, these requirements are not achievable when using the normal QCL waveguide ridge and the emission characteristics need to be improved including the non-uniform beam profile, absolute frequency, and the inadequate power.

Photonic engineering techniques can be used to optimize key properties of the THz emission, including al the limitations that have been mentioned. One of these approaches is to use a diagonal feedhorn antenna and will be explained further in detail in Chapter 5. Moreover, it is important to mention the influence of the THz QCL waveguide designs and how they can affect the laser emission.

2.5.2 Waveguide design for THz QCL

One of the essential requirements of the laser's waveguides are to achieve an efficient heat extraction along with strong optical confinement. Ridge waveguides are the most common structure of THz QCLs, where the ridge region is the medium that confines the propagated light in two dimensions, which is reflected at the two facets by special mirrors [10]. In a short λ device, the refractive index of cladding layer must be less than the refractive index of the active region. However, at long wavelengths, the propagated mode leak into the cladding layer [73], which means that the normal dielectric waveguides are not convenient for such radiations. Generally, the characterization of the waveguide that determine the threshold gain g_{th} are affected by three main parameters, which are the loss coefficient (waveguide losses α_w due to the scattering and absorption), confinement factor Γ, and mirror loss coefficient α_m [73]. Thus, the gain should overcome those losses in the cavity for the laser to operate, and the threshold gain can be calculated as the following:

$$g_{th} = \frac{\alpha_w + \alpha_m}{\Gamma} \tag{2.24}$$

There are two principal waveguide designs that are utilized for THz QCLs, which are the semi-insulating surface plasmon (SI-SP) and the metal-metal waveguide.

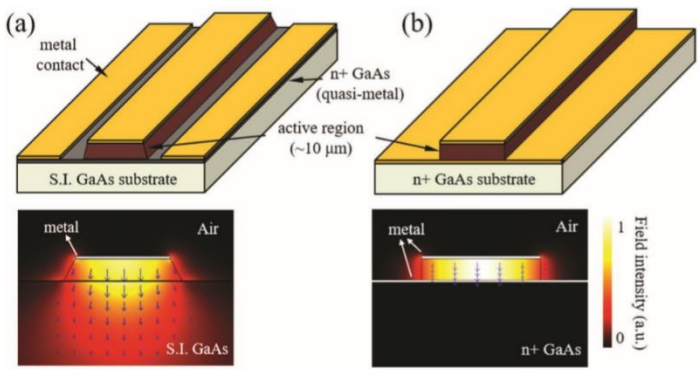

Figure 2.13 Schematic diagrams of THz QCL waveguides semi-insulating surface-plasmon (SI-SP) waveguide and (b) a double-metal (DM) waveguide. Adapted from [81].

2.5.2.1 Semi Insulating Single Plasmon (SI-SP) waveguides

The structure in Figure 2.13(a) shows how the THz mode confined with the SI-SP waveguide, where the ridge (active region) is sandwiched between a top metal layer and a thin surface-plasmon layer, which is made by a heavily doped *n*+ layer of the GaAs [2], [73]. The conventional purpose of this design is to reduce the absorption losses and confines the optical mode tightly at long-wavelength [34].

Although low free-carrier losses and high optical power can be obtained in such design, the minimum device area is limited due to poor optical confinement. This penetration, in turn, results in a small confinement factor and reduces the temperature performance of the device [2], [13], [73].

QCLs based on a SI-SP waveguide at 3.4 THz can produce maximum optical power up to 1.01 W at 10 K and can be operated up to 123 K as demonstrated in [88], and as mentioned previously ~2 W at 10 K but with maximum operating temperature 105 K [91].

2.5.2.2 Double metal or metal-metal (MM) waveguides

The structure of the MM waveguide, shown in Figure 2.13(b), is similar to a microstrip or parallel plate waveguide, where the radiation is fully confined within the active region between the top and bottom metallic layers in a sub-wavelength dimension, and the confinement factor for such design is very high ($\Gamma \sim 1$) [99]. Although the efficiency for such design is reduced due to the very high divergence of radiation and the strong confinement of the light, a higher operating temperature can be achieved due to the reduction of the self-heating of the device which results from the effect of the second metallic layer [2], [13], [99].

QCLs based on Au–Au waveguide have been demonstrated to work up to about 160 K operating temperature, but with maximum optical power up to few mW [100]. Additionally, even better operating temperature performance has been achieved to work up to ~200 K based on Cu–Cu waveguide design because it has better thermal and electrical conductivity [92]. This is due to the electric and thermal conductivity, which is higher in copper than in gold as will explained later in Chapter 3 which we also consider higher conductivity Ag–Ag devices.

2.6 Summary

In this chapter, an introductory to the laser technology has been recalled with an explanation on how the electrons can response to an incident energy in an atomic energy levels in different ways, which are absorptions, spontaneous emissions, and stimulated emission. The stimulated emission is ensured by achieving two main design parameters, which are: population inversion, and high photon density. The propagated light of the laser is then confined in a waveguide to produce internal reflection within an optical resonant cavity to provide large photon density. Thus, the waveguide theory

and structure have been reviewed to understand the behaviour of the electromagnetic field inside the waveguide using cladding material. After that, an introductory to the quantum well heterostructure has been reviewed with further explanation on the fundamentals of the QCL and its functionality. This is followed by a literature review on the THz QCL with explanation on the different THz active region designs and the THz waveguide design, which hare SI-SP and DM waveguides.

Therefore, the following chapter will focus on fabricating THz QCLs based on the two different waveguide designs. The fabricated devices will then be characterised and analysed to examine the performance of the different designs in terms of power, spectral resolution, maximum operating temperature.

Chapter 3

THz Quantum Cascade Lasers fabrication

This chapter discusses the two different THz QCL fabrication methods, which are the semi insulating single-plasmon and the double metal waveguides process. As discussed previously in Chapter 2, each method influences the QCL performance in terms of the output power and operating temperature, which will be investigated later in this chapter. All the devices presented in the thesis are fabricated and characterised by myself with Dr Yingjun Han supervision.

The active region of the QCLs is grown by two main techniques, which are the metalorganic vapor phase epitaxy, and molecular beam epitaxy (MBE). The MBE is the favourable method for the QCLs fabrication due to the controllability of the doping profile [101]. Such technique is based on a thermal evaporator system, where thin-atomic layers of GaAs/AlGaAs material are sequentially grown under ultra-high vacuum pressure ($\sim 10^{-11}$ mbar) [102].

3.1 Semi insulating single-plasmon (SI-SP) process

THz QCL chips are fabricated following several iterations of micro and nanofabrication techniques, such as photolithography, wet chemical etching, and evaporation of thin films of metals and annealing. These techniques are utilised to fabricate QCL through main processing stages as illustrated in Figure 3.1. In a typical SI-SP QCL device, there are four main layers as shown in Figure 3.2, the purpose of the top n^+-GaAs is to provide better Ohmic contact; the active region in the middle is the gain material which made of hundreds of layers as explained previously in Chapter 2 about the waveguide theory; and the lower n^+-GaAs is used to provide better Ohmic contact as well as better laser mode confinement; the SI-GaAs works as a supporting substrate.

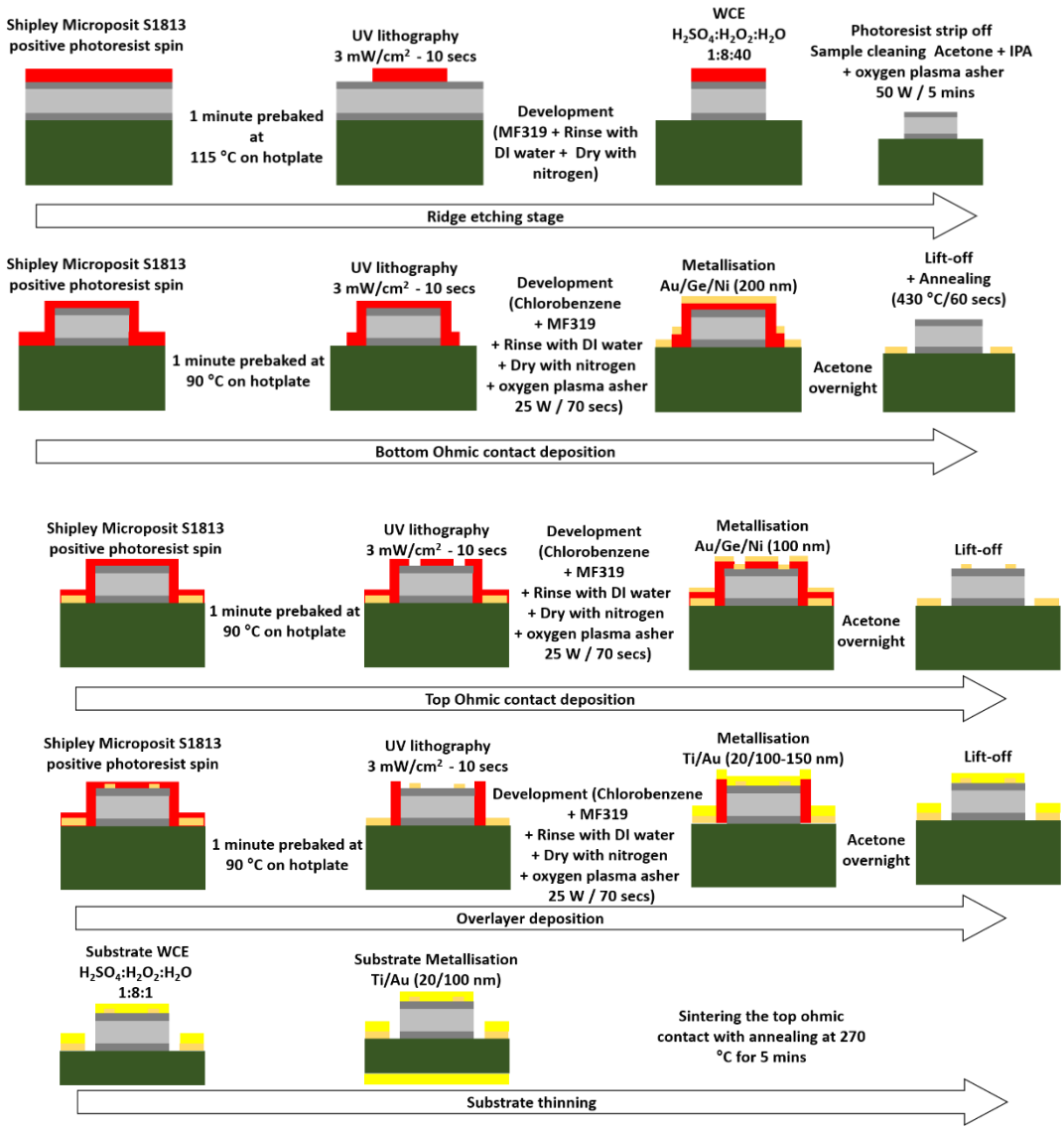

Figure 3.1 Illustration of SI-SP fabrication process

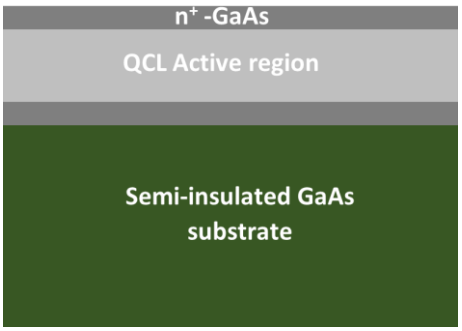

Figure 3.2 Illustration of the main layers in an SI-SP waveguide

The time plan for fabricating a successful SI-SP QCL is shown in the Table 3.1, bearing in mind that this plan assumes that all the equipment needed are available to be used throughout the period and along with normal operation in the nanotechnology room and without any problems that may occur during the fabrication processes.

Table 3.1. Fabrication time plan for the SI-SP process.

FABRICATION PLANNER FOR SI-SP QCL	
Day 1	**Process:** Cleaning process + Ridge etching stage **Equipment needed:** Ultrasonic bath – Plasma Asher – UV lithography – WCE bench – surface profiler **Estimated time:** [4-5 hours]
Day 2	**Process:** Bottom Ohmic contact deposition – overnight lift-off **Equipment needed:** UV lithography – Edward 306A thermal evaporator **Estimated time:** [4 hours]
Day 3	**Process:** Bottom Contact annealing – Top Ohmic contact deposition – overnight lift-off **Equipment needed:** AnnealSys - UV lithography – Edward 306A thermal evaporator **Estimated time:** [4 hours]
Day 4	**Process:** Overlayer deposition – overnight lift-off **Equipment needed:** UV lithography – Edward 306A thermal evaporator **Estimated time:** [4 hours] depends on the quality of the chemical solution
Day 5	**Process:** Substrate thinning using WCE + metallization **Equipment needed:** WCE bench E-beam evaporator **Estimated time:** [4-6 hours] depends on the number of chips
Day 6	**Process:** Sintering the Top Ohmic contact - Cleaving process **Equipment needed:** AnnealSys - Scriber **Estimated time:** [3 - 4 hours] depends on the number of chips
Day 7	**Process:** QCL mounting **Equipment needed:** QCL mounting tools in foyer in THz lab room (copper block, indium, hot plate, QCL mount holding pins) **Estimated time:** [3 – 4 hours] depends on the number of devices
Day 8	**Process:** Wire bonding **Equipment needed:** Ball bonder **Estimated time:** [2-3 hours]

3.1.1 Sample cleaning and edge bead removal

In the first instance, the sample is cleaned to remove any contaminations resulting from the transfer of samples. This is done by immersing the sample in acetone and an ultrasonic bath for 1 minute with 10% power, followed by a rinse with isopropyl alcohol (IPA). To remove any remaining organic residues, the sample is also cleaned with an oxygen plasma asher at 50 W for five minutes. Usually, this cleaning procedure is repeated every time before spinning the photoresist on the sample. After the initial cleaning, the QCL ridges are processed using the photolithography technique, which involves coating the top of the sample with a photoresist material and exposing a selective area of the sample under an Ultraviolet (UV) light. Specifically, the sample is spin coated with Shipley Microposit S1813 positive photoresist at 5000 rpm for 30 seconds, then baked at 115˚C using a hotplate for about 1 minute. The sample is subsequently exposed to the UV light under an edge removal pattern using a predefined photomask at a dose of ~3 mW/cm^2 for about 1 minute and 30 seconds to remove the photoresist at the corners and along the edges of the sample. after that, Shipley® Microposit® MF-319 developer is used for two minutes to remove the photoresist that been exposed to UV. This is followed by a rinse with deionised water and drying with a nitrogen jet.

The photolithography technique is used to pattern the photoresist thin film before the chemical etching to form the ridges of the QCL sample, and before the metallisation process to form the bottom contact, top contact, and the claddings.

3.1.2 Ridge etching

The ridges of the QCL are defined after the sample is spin-coated with Shipley Microposit S1813 positive photoresist and soft baked on a hot plate at 115˚C for 1 minute. After that, the sample is exposed to UV light for about 10 s under the predefined photomask to form the ridge patterns with 150-µm width and 6-mm length. Then, MF-319 is used to develop the sample for about 70 s followed by rinsing the sample with DI-water and drying with nitrogen. The ridges pattern is now defined as shown in Figure 3.3(a).

It is important to mention that the ridge etching process is the most problematic step in the SI-SP fabrication process as it requires extra care to avoid over etching, so that why we need to spend more time doing the etching and check the device using the surface profiler until we reach the required thickness. Wet chemical etching is used to etch ridges on the sample surface by using a combination of a Piranha etch chemical solution including sulfuric acid, hydrogen peroxide, and deionised water (H_2SO_4:H_2O_2:H_2O) with a ratio of 1:8:40 respectively. Prior to the etching, the back side of the sample must be coated with Shipley Microposit S1813 and bake it for few minutes on a 115˚C hotplate; this will protect it from the etching process. Then, an alpha step surface profiler is used to measure the height between the defined ridge and the normal surface of the sample, which will give a clear idea about the

maximum amount of etching for the active region layer. The etching process is then applied for few minutes by rinsing the sample inside the chemical solution while agitating circularly or as figure-of-eight shape to ensure equal etching for the surface. Then, the height between the ridge and the active region is re-measured to calculate the etching rate per minute and record the new thickness. The process is repeated until the required thickness is achieved, which for most QCLs must usually not exceed 10–12 µm. Figure 3.3(b) shows an optical microscope image of the QCL after the ridge etching process. One important thing we must know is that that the width of the ridge has slop side wall, and it is narrower at the top, and wider at the bottom.

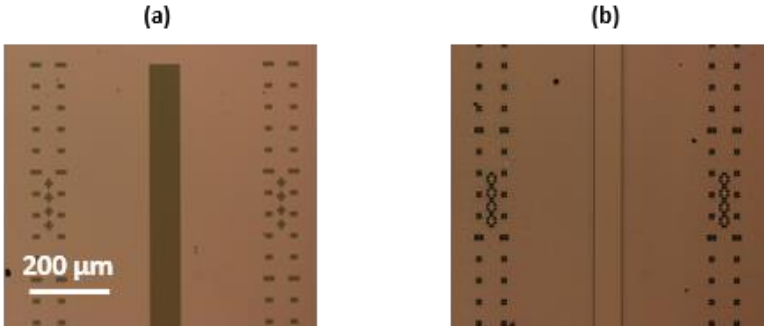

Figure 3.3 Optical microscope images for the ridge of the QCL (a) lithography and (b) etching process, which is etched by about 11 µm, during QCL fabrication in the clean room on QCL.

3.1.3 Bottom Ohmic Contact Deposition:

The main aim of this step is to define the Ohmic contact metal on either side of each ridge of the QCL. To do that, the sample is first cleaned after the ridge etching process before applying the same photoresist spin technique but this time with lower bake temperature (90˚C) to ensure optimal lift-off process for the metal. The photolithography technique follows the same procedures that have been used before with an appropriate photomask pattern to define the bottom contact. In addition, the sample is soaked in chlorobenzene before the developing step, which is used to strengthen the sample and provide an undercut to ensure a safe lift-off process later. An oxygen plasma asher at 25 W for 70 s is used after the development step and prior to the metallization step to remove stray organic residues from the sample surface.

The Edwards 306A thermal evaporator in the University of Leeds cleanroom is used for the metallisation process by evaporating 200 nm from the gold–germanium–nickel (Au/Ge/Ni) material to the bottom contacts of the sample, at pressure $\sim 1.8 \times 10^{-2}$ mbar to the QCL. After that, the sample is soaked in acetone and left overnight to ease the lift–off process of the metal from the surface. Following the cleaning step, the sample is loaded into a rapid thermal annealer (AnnealSys) to diffuse the metalized bottom Ohmic contact into the substrate at about 430°C for 60 s. Figure 3.4 shows an optical microscopy image of the QCL sample after annealing process of the bottom Ohmic contacts.

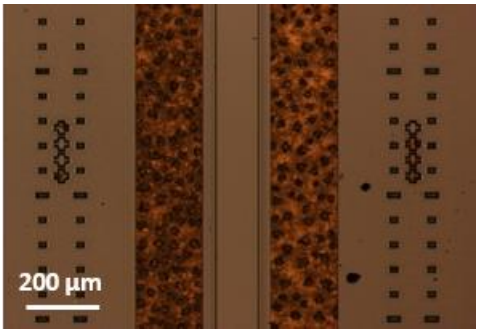

Figure 3.4 Optical microscopy image of the QCL sample after annealing of the bottom Ohmic contacts.

3.1.4 Top Ohmic Contact Deposition

This step aims to define the top Ohmic contacts as two 10-µm wide strips on the top of each ridge with about 100-nm thickness by applying Identical processing steps, including the photolithography, evaporation, and lift-off processes. An optical microscopy image for the top Ohmic contacts of the QCL sample after lift–off is shown in Figure 3.5.

3.1.5 Overlayer deposition

This step aims to cover the whole surface of the ridges to confine the radiation of the laser and to cover the bottom Ohmic contacts to improve the wire bonding later. All the processing techniques that have been used before for the top and bottom Ohmic contacts are used here to evaporate a thin layer of about 20 nm of the titanium (Ti) and 100 nm of Au. An optical microscopy image of the cladding metal after the lift-off is shown in Figure 3.6.

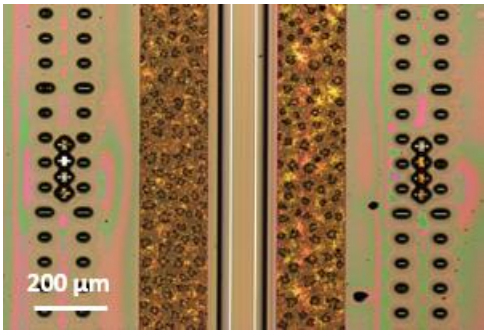

Figure 3.5 Optical microscopy image of the top Ohmic contacts of the QCL sample after lift–off.

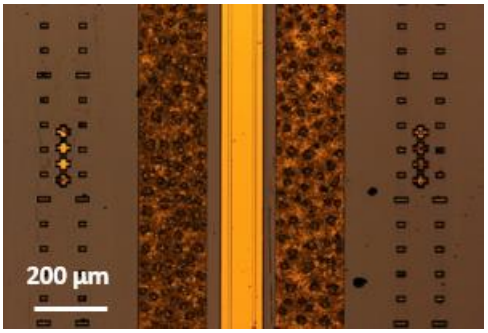

Figure 3.6 Optical microscopy image of the cladding metal after the lift-off of the QCL sample.

3.1.6 Substrate thinning

At the end of the fabrication, wet chemical etching is used to thin the GaAs substrate to improve the thermal dissipation of the QCL. The chemical solution that has been used is H_2SO_4 (40 ml): H_2O_2 (320 ml): H_2O (40 ml). To do that, the top side of the sample is covered with photoresist and wax mounted on a piece of glass, the thickness is then measured with a micrometre measuring tool before the etching and after a few minutes to check the thickness and the etching rate; the process is then repeated until the required thickness is achieved. After the etching, the sample is rinsed with DI-water to stop the etching. Then, a hot plate is used to melt the wax on the glass and remove the sample easily. The sample is cleaned after that using trichloroethylene, acetone, and IPA, respectively. The last step is to evaporate 20-nm Ti/ 100-nm Au on the backside of the sample.

3.1.7 Sintering of top Ohmic contact

This step is used to ensure adhesion of the metal onto the substrate. This is done by using the same rapid thermal annealer but with lower temperature of about 270˚C for 5 minutes.

3.1.8 Mounting process

The final fabricated sample of the QCL contains three ridges; each ridge represents an operational laser. Thus, a cutting process must be applied to the sample by using a JFP S-100 automated scriber to separate these ridges from each other as shown in Figure 3.7(a). Then, these ridges are cleaved into multiple chips to obtain the optical cavities of the laser as shown in Figure 3.7(b). This process must be done carefully to avoid damaging the facet and the surface because it might cause an increase in the mirror losses and the threshold current.

The cleaved devices are usually mounted on a heat-sink to reduce the thermal backfilling of the device. So, it is mounted on a Cu block using In/Au soldering. The top contact is wire bonded to a ceramic pad and bottom to the copper as shown in Figure 3.7(c). To this end, the device should be ready to be tested and characterised in the THz Lab.

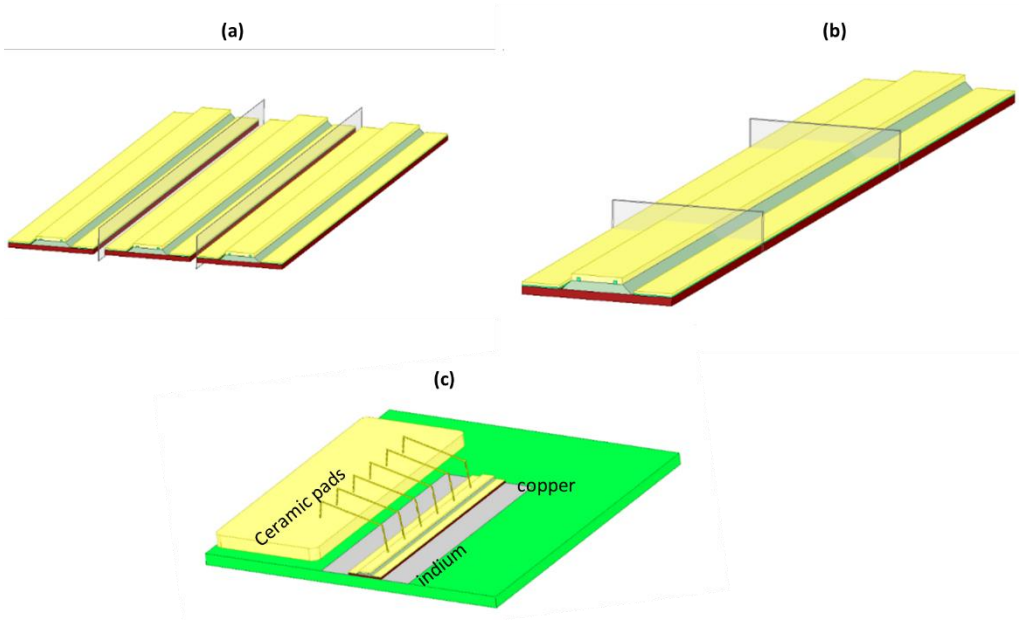

Figure 3.7 Schematic of the (a) scribing and (b) cleaving process for the three laser ridges of the fabricated QCL. (c) Mounting and Au wire bonding.

3.2 Double-metal process

The fabrication of the double metal waveguide is a more complicated process than the normal SI-SP waveguide, as it requires postgrowth processing of the laser heterostructures. As explained previously in Chapter 2, the active region of the QCL with double metal waveguide is confined from top and bottom with metal layers, which would provide better confinement and better operating temperature and hence a low loss waveguide, which makes the QCLs more appropriate for use as a LO in satellite applications. Therefore, the fabrication needs to provide metal layers adjacent to the active region, the process starts by removing the GaAs substrate on which the active region was grown.

Moreover, the selection of cladding metal layers has a direct effect to further reduce waveguide losses depending on their properties. Copper (Cu), gold (Au), and silver are variant waveguide metals that have been investigated in [103], in order of preference for thermal and electrical conductivity, silver comes first, then copper and then gold. However, there are some other factors that need to be taken in consideration during the fabrication process that would change priority order for the selection of the metals, which will be explained later.

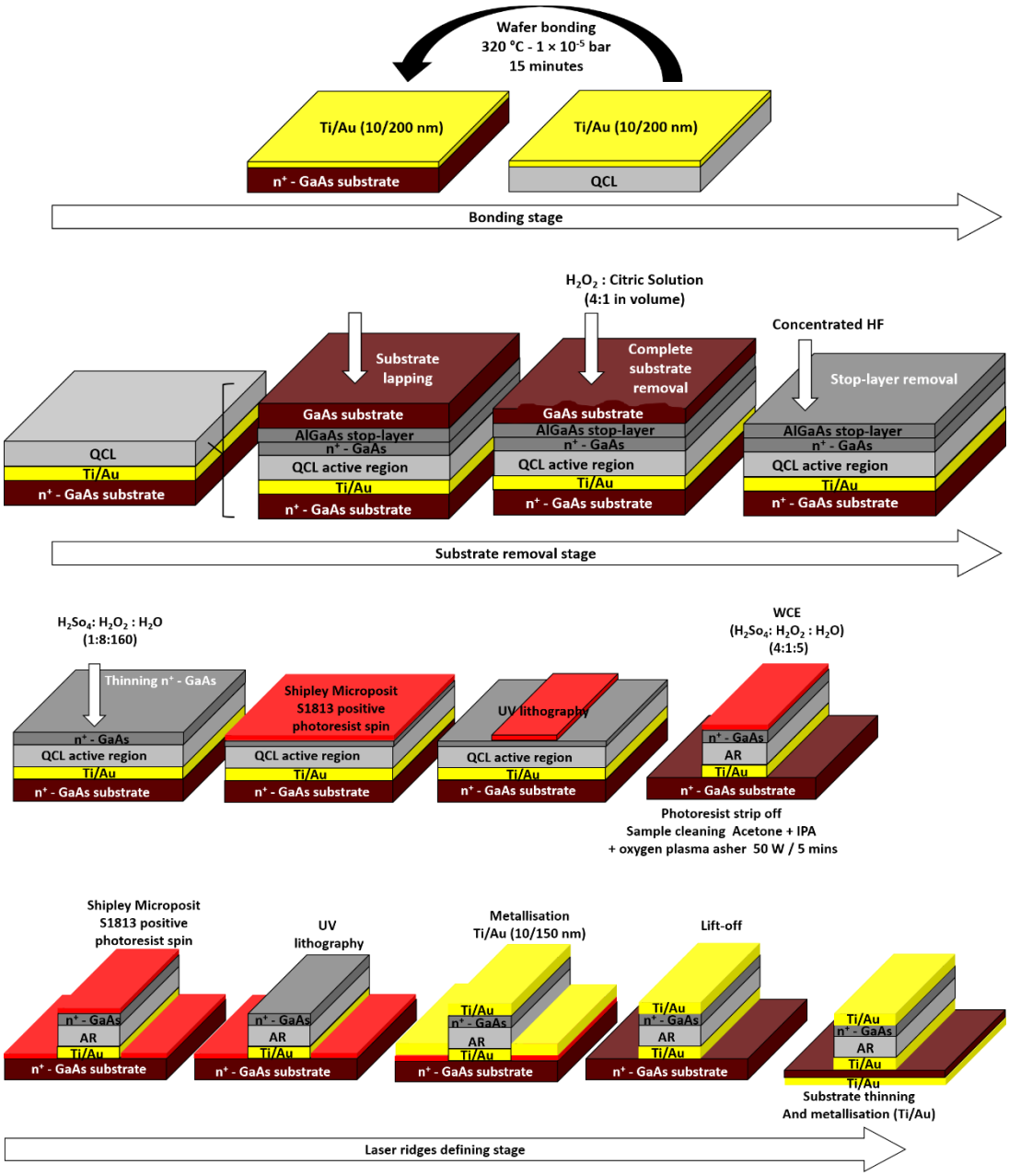

Figure 3.8 Illustration of the three main stages of the DM QCL fabrication process.

To start the manufacturing process, we must first understand the main layers of the QCL wafer, most wafers often have the same main structure with a difference in the thickness and layers of the active region, which determines the frequency and operational efficiency of the laser. Figure 3.8 shows the main structure of a QCL wafer, which consists of four main layers: the conductive substrate based on GaAs, AlGaAs stop-layer, n^+-GaAs buffer layer, and the QCL active region (GaAs/AlGaAs). The fabrication process of the double metal QCL goes through three main stages as shown in Figure 3.8 which are: the bonding stage, substrate removal stage, and laser ridges defining stage. Each stage is done by applying several fabrication techniques in the nanotechnology clean room in the University of Leeds.

The bonding and substrate removal stages are the two post growth processes that are critical and needs extra care to avoid any damage during the bonding and avoid losing specific layers or over etching during the substrate removal.

The time plan for fabricating a successful DM-QCL is a little bit longer than the SI-SP period, owing to the need for postgrowth processes. Table 3.2 shows the time plan needed to fabricate a DM-QCL, assuming the availability for all the needed equipment throughout the period and along with normal operation in the nanotechnology room and without any problems that may occur during the fabrication processes.

Table 3.2. The time plane for DM-QCL processes.

FABRICATION PLANNER FOR DM-QCL	
Day 1	**Process:** Cleaning process (GaAs and QCL wafers) + Metallization (Ti/Ag/Ti/Au) for both wafers **Equipment needed:** Ultrasonic bath – Plasma Asher – E-beam evaporator **Estimated time:** [3 hours]
Day 2	**Process:** Wafer bonding + cut the wafer into small chips **Equipment needed:** Wafer bonder – Saw machine **Estimated time:** [4 hours]
Day 3	**Process:** Preparing the samples for substrate removal (GaAs of the QCL wafer) **Equipment needed:** Hot plate to mount the samples with the mechanical pressure tool – Lapping station. **Estimated time:** [4 hours] – for 4 to 5 chips
Day 4	**Process:** Complete substrate removal (GaAs of the QCL wafer) using WCE H_2O_2: Citric solution (4:1) and concentrated HF etching (to remove the AlGaAs stop-layer) **Equipment needed:** WCE bench – HF bench **Estimated time:** [4 hours] depends on the quality of the chemical solution
Day 5	**Process:** n + -GaAs thinning using the WCE H_2So_4: H_2O2: H_2O (1:8:160) + forming the QCL ridges using the lithography and WCE **Equipment needed:** WCE bench – alpha step - UV lithography **Estimated time:** [4-6 hours] depends on the number of chips

Day 6	**Process:** Top contact layer metallization (Ti/Ag/Ti/Au) + overnight left-off **Equipment needed:** UV lithography – E-beam evaporator **Estimated time:** [4-6 hours] depends on the number of chips
Day 7	**Process:** Substrate thinning using WCE + metallization + Annealing **Equipment needed:** WCE bench – E-beam evaporator - AnnylSys **Estimated time:** [4-6 hours] depends on the number of chips
Day 8	**Process:** Substrate thinning using WCE + metallization **Equipment needed:** WCE bench – E-beam evaporator **Estimated time:** [4-6 hours] depends on the number of chips
Day 9	**Process:** Cleaving process + QCL mounting **Equipment needed:** Scriber – QCL mounting tools in foyer in THz lab room (copper block, indium, hot plate, QCL mount holding pins) **Estimated time:** [4-5 hours] depends on the number of devices
Day 10	**Process:** Wire bonding **Equipment needed:** Ball bonder **Estimated time:** [2-3 hours]

3.2.1 Bonding stage

The main aim of this stage is to define the bottom metallic layer of the DM waveguide by depositing the metal layer to the top side of the QCL wafer, which is the active region, and to a conductive n^+-GaAs substrate wafer. Then, the metallised surfaces of the two wafers are bonded using a thermocompression-bonding method.

Prior to the metallisation step, both wafers need to be cleaned using acetone, IPA, and then in a high-frequency oxygen discharge plasma to make sure that surfaces were cleaned from any residues. After that, the formation of the bottom cladding of the Au–Au waveguide is made using an Electron Beam Evaporator, using Titanium and gold (Ti/Au) with thicknesses 10 nm/200 nm, respectively. The Ti layer is used to prevent the Au diffusion to the active region of the QCL by choosing an appropriate thickness, and act as an adhesive layer for the gold. Afterwards, thermocompression bonding is used to join the wafers, by making sure that the plates of the bonding machine are equally balanced, and both wafers aligned correctly on the top of each other from the metalized surfaces sides. To achieve the melting point, performed at 320˚C and ~1×10^{-5} bar for at least 15 minutes. At this point, the bonding stage process is finished, and we have the QCL wafer flipped on the n^+-GaAs wafer from the metallised surfaces as shown in Figure 3.8, so that we have the first metallic layer of the DM waveguide underneath the active region of the QCL.

The main aim from this stage is to reach the other side of the active region and define the top metallic cladding of the DM waveguide. To do that, 3 of 4

of the main layers that have been mentioned previously for the QCL wafer need to be removed, which is done by following a sequential scheme of removal operations.

Firstly, the GaAs substrate from the QCL wafer has thickness of about 620–650 µm and need to be thinned to about 20–30 µm, which is done mechanically using a lapping process. To do this, we melt wax on a tempered glass on a hot plate, then the sample is mounted on the tempered glass from the n^+-GaAs wafer side and covered with baking paper from the top side. Then, the sample is mechanically pressed using another piece of tempered glass on the top of the baking paper with a hot plate temperature up to 120˚C. Then, we move it to a cooled surface and wait until the temperature to become less than 50˚C to make sure that the wax is set before releasing the sample. After that, the sample is thinned using a lapping machine to make sure the surface of the sample is equally thinned and flat. Secondly, the remaining GaAs substrate is then completely removed by wet chemical etching technique using chemical solution of H_2O_2:citric-acid solution with ratio 4:1 in volume.

To this point, the QCL fabrication reached the AlGaAs stop-layer, which is removed using concentrated hydrofluoric-acid (HF) that has high etched selectivity and does not etch the next buffer layer of the n^+-GaAs.

3.2.2 Laser ridges formation stage

This stage starts with thinning the n^+-GaAs layer from 700 nm to about 100 nm using a slow-rate etching chemical solution of H_2SO_4:H_2O_2:H_2O (1:8:160). This is done by defining a small area of the sample, from one of the corners, with Shipley Microposit S1813 positive photoresist, soft baking it, and exposing it to UV light. An alpha step surface profiler is then used to measure the height between the coated area and the normal surface of the sample. The etching process is then applied carefully for less than a minute by rinsing the sample inside the chemical solution circularly or as a figure-of-eight shape to ensure equal etching for the surface. The height between the coated area and the surface is then measured to check how much material remain to be etched. The process is repeated until the required thickness is achieved.

The fabrication of the QCL ridges is then done using wet chemical etching (WCE) technique in which the ridges are formed with inclined side walls. Following the same procedures used before with the single metal waveguide QCL, the ridges are defined using the UV lithography technique in which the sample is coated with Shipley Microposit S1813 positive photoresist and soft baked on a hot plate at 100˚C for 1 minute. After that, the sample is exposed to UV light with a pre-defined mask with ridge patterns width of 125-µm width and 6-mm length. Then, MF-319 is used to develop the sample for about 70 s followed by rinsing the sample with DI-water and drying with nitrogen.

The WCE is used to etch ridges on the sample surface by using a combination of a chemical solution H_2SO_4:H_2O_2:H_2O with a ratio of 4:1:5, respectively. Prior to the etching, the back side of the sample must be coated with Shipley Microposit S1813 and baked for few minutes on a 115˚C hotplate; this will protect it from the etching process. The etching process is then applied carefully until all the active region is etched, this is can be known by seeing colour changing of the sample and observing the bottom gold layer that has been defined before. The sample is then rinsed with DI water for few seconds and dried with nitrogen. The sample is then checked with a microscope to check the quality of the ridges and to see if any remaining materials need to be removed from the surface. If the surface still has some residue, the etching is continued for few seconds and checked again with the microscope. After that, the sample is cleaned with acetone and IPA. After that, we define the top metallic layer of the Au–Au waveguide following the same procedures of UV lithography and e-beam evaporation. In case of using the Ag–Ag waveguide, the process follows the same metallisation approach that is used when the top cladding layer is been defined; so that the top metallic layer will be Ti/Ag/Ti/Au.

Finally, the GaAs substrate, which is under the bottom metallic layer, is thinned using WCE. This will make the packaging process easier and allow better heat extraction. The final structure of the QCL is shown in Figure 3.8, and optical images for the device for the main stages are shown in Figure 3.9.

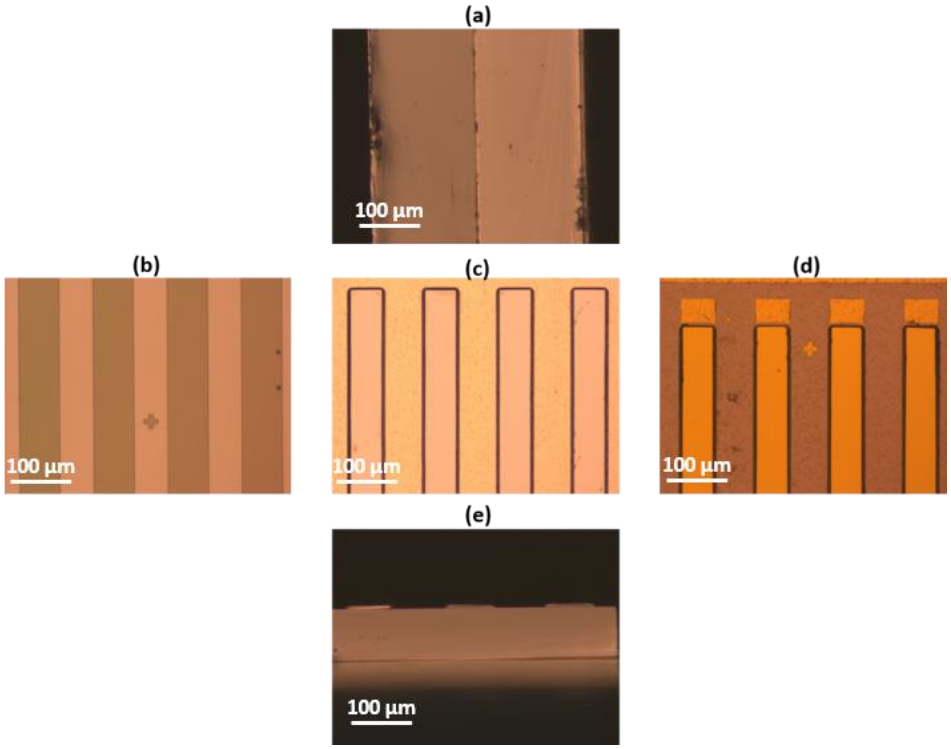

Figure 3.9 Optical microscope images for the main stages of the DM QCL fabrication. (a) the device after the bonding. (b) Photolithography for the ridges. (c) WCE for the ridges. (d) Metallisation for the top cladding layer. (e) front side of the facets after the cleaving.

3.3 Characterisation methods for the fabricated devices

There are some important and basic characteristics that can show the QCL performance after the long sequence of the fabrication steps. These characteristics are the light-current-voltage characteristics (LIV), which involves investigating the maximum output power that can be gained from the device (P_{max}), the threshold current (I_{th}) which is the minimum current required for the device to start lasing at the operating voltage (V_{th}), and the voltage as a function of the drive current. The spectra are another important factor that can be analysed to study the emission behaviour as a single or multi-mode and as a narrow or wideband source and its suitability for different applications. The thermal operation performance of the device can also be investigated by characterising the LIV at different heat sink temperatures to obtain the maximum operating temperature for the device. A QCL with high output power, high-operating temperature, and narrow emitting spectrum and radiation pattern are generally preferred for most applications [87].

The test can be operated in two modes, which are the pulsed mode and continuous wave mode (CW). In pulsed mode operation, the QCL is being turned on and off by using an external signal, generated from the pulse generator, to apply short electrical pulses with a low duty cycle. In the first experiment, the duty cycle of 2% is used that represents the time percentage of the laser when it is on, and the laser produce pulses of THz radiation. 100% duty cycle means that the laser is operated in CW mode, which means that THz radiation is continuous wave. In addition, the temperature of the active region in pulse mode is almost the same as the heatsink temperature, while it is higher than the heatsink temperature for the CW mode due to the effect of the self-heating [87].

Additionally, there are some important factors that have a proportional effect on the total output power of the QCL, which are core doping, number of QCL stages, cavity length, and width of the ridge. In pulsed mode operation, increasing any of these factors will affect correspondingly the peak power, while it will result in increasing the internal heating of the core in CW mode. Therefore, it is always a trade-off between having a high power or an efficient heat removal in a QCL [32].

3.3.1 Optical and experimental set-up for LIV measurements

The packaged QCL devices were mounted on a cold finger of a Janis ST-100 continuous flow cryostat. This cold finger is connected to a heater, which is used to regulate the operating temperature of the QCL by a temperature controller. The cryostat outer chamber is pumped down to vacuum to be about 8×10^{6} mbar to provide thermal insulation. This can be done by using a turbo vacuum pump connected to the evacuation valve of the cryostat. After that, the cryostat is cooled down by utilising continuous flow of liquid helium (He) through the helium entry tube.

The block diagram in Figure 3.10 shows all the electronic devices that have been used for characterising the QCL. To match the responsivity of the

bolometer detector, the signal generator is used to generate a frequency of 166 Hz to gate the output of the pulse generator and provide a reference to the lock-in amplifier. The QCL is driven by connecting the pulse generator to electrical feedthrough of the cryostat at 10-kHz pulse rate and driving pulse of 2% duty cycle, with inductive loop current probe between them that is used to monitor and control the current flow of the QCL. Both the output from the current probe and the output of the sense port of the cryostat that measures the operating voltage of the QCL were connected to a digital oscilloscope in two different channels.

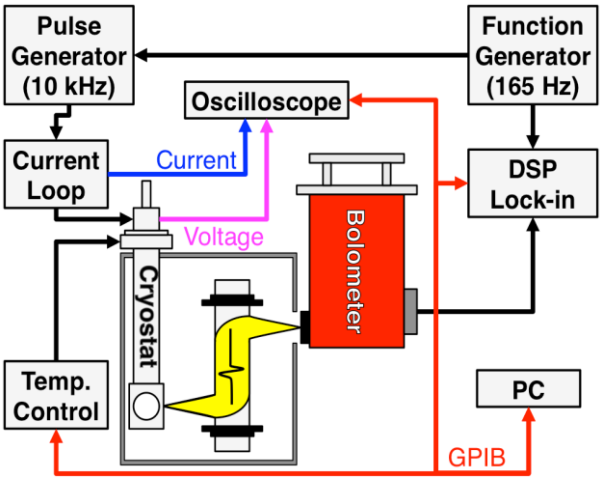

Figure 3.10 Schematic diagram of the optical and experimental set-up for the LIV characteristics. Reproduced from [104].

The THz radiation of the QCL is transmitted through a polyethene window in the cryostat. An *xyz* micrometre controller stage is used to adjust the alignment of the cryostat to observe the maximum output from the laser emission and direct it to the detector through gold-coated parabolic reflectors (parabolic mirrors), which is housed in a nitrogen-purged chamber to minimise absorption of THz radiation by water vapour. A cryogenically (He) cooled QMC QSIB/3 bolometer is used to detect the radiation from the reflectors.

The detector is susceptible to ambient THz noise in addition to the signal. This combined with the absorption of the THz radiation by water in air makes it weak and difficult to be detected. Therefore, a signal recovery system is required to separate the modulated QCL signal from the noise, which is done by using a 7225 DSP lock-in amplifier.

A National Instruments LabView instrument panel has been used to record the LIV data and curves by connecting the oscilloscope, the lock-in amplifier, and the temperature controller to a PC. The heat sink temperature has been regulated to vary from 10 K up to the maximum operating temperature of the device, in which no output power is observed. The laser drive current, the operating voltage, and the power from the lock-in amplifier are tabulated in a text file and then analysed using a MATLAB code. Finally, a Thomas Keating (TK) Absolute Terahertz Power Meter is used to measure the absolute emitted power of the QCL.

3.3.2 Optical and experimental set-up for spectra characteristics

The characterisation setup for spectral measurements is almost the same as that used for the LIV characteristics. The main difference is that a Fourier transform infrared (FTIR) spectrometer is used to measure the spectra in a rapid scan mode at different driving currents as shown in Figure 3.11.

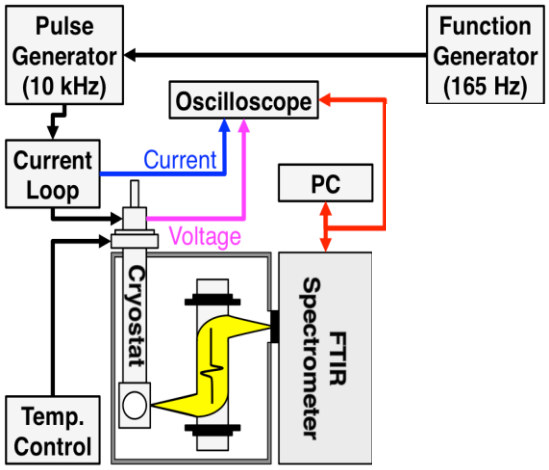

Figure 3.11 Schematic diagram of the optical and experimental set-up for the spectral characteristics. Reproduced from [104].

The FTIR is designed based on an optical device called an interferometer as shown in Figure 3.12, which produces a signal that carries all the frequencies encoded from the source into it. The incoming signal is divided into two optical beams using a beam splitter. The first optical beam is reflected to a stationary flat mirror, while the other is reflected to an adjustable flat mirror that can move away from or close to the beam splitter with millimetres distance. When the two beams are reflected from their respective mirrors, they recombined again as one beam at the beam splitter and directed to the detector as an interferogram. The interferogram has all the required information to convey and measure all the frequencies from the source due to the moving mirror position that provide every data point to form the signal. After that, all the individual frequencies are being decoded using a mathematical technique called Fourier transformation, which is obtained by the computer through OPUS software to perform the frequency spectrum. Then, this spectrum is reproduced by a MATLAB code as a plot of the intensity at each individual frequency.

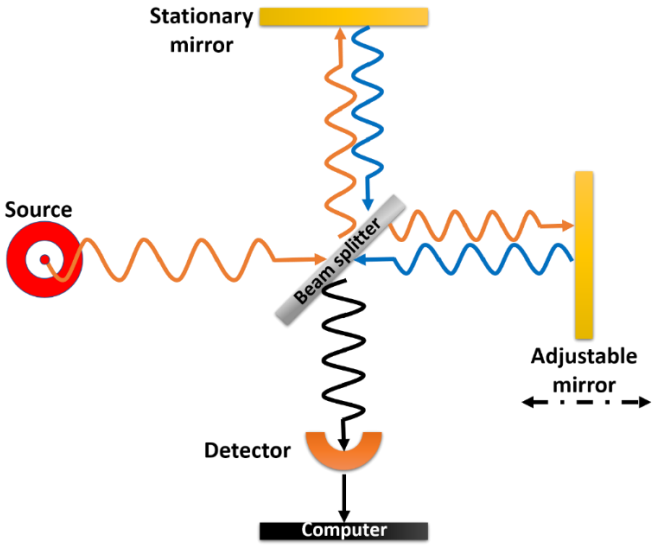

Figure 3.12 The elements of a simple interferometer system.

3.4 QCL fabrication results

The main purpose of characterising the fabricated THz QCL is to check if the performance of such devices can meet the proposed satellite mission requirements to be used as local oscillators to target dominant species of the Mesosphere lower thermosphere (MLT). The study will consider important parameters that address the proposed satellite THz payload requirements, by ensuring that the device will generate sufficient THz output power to 'pump' the mixer diode in the heterodyne system, typically at the milliwatt level, and to have narrow spectral emission signature. Similarly, an investigation for the double metal QCL will be undertaken in the following section to have a comparison between the two designs.

3.4.1 SI-SP QCL characterisation (G0109, 3.1 THz)

Firstly, the fabricated device in Section 3.1 that is based on SI-SP has been tested. The experiment of the LIV and spectra characterisation has been applied on the QCL device from the wafer G0109- 3.1 THz with hybrid active region design with dimensions of 2-mm length and 150-μm width.

The experiment is conducted in pulsed mode operation at different heat sink temperature to examine the LIV performance of the device as shown in Figure 3.13(a) and (b). The maximum power of the device that has been obtained at temperature 10 K was 45 mW with threshold current density of 135 A/cm^2. The threshold current density (J_{th}) is typically related to temperature by the phenomenological relationship:

$$J_{th} = J_o \, e^{\frac{T}{T_o}} \tag{3.1}$$

Where J_o is constant value, T_o is the characteristic temperature, and T is the range of the heat sink temperature varied between 10 and 110 K.

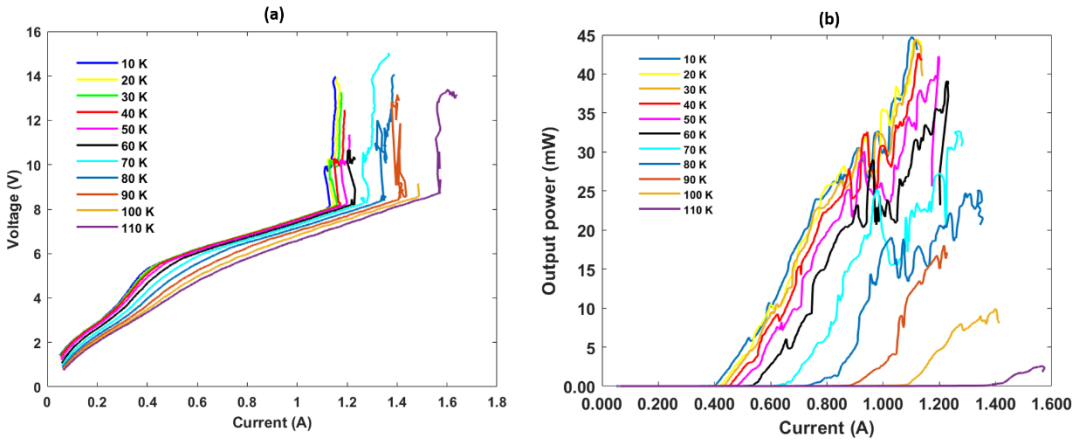

Figure 3.13 LIV characteristics of a SI-SP 3.1-THz QCL device at heat-sink temperature varied from 10–110 K. (a) operating voltage as a function of the drive current. (b) The actual output power as function of the QCL drive current.

This device worked at temperatures up to 110 K with 2.5 mW. The maximum power at 60 K, which is the temperature of the Stirling cycle cooler of the proposed satellite mission, is reached up to 39 mW. However, this would be lower when operating the QCL in CW mode due to the self-heating of the QCL but will still expected to have sufficient power for the system. Moreover, the output power decreased with a rise in heat sink temperature. To estimate the CW performance for the device, the temperature of the active region has been calculated as the following:

$$\boldsymbol{T_{\mathrm{AR}} = T_{\mathrm{heat-sink}} + (R_{\mathrm{Th}} IV)} \qquad (3.2)$$

Where, R_{Th} is thermal resistance. Typically, R_{Th} ≤ 10 K/W, so a worst-case estimated for performance is $T_{\mathrm{AR}} = T_{\mathrm{heat-sink}} + (10IV)$.

The active region temperature at 10 K heat-sink temperature is found to be 32 K at the threshold current and reach up to 97 K at the maximum power as shown in Figure 3.14(b). This imply that the device could be work in CW mode with limited operating temperature. The threshold current density was plotted as a function of heat sink temperature, observing an exponential increase with the temperature with $J_0 = 86\ \mathrm{A/cm^2}$ and $T_0 = 67\ \mathrm{K}$ as shown in Figure 3.14(a).

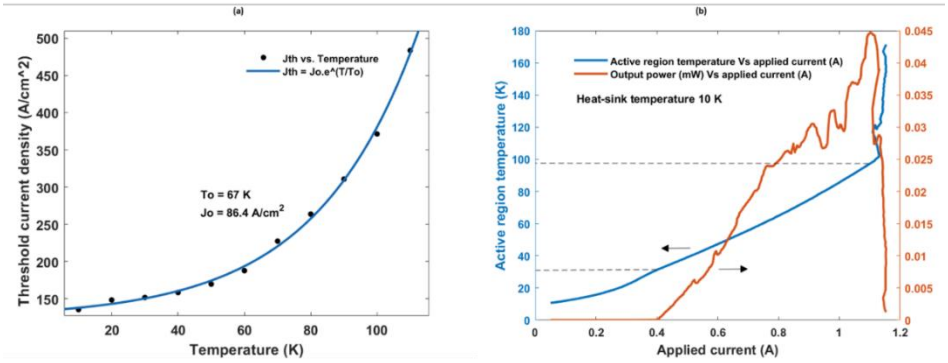

Figure 3.14 SI-SP 3.1-THz QCL temperature performance (a) Threshold current density as a function of heat-sink temperature in pulsed mode. (b) Estimated performance in CW mode showing the active region temperature rises after the threshold point up to the maximum.

The spectra, the spectra of the device have been obtained at four different drive currents starting above the threshold current and ending just below the rollover current as shown in Figure 3.15. The results that have been observed with fixed heat sink temperature at 6 K show multi-mode emission behaviour with central frequency at 3.069 THz. With an increase in drive current, the intensity of the emission increased with multi-mode behaviour observed between 3.02 and 3.15 THz. Such tunability is overrange the proposed satellite payload requirements, in which the desirable precision tunability for the LO needs to be around 1 GHz with single-mode behaviour. The mode index of the Fabry-perot waveguide has been calculated as the following:

$$\Delta \boldsymbol{f} = \frac{\boldsymbol{c}}{\boldsymbol{2nL}} \tag{3.3}$$

Where, Δf is the free-spectral range (i.e., the separation between the peaks), c is the speed of light, L is the cavity length. At 1-A drive current with 2-mm cavity length, the mode index has been found to be $n = 3.57$.

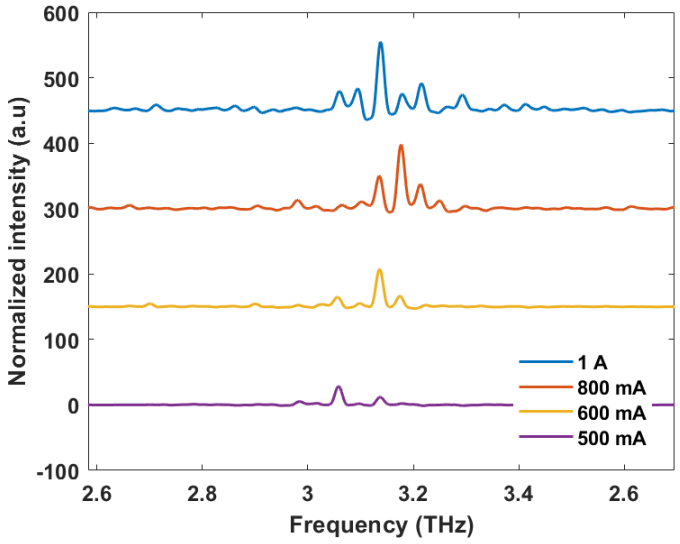

Figure 3.15 SI-SP 3.1-THz QCL device spectral measurements with range of drive currents varied from 0.5–1.0 A at 6-K heat-sink temperature. The vertical shift of the spectra is only for clarity and to make the multi-mode spectra obvious. The flat portions either side of the modes are all zero apart from the shift.

The following table summarise the most important factors of the SI-SP device.

Table 3.3. SI-SP QCL device performance.

Device dimension	2mm×150μm
Active region design	Hybrid
Max heat-sink temperature (K)	110
Max output power (mW) at 10K	45
Threshold current density (A/cm²)	135
Centre frequency (THz)	3.069
Mode behaviour	Multi-mode

3.4.2 Double-metal QCL characterisation (L1169, 4.7 THz)

The main reason for investigating the double-metal QCL design is that a higher operating temperature can be achieved due to the reduction of the self-heating of the device which results from the effect of the second metallic layer as mentioned previously in Chapter 2. In addition, single mode emission can be achieved by such design due to the strong confinement of the radiation. However, other issues will be raised related to the beam divergence, which will be discussed later. In addition, due to the strong confinement, the output power will be affected and reduced to a few milliwatts. LIV and spectral characterisation have been carried out on a double metal Au-Au QCL device from the wafer L1169 — 4.7 THz with hybrid active region design grown with MBE in the University of Leeds. The fabricated ridges that have been used have dimensions of 2-mm length and 125-µm width.

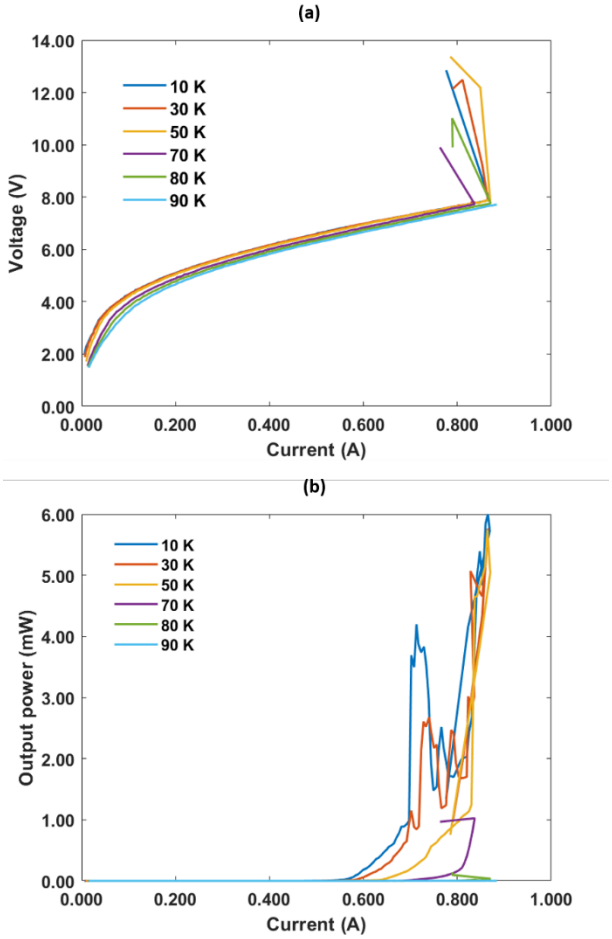

Figure 3.16 LIV characteristics of a DM 4.7 THz QCL device at heat-sink temperature varied from 10–90 K. (a) operating voltage as a function of the drive current. (b) The actual output power as function of the QCL drive current.

The experiment is conducted in pulse mode operation at different heat sink temperature to examine the LIV performance of the device as shown in Figure 3.16. The maximum power of the device that has been obtained at temperature 10 K was 6 mW. Despite the difference in frequency, when compared to the SI-SP QCL with the same active region design, we can see the big drop in terms of the output power due to the strong confinement of the

radiation in the DM waveguide, this would be even less if the device works in CW mode. The device worked at operating temperatures up to 80 K with 141 µW. The maximum power at 50 K is around to 5.7 mW and 1 mW at 70 K. The threshold current density showed exponential increase with the temperature with $J_0 = 197\ \mathrm{A/cm^2}$ and $T_0 = 162\ \mathrm{K}$ as shown in Figure 3.17. Thus, this active region design could work with higher temperature owing to the high value of T_0, which means the maximum operating temperature can potentially increase, conditioned with better fabrication quality.

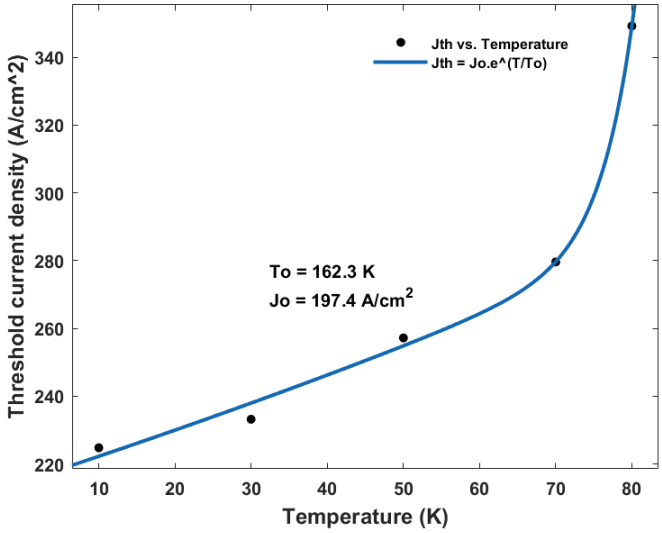

Figure 3.17 DM THz QCL threshold current density as a function of heat-sink temperature.

To check the performance of this device in CW operation mode, the power has been recorded as a function of the duty cycle varied from 2% up to 80%. The results shown in Figure 3.18 showed that the device will not be able to work in CW mode, because of the drop in the average power of the QCL as the duty cycle increased. It is thought that this is related to the n^+-GaAs above the active region being over etched. This would degrade performance by increasing the waveguide losses. Moreover, the active region temperature for the device is estimated using equation (3.2) to be between 42 and 78 K over the dynamic range of the device, with 10-K heat sink temperature, using a "worst-case" value of $R_{TH} = \frac{10K}{w}$. This estimation also shows that this device will not operate in CW mode or only could work with limited operating temperature.

Turning to the spectra measurements, the spectra of the device have been obtained as shown in Figure 3.19. The results that have been observed with fixed heat sink temperature at 5 K show single-mode emission at 4.793 THz at the maximum and slightly tuned to 4.786 THz by varying the driving current. This is about 7-GHz tunability, which seems to be desirable for the proposed satellite THz payload requirements.

The change in frequency is principally caused by the refractive index of the waveguide changing with temperature. The change in bias will also cause a small Stark shift as the subbands realign.

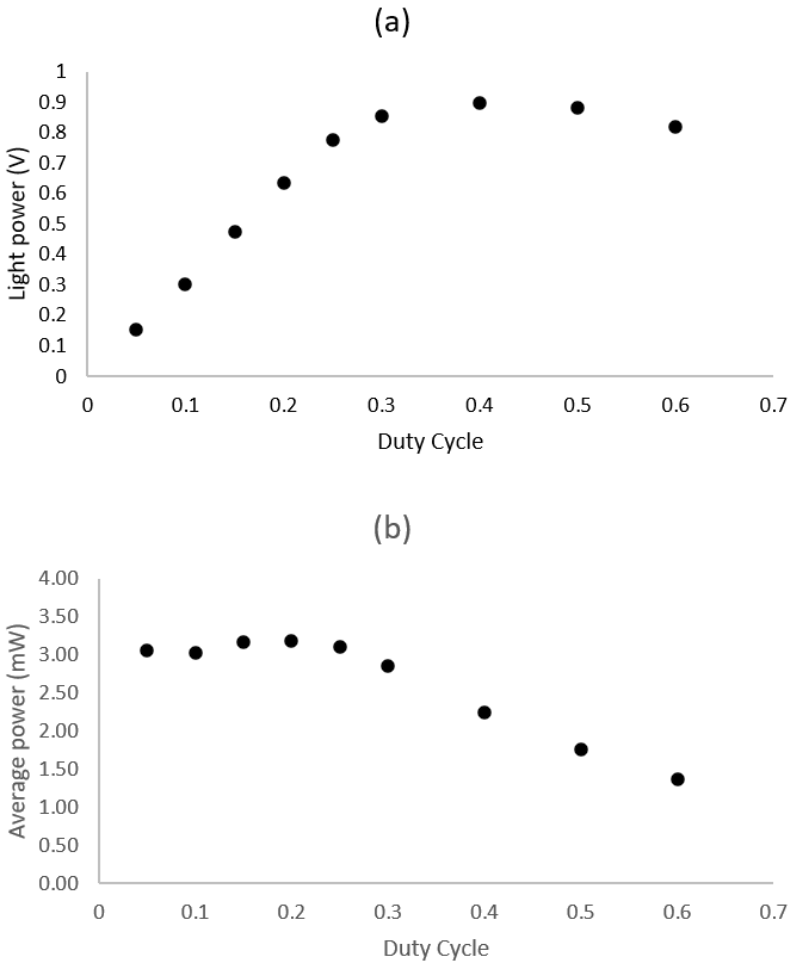

Figure 3.18 DM 4.7-THz QCL estimated performance for CW operation at 10 K. (a) Light power coming from the lock-in amplifier vs the duty cycle (b) The phase power as function of the duty cycle.

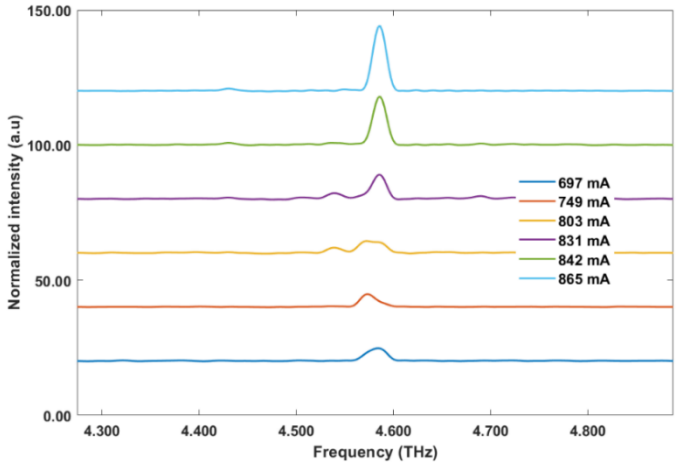

Figure 3.19 DM 4.7-THz QCL device spectral measurements with range of drive currents varied from 0.697–0.865 A at 10-K heat-sink temperature.

The following table conclude the most important factors of the DM QCL device.

Table 3. 4. DM-QCL device performance.

Device dimension	2mm×125µm
Active region design	Hybrid
Max heat-sink temperature (K)	80
Max output power (mW) at 10K	6
Threshold current density (A/cm^2)	224
Centre frequency (THz)	4.793
Mode behaviour	Single-mode

3.5 Summary

In this chapter, the two different methods of QCL fabrication have been explained with investigation of the QCL performance for each method. Even though the devices were with different frequencies, but a hybrid region design was used in both. The 3.1 THz SI-SP QCL provides more power and multi-mode behaviour with wide range tunability around 200 GHz, while the 4.7-THz DM QCL emits lower power at few milliwatts, but would provide single mode behaviour, which makes the DM more convenient for use as an LO for the proposed satellite mission.

Accordingly, the following chapter will focus on improving the output power of the DM QCL using different techniques. Using high-reflectivity coating at the back facet of the QCL would improves the output power as will be showed later in the following chapter. Another approach is to use Ag–Ag waveguide instead of gold; this is due to the electrical and thermal properties of silver, which have a higher conductivity than gold. This, in turn, could lead to an increase in the output power and a more efficient operating temperature of the device.

Chapter 4

Optimisation of THz Quantum Cascade Lasers

This chapter discuss methods for optimisation of the performance of the THz QCLs in terms of operating temperature and output power. The first method used is the high reflectivity (HR) optical coatings that would help to reduce the self-heating temperature and minimize the power dissipation of the device. The second method is related to the material of the cladding material for the active region of the device, by using the silver compared with the gold to increase the operating temperature of the device and increase the output power.

4.1 High-reflectivity facet coating

One of the advantageous methods that is used to optimise the performance of the lasers in terms of minimising the power dissipation and reduce the self-heating temperature is the use of high reflectivity (HR) optical coatings on one of the QCL facets. Using such technique would also allow them to reduce the cavity length to a smaller size and reduce the power consumption, which is desirable for the integration of the QCL for the proposed satellite payloads that has been mentioned previously in Chapter 1.

The HR coating can be classified as either dielectric coatings, e.g. Al_2O_3/Si, or metal-on-insulator coatings, e.g. Al_2O_3/Ti/Au and SiO_2/Au. For QCL optimisation, the metal-on-insulator coatings is more appropriate, in which the rear facet is coated and would provide about 99% reflectivity [105]. Due to the long wavelength of the THz QCLs, the dielectric coatings are impractical because the practicality and reflectivity will be limited, because the coating thickness is scaled in proportion to the wavelength. The composition of the coating is made with corresponding to the wavelength emission by using a thin dielectric layer with low optical absorption insulates the high reflective metal from the laser facet. Using such technique would increase emitted power from a specific facet as reported in [88], in which they achieved a peak power ~1.01 W (at 10 K) by coating the rear facet with SiO_2(150 nm)/Ti(10 nm)/Au(150 nm)/SiO_2(200 nm), deposited by an electron beam evaporator.

Accordingly, in this section we report characterisation of GaAs-based QCLs that have been tested in Chapter 3 (L1169) with and without a metal-on-insulator HR coating. We show that the presence of the coating improved the laser performance in terms of power. Before that, the threshold gain for the device has been predicted twice, once without the coating material, and once with the coating applied to one facet. This is done through multiple equations, by calculating the mirror losses first for the two devices using the following equation:

$$\boldsymbol{R_1 = R_2 = \left(\frac{n-1}{n+1}\right)^2} \qquad (4.1)$$

Where R_1 and R_2 are the reflection percentage of the device facets, *n* is the refractive index of the material. In the first case without coating, $R_1 = R_2$ for the GaAs, and the calculated value found to be 0.323, which means each facet has a reflection of 32.3%, while the reflectivity for the coated device based on SiO_2/Au is assumed to be 100%. It is important to note that this expression refers to optical interfaces with areas larger than the wavelength. As such, it only provides an approximation to the QCL facet reflectivity. The second step is to calculate the mirror losses for both devices using the following equation:

$$\boldsymbol{\alpha_{\mathrm{m}}} = \frac{\mathbf{1}}{\mathbf{2}\boldsymbol{L}} \boldsymbol{In}\left(\frac{\mathbf{1}}{\boldsymbol{R_1 R_2}}\right) \tag{4.2}$$

Where, α_m is the mirror loss, L is cavity length. Here, α_m is defined as the effective losses distributed across the device. The mirror loss for the uncoated device with 2-mm length is found to be 5.6 cm^{-1}, and for the coated device is 2.8 cm^{-1}. Accordingly, the threshold gain for both devices has been calculated using the following equation:

$$\boldsymbol{g_{\mathrm{th}}} = \frac{\boldsymbol{\alpha_{\mathrm{w}}} - \boldsymbol{\alpha_{\mathrm{m}}}}{\boldsymbol{\Gamma}} \tag{4.3}$$

Where, g_{th} is the threshold gain, α_{w} is the waveguide losses which is about 18 cm^{-1} as calculated in [106] for double metal device with 10-µm active region thick. Γ is the confinement factor and it is almost 1 for the double metal devices. Therefore, the threshold gain for the uncoated device has been predict it to be 12.4 cm^{-1}, whereas for the coated device is predicted to be 15.2 cm^{-1}, representing 18% improvement which indicates that the use of such technique would increase the output power of the device.

The fabricated device from L1169 wafer is loaded into the chamber of e-beam evaporator with a facet side facing toward the evaporation source. The coating is programmed and is carried out accordingly when based vacuum is reached. The material SiO_2/Ti/Au/SiO_2 with thickness 165 nm/12 nm/150 nm /60 nm, respectively.

LIV characterisation has been carried out on fabricated ridges that have same dimensions that have been used with the uncoated device, which is 2-mm length and 125-µm width.

The experiment is conducted in pulse mode operation at different heat sink temperature to examine the LIV performance of the device as shown in Figure 4.1. The maximum power of the device that has been obtained at temperature 10 K was 6.5 mW. Compared with the uncoated device, this device worked with operating temperatures up to 70 K with 2.1 mW and just few microwatts only at 80 K. The threshold current density showed exponential increase with the temperature with $J_0 = 187.6\ \mathrm{A/cm^2}$ and $T_0 = 108.15\ \mathrm{K}$ as shown in Figure 4.2.

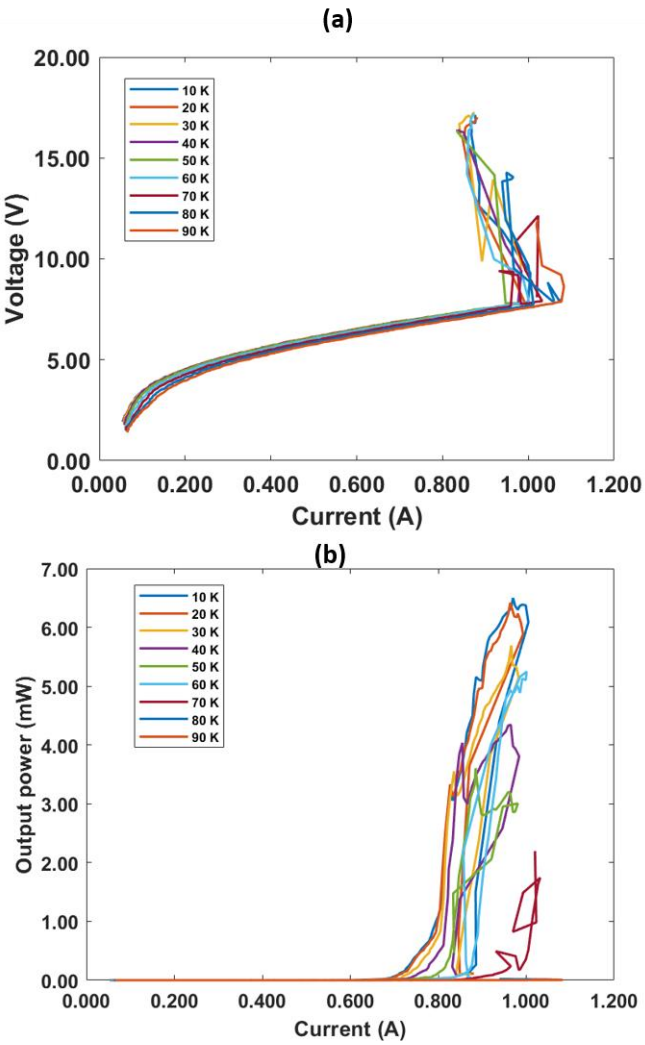

Figure 4.1 LIV characteristics of a DM 4.7 THz QCL device with HR coating at heat-sink temperature varied from 10 K to 90 K. (a) operating voltage as a function of the drive current. (b) The actual output power as function of the QCL drive current.

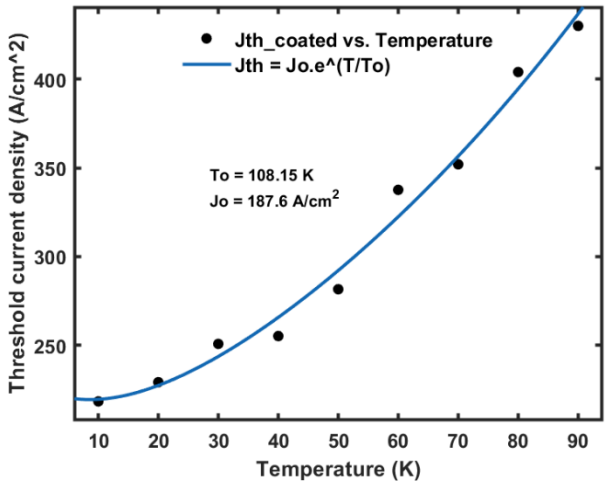

Figure 4.2 DM THz QCL with HR coating threshold current density as a function of heat-sink temperature.

As can be seen from Figure 4.3, the use of the HR coatings led to an increase in the output power by 8%, in which the maximum power of the device that has been obtained at temperature 10 K with the facet coating is 6.5 mW and was 6 mW without the coating. However, this increase in power came at the cost of decreasing the maximum operating temperature of the device, which is for the uncoated device worked up to 80 K with 141 µW, while for HR coated device 18 µW at the same temperature. Table 4.1 shows a brief comparison between the two devices. A systematic further study would be required to eliminate variation in thermal resistance between different fabrication runs.

Table 4.1 Comparison between the coated and the uncoated DM-QCL devices.

DM-QCL	Maximum power at 10 K	Maximum power at 80 K	characteristic temperature T_o	J_o
Normal facet	6 mW	141 µW	162 K	197 A/cm^2
HR coating facet	6.5 mW	18 µW	108 K	188 A/cm^2

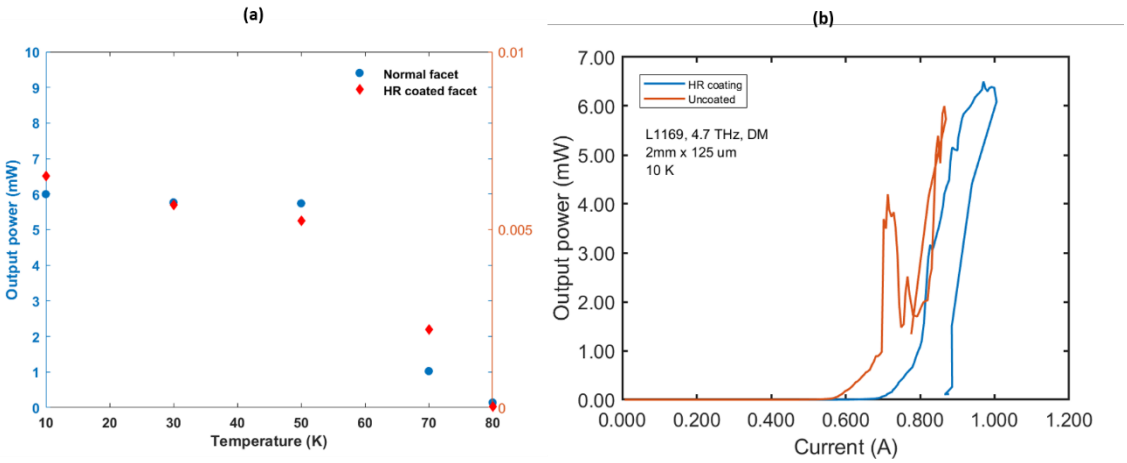

Figure 4.3 Output power from coated and uncoated DM QCLs (a) as a function of operating temperature. (b) as a function of drive current at 10 K.

4.2 THz QCL optimisation using Ag-Ag waveguide

The performance of THz QCLs is directly affected by low loss waveguides at high operating temperatures, making them able to provide high output power at higher operating temperature conditions compared with the other waveguides. Thus, their practicality would make them desirable for applications such as using them as local oscillators for astronomic instrumentation and THz imaging [103].

To do that, different waveguide metals have been investigated. In this section, we experimentally compare the performance of THz QCL processed

in DM waveguide devices based on two different materials, gold, and silver. Comparing the two metals, the electrical and thermal conductivities of the silver (Ag) is higher than the gold (Au) at room temperature as reported in [103], and that would provide lower-loss waveguide.

The experimental results obtained in [103] show that the active region design of the THz QCL is a significant reason for the performance improvements obtained in Ag-based devices, in which they deduced that an improvement in high-temperature performance can be potentially achieved by utilizing silver based waveguides, with improvements of 5 K in the maximum operating temperature [103]. They also show that the peak output powers increased by 40% and for the Ag-based device, and has lower threshold current density compared with the Au-based one [103]. Another study shows that the use of Ag-based QCL reduces losses by 2–4 cm^{-1} in comparison with Au-based QCL, with maximum operation temperature 10 K higher than for laser with Au-based QCL [107]. Ag-based waveguides are, however, more challenging to fabricate, owing to their tendency to oxide rapidly.

To investigate that, several identical laser ridges with three different widths were fabricated on two chips from the same wafer, one is with an Au-based for the top and bottom cladding material, and the other with an Au-based waveguide. The devices were fabricated together except for the metallization stage, in which different recipe were used for the Ag-based device. As before, wet chemical etching was used to define the lasers ridges. The metallisation recipes were Ti/Au (15/200-nm) layers deposited for Au-based waveguides. In case of using silver as the cladding material, the wafer bonding would be harder to achieve due to the high temperature melting point of the silver, which is about 962°C, which considered as a drawback of the silver. To avoid this issue, the formation of the bottom cladding of the Ag-Ag waveguide is made using Electron Beam Evaporator, by using Titanium and silver first (Ti/Ag) with thicknesses 10 nm/200 nm, respectively. During the device processing, a potential oxidation issue may appear due to the chemical reaction, which considered as another drawback of the silver, makes the Ti/Au overlayer as shown in Figure 4.4 work as a protection layer for the silver from any oxidation that might happen, and to make the bonding process easier so that the melting point will be as before for the Au instead of silver. Thus, the Ag-based waveguides Ti/Ag/Ti/Au (15/200/15/200-nm) layers were used.

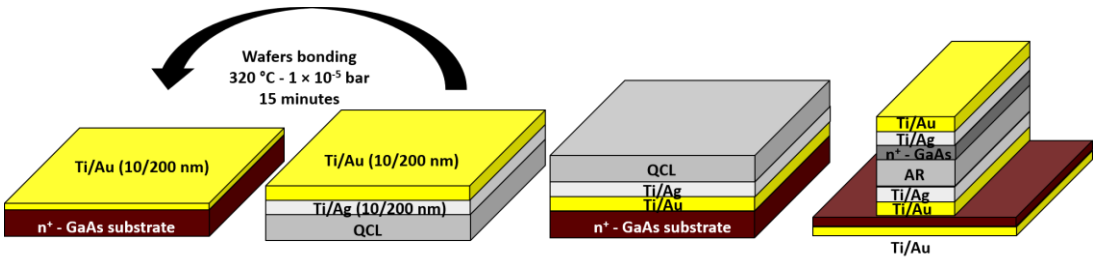

Figure 4.4 Illustration of the Ag-Ag QCL fabrication process. All the stages and fabrication techniques that illustrated in Section 3.2 for the Au–Au waveguide are the same, except the metallisation process for the top and bottom cladding layers.

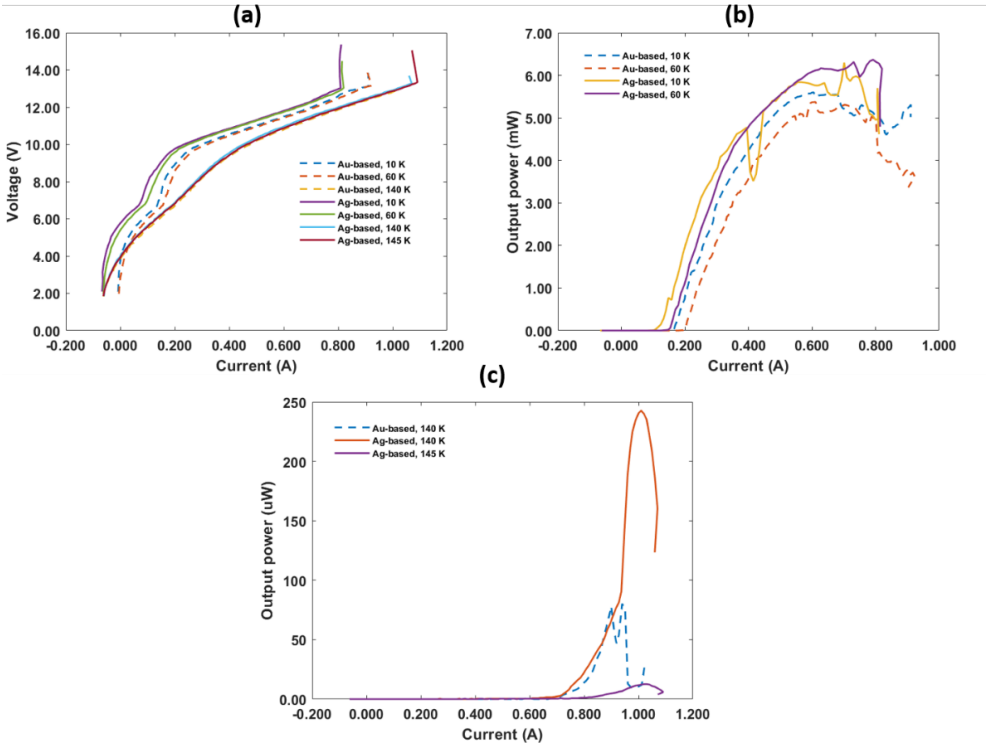

Figure 4.5 LIV characteristics of Au-based and Ag-based QCLs. Both devices have dimensions 1.5-mm length × 100-µm width. (a) IV curve for both devices at different operating temperature. (b) LI curve for both devices at 10 K and 60 K. (c) LI curve for both devices at temperature 140 K and 145 K.

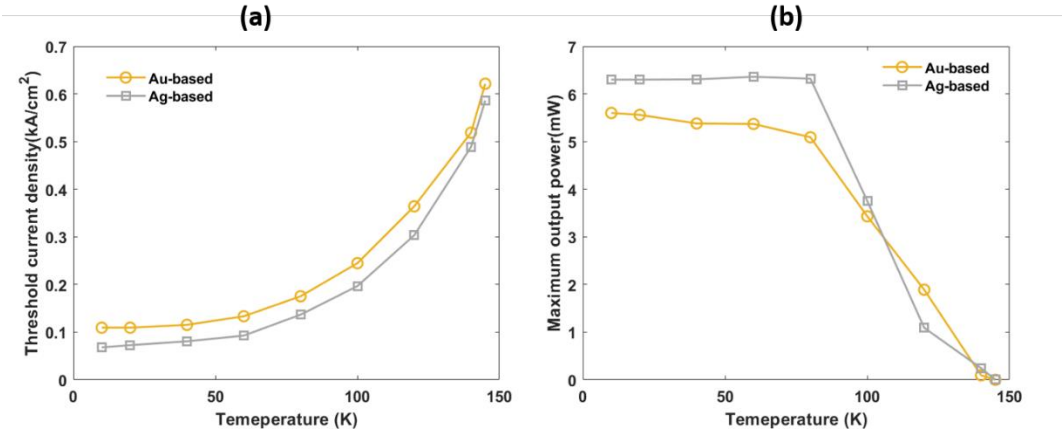

Figure 4.6 The temperature evolution for Au–Au and Ag–Ag devices (a) Threshold current density vs the operating temperature shows lower density for the silver-based device. (b) Maximum output power vs operating temperature shows higher output power at low temperatures also at high temperatures.

The device performance is compared in Figure 4.5 and Figure 4.6 for the Au-based and Ag-based devices of 1.5-mm ridges length, and 100-µm width.

The measured data listed in Table 4.2 show that the Ag-based device yield a significant drop in the threshold current and dramatic improvement in the output power at higher heat sink temperatures, it also has a higher maximum lasing temperature, higher output power and lower threshold current density compared to the identical Au-based device, which means that Ag-based

waveguides exhibit lower losses than Au-based waveguides, which agrees with the waveguide analysis presented in [103]. Their maximum operating temperatures were determined to be 140 K and 145 K, representing a 5-K increase for the Ag-based device. At a temperature of 10 K, the peak output powers are 5.6 mW and 6.3 mW, respectively, representing a 11% increase for the Ag-based device. The difference between the threshold current density is 44 A/cm^2. The increase in the peak output power between the Ag-based device compared with the Au-based device agrees well with the modelling results reported in [103].

Table 4.2 Summary of Au-based and Ag-based QCL performance

Waveguide material	T (K)	J_{th} (A cm^{-2})	P_{out}
Au–Au	10	111	5.6 mW (max)
Au–Au	60	134	5.4 mW
Au–Au	140 (max)	521	81 µW
Ag–Ag	10	67	6.3 mW (max)
Ag–Ag	60	93	6.3 mW
Ag–Ag	140	489	243 µW
Ag–Ag	145 (max)	586	3 µW

The emission spectra of the two devices shown in Figure 4.7 are almost the same, and only 30-GHz difference between the two devices, which point out that only a small influence on the electrical conduction and the net gain spectra is affected by Ag waveguide. The emission of the Au-based is centred at 3.27 THz and tuned about 90 GHz, while Ag-based centred at 3.3-THz and tuned about 100 GHz after the roll-off point.

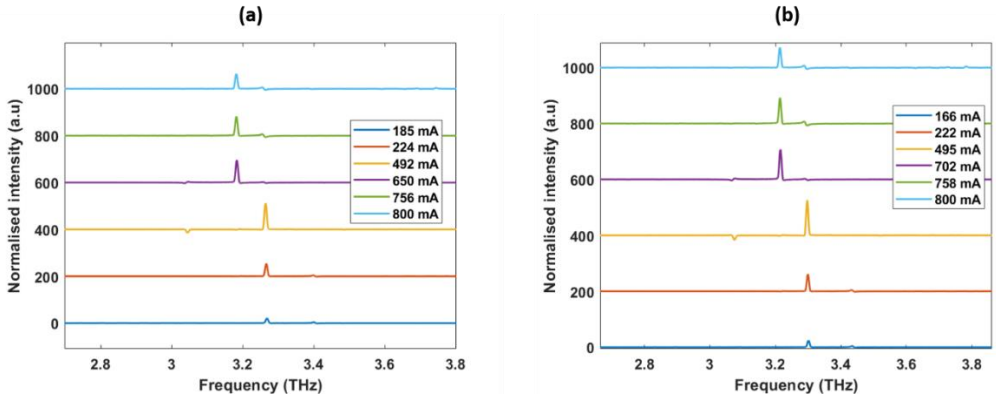

Figure 4.7 The emission spectra at 10 K of (a) Au-based QCL. (b) Ag-based QCL.

4.3 Summary

Optimization methods which aim to improve the performance of THz QCLs in terms of operating temperature and output power have been discussed, by applying high reflectivity (HR) optical coatings to reduce self-heating temperature and reduce the dissipation of the system. The other technique is based on modifying the form of metal cladding that covers the active region from the top to the bottom, by using the silver as an alternative to the gold.

Due to COVID-19 situation, the number of devices that have been measured in this chapter is limited. To be able to publish these results, more measurements for more devices are needed to confirm the results presented in this thesis and ensure the producibility for such methods.

Chapter 5

Waveguide integration analysis

There is considerable scientific interest in studying the abundance of key gas species (e.g., O and OH) within the mesosphere–lower thermosphere (MLT) region of the Earth's atmosphere, in part because there is a strong indication that these provide a highly sensitive indicator of climate change. The proposed satellite THz payload aims to observe these gases by limb-sounding from low-Earth orbit to record their emission spectra using four receiver channels in the 0.8–4.7-THz band [60]. The system comprises two novel terahertz-frequency (THz) radiometers, in which THz quantum cascade lasers (QCLs) will be exploited as local oscillators (LOs) at 3.5 THz and 4.7 THz, owing to their high THz output power (> 1 mW continuous-wave), narrow intrinsic linewidths [108] (~20 kHz) and compact size (~1 mm).

Therefore, the main objective from this chapter is to analyse the propagation of the electromagnetic field within a proposed waveguide design that will be used to integrate the QCL with other system components in the proposed payload.

5.1 QCL waveguide integration

Although the double-metal QCL ridge-waveguide provides good THz power and thermal performance, such designs show very high beam divergence and poor far-field beam quality as a result of the sub-wavelength radiation confinement, resulting in poor coupling to external optical systems [109]. This makes it appropriate for the near-field radiation coupling and weak for external free-space coupling.

Accordingly, a new packaging and waveguide-integration design needs to be made to make a reproducible system for integrating a mechanically robust THz QCL that has the capability to couple efficiently with external waveguides and mixers, and with good quality beam profile [110]. Thus, several techniques have been utilized to optimise the beam profile and coupling following different approaches. The outcoupling power of the THz QCLs radiation has been considerably improved using third-order distributed feedback (DFB) grating technique as demonstrated in [111] or using a simple one-dimensional grating design to collimate the beams of the THz radiation by sculpting designer spoof surface plasmon structures as reported in [112]. even though the patterned far-field beam profile has been reshaped into a narrow beam of ~10° divergence for both techniques, both follow device patterning approaches which that makes them relatively complex and unsuited to be reproduced. Another approach demonstrates an optical engineering of lens-coupled metal–metal waveguide, in which good beam profile at the far-field and high-power levels can be achieved [113]. Another work show an improvement on the beam pattern and obtained high optical output power using pyramidal structures [114]. However, they still have issues

in terms of reproducibility and mechanical robustness along with the complexity of their fabrication.

Therefore, a new approach has been demonstrated in [110], in which the THz double-metal QCL is ribbon bonded to a direct current (dc) strip-line within a copper (Cu) heat-sink enclosure containing a rectangular cross-section metallic waveguide. The radiation from one facet of the QCL is guided through a rectangular cross-section waveguide, which is precision-micro machined into the block. Comparing with the previous techniques discussed above, this scheme results in a significant improvement in beam divergence to < 20°. Nevertheless, the out-coupled power from such designs is poor and key development challenges remain though, including stabilizing the emission frequency of the QCL, and improving the beam-profile and the coupling of THz radiation between the QCL and other system components. However, such a technique is based on highly reproducible mechanical microfabrication that supports the integration between a THz QCL and mixer, and opens the way towards the development of a mechanically micro-machined waveguide cavity containing dual diagonal feedhorns [115]. The horn antenna is used to match the impedance of the waveguide to that of free space and ensure a smooth transition, while also the undesirable modes of the signal are being eliminated to get a more efficient emission of radiation [116]. In addition, this kind of feed type has been selected to allow easier machining and integration with the QCL block. There are different types of the feedhorn that can be used such as the corrugated conical and the smooth wall conical feedhorn which have been investigated in different studies [117], [118] and showed very good performance in terms of coupling efficiency that reached up to 96% with low loss and circular radiation pattern. However, at THz frequencies, the dimensions of both waveguide and feedhorn become very small and encounter a complexity and challenge of mechanical fabrication techniques, makes the diagonal feedhorn antenna preferable.

Thus, the development of a dual feedhorn integration technique has been investigated and analysed [115]. Using such technique proved that the QCL output signal could be enhanced along with the beam quality. Such small and robust mechanical assembly integration, easier compared with the other feedhorn types, provides an efficient electromagnetic interface with free space. Moreover, the dual feedhorn integration technique enables access to both QCL facets simultaneously.

Figure 5.1 shows the internal structure of a precision micro-machined copper block containing a 3.3-THz QCL mounted in a rectangular waveguide with cross-sectional dimensions of (160 × 80) μm^2. The waveguide feeds into a diagonal feedhorn with a (1.56 × 1.56) mm^2 square aperture at either end, enabling the free-space THz emission to be coupled simultaneously to a mixer and a frequency-stabilization subsystem. The machining process has been done using a precision mill to form the waveguide into the copper block [115]. The formation of the two diagonal feedhorn were identical at either end of the waveguide with slant angle of 7.5°. To improve the heat-sink temperature and make it suitable for the cryogenic cooler, the copper block was coated with

gold after the machining process, this also would prevent any corrosion might arise on the block. A stage of heat sinking was placed between the QCL and the bias connection of a standard SMA connector. As opposed to the QCL heat-sink, this area is designed to remove heat conducted through the bias cabling from outside the cryostat. The stage links all the parts using a series of wire bonding steps as shown in Figure 5.1.

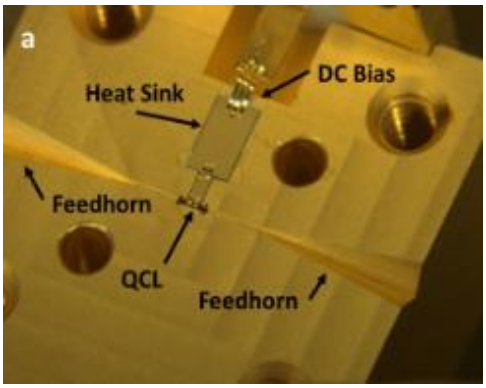

Figure 5.1 QCL mounted within a dual-feedhorn waveguide block [115].

5.2 Beam profile measurements:

The experiment setup that has been conducted in RAL is shown in Figure 5.2(a), in which the output radiations of the QCL from the dual-feedhorns was reflected by two plane mirrors inclined at 45° and located about 5 mm away from the apertures. The two signals are then recorded using a raster scanned Golay detector located about 70 mm away from the mirrors [119]. Thus, the THz emission intensity and the beam profile of the antenna has been measured in a rectangular coordinate reference plane aligned orthogonally to the direction of signal by taking a series of discrete sampling with step interval of 5 mm in both axes. The experimental results in Figure 5.2(b), as reported in [119] show bright central maxima and exhibit a near symmetrical diffraction pattern with a beam divergence of about 5° for the two signals, confirming that there is an equal power distribution between the two facets, and that each aperture is excited approximately uniformly by the QCL. In addition, the feedhorn has been shown to improve power outcoupling and beam divergence of the QCL [120], but in order to optimize the far-field beam-profile, an electromagnetic model is needed.

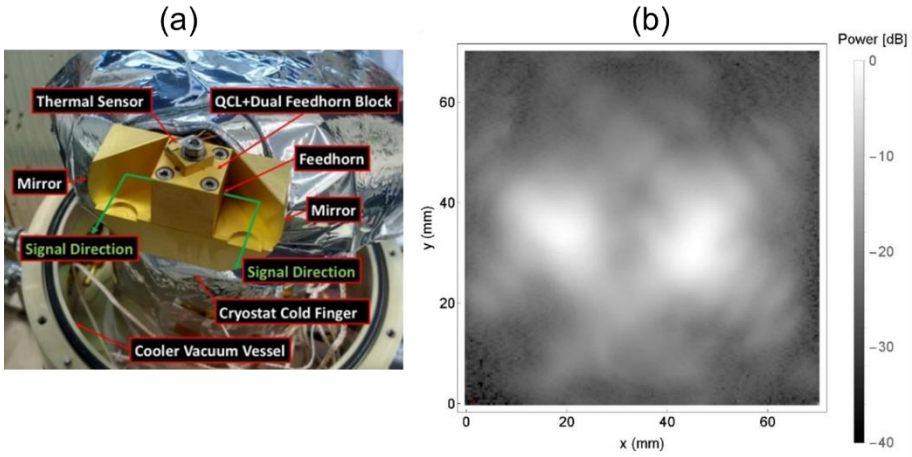

Figure 5.2 Beam-profile measurements of dual-feedhorn QCL block. (a) The complete precision micro-machined copper block containing a 3.3-THz QCL installed on a cryostat cold finger with the set-up measurements. (b) Far-field beam pattern obtained at 70-mm shows two central maxima corresponding to dual output of QCL with sidelobe typical of diagonal feeds.

5.3 Simulation method

We are aiming to simulate the propagation of the QCL radiation in a single diagonal feedhorn structure to provide an analysis of the beam profile and the transmission of THz power through the waveguide. To do that, a hybrid modelling approach has been developed, to enable accurate yet fast simulation.

Firstly: We used High Frequency Structure Simulator (HFSS) finite-element model to simulate a three-dimension (3D) QCL structure with bulk active region placed inside a 3D rectangular waveguide structure. This aims to find important parameters that we want to compare with the designed diagonal feedhorn and see how the performance of these parameters will improve. These parameters are the beam-profile of the double-metal QCL and its divergence in the free-space, and the radiated power of the QCL.

Secondly: An analytical simulation has been developed to analyse the electric field in the far-field region, based on a Fraunhofer diffraction approximation for a square aperture with a uniform electric field. This aims to provide an overall Illustration of an equivalent feedhorn structure in terms of beam-profile and compare it with integrated QCL in a rectangular waveguide.

Thirdly: In HFSS, the designed 3D QCL is now placed inside a 3D rectangular waveguide structure that feeds into a diagonal feedhorn. The simulation aims to show the field excitation across the QCL facet that propagates through the waveguide and feedhorn, to determine the near-field pattern. Then, instead of using the uniform electric field in the analytical simulation, we export the complex electric field from the HFSS to a 2D Fourier transform to find the corresponding far-field which will allow us to understand and analyse the far-field propagation of the radiation for such design. To find

the optimum design, the results have been predicted at different model dimensions as we will see in Section 5.3.4.

5.3.1 High Frequency Structure Simulator

High-Frequency Structure Simulator (HFSS) is a software to provide full-wave electromagnetic (EM) field simulation for 3D volumetric passive device modelling. Antennas, filters, IC packages, and other wide range of high frequency products can be designed and analysed with this simulation tool [121]. By utilising a Finite Element Method (FEM) method, the solution can be found for the field within a collection of tetrahedra that are formed by subdividing the design structure into small subsections. The field solution for the whole structure is then obtained using Maxwell's equations and thus the S-parameters is determined. Moreover, the solution's accuracy is acquired using a convergence of an iterative refinement technique, in which it is localised in regions with high error field solution. Thus, HFSS is considered as an integrated simulation that combines modelling, visualization, solid modelling, and automation in an easy-to-learn environment. This will enable engineers to acquire the solution of any high-frequency design quickly and accurately.

To create a design, it must involve a Parametric Model Generation by creating the geometry of the model and defining its boundaries and excitations. In the analysis step, the solution setup and frequency sweeps need to be defined, which is done by choosing the solution type to define the type of the result that we want. There are three available solution types in HFSS, which are: driven model, driven terminal, and eigenmode. In the driven model, the solutions are expressed in terms of the incident and reflected powers of waveguide modes to calculate the S-parameters of the model. In the driven terminal, the solutions are expressed in terms of terminal voltages and currents to calculate the terminal-based S-parameters of multi-conductor transmission line ports. The resonant frequencies of the structure and the fields at those resonant frequencies can be obtained using the last solution type, which is the eigenmode. The solution process is fully automated in HFSS and the design is analysed through the solve loop as shown in the flowchart. Finally, the results can be obtained in 2D or 3D report and field plots.

5.3.2 3D Geometry design

The structure of the waveguide integration system has been designed in HFSS through three main stages, which are the QCL, the rectangular waveguide and feedhorn antenna, and the boundaries of the design.

Firstly, the 3D QCL structure has been done based on 3 materials in HFSS, the substrate of the QCL defined as GaAs, the top and bottom gold layers, and the QCL active region. The QCL active region has been defined in HFSS as a bulk material by calculating the average permittivity of the whole device which is given by the interpolation between the wells and barriers of the device.

The detailed layers of the device that has been used to make the bulk material is shown in Table 5.1.

Table 5.1 The detailed layers of the active region for a 3.3-THz QCL device.

Composition	Thickness (nm)	Doping concentration (cm^{-3})
$Al_{0.18}Ga_{0.82}As$	3.8	0
GaAs	10.8	0
$Al_{0.18}Ga_{0.82}As$	0.5	0
GaAs	12.6	0
$Al_{0.18}Ga_{0.82}As$	1	0
GaAs	12.9	0
$Al_{0.18}Ga_{0.82}As$	1.9	0
GaAs	11.3	0
$Al_{0.18}Ga_{0.82}As$	2.9	0
GaAs	9.1	0
$Al_{0.18}Ga_{0.82}As$	2.9	0
GaAs	8.2	0
$Al_{0.18}Ga_{0.82}As$	2.9	0
GaAs	6.8	0
$Al_{0.18}Ga_{0.82}As$	2.9	0
GaAs	16.3	3×10^{16}
$Al_{0.18}Ga_{0.82}As$	2.9	0
GaAs	14.2	0
Total	123.9	

To calculate the average doping of the device, we use the following equation:

$$\boldsymbol{N_{\mathrm{avg}} = N_{\mathrm{doped}} \times \left(\frac{L_{\mathrm{doped}}}{L_{\mathrm{total}}}\right)} \quad (5.1)$$

Where, N_{doped} is the volume-doping density within the doped region of the device (3×10^{16} cm^{-3}), L_{doped} is the length of the doped region (16.3 nm), L_{total} is the total length of one period of the device (123.9 nm). Based on that, we calculate the permittivity of both GaAs and the AlAs using a Drude model [72]. Now we have the wells permittivity, which are made of just doped GaAs, we calculate the barrier permittivity which is given by the interpolation between the GaAs and AlAs values as the following:

$$\boldsymbol{\varepsilon_{\mathrm{barriers}} = \varepsilon_{\mathrm{AlAs}} x + \varepsilon_{\mathrm{GaAs}}(1 - x)} \quad (5.2)$$

Where, $\varepsilon_{\mathrm{barriers}}, \varepsilon_{\mathrm{AlAs}}, \varepsilon_{\mathrm{GaAs}}$ are the permittivity's of the barriers, AlAs, and GaAs, respectively. $x = 0.18$ is the aluminium fraction within the barriers.

Now we have calculated the permittivity of the barriers and wells, we can calculate the average permittivity of the whole device as the following:

$$\boldsymbol{\varepsilon_{\mathrm{avg}} = \frac{\varepsilon_{\mathrm{barriers}} L_{\mathrm{barriers}} + \varepsilon_{\mathrm{wells}} (L_{\mathrm{total}} - L_{\mathrm{barriers}})}{L_{\mathrm{total}}}} \quad (5.3)$$

The QCL is now completed with length, width, and thickness (1.5 mm × 125 µm × 12 µm) respectively. The QCL is then placed in a

vacuumed WM-130 rectangular waveguide structure (130 × 65)- μm^2 based on the IEEE standard, and with 2-mm long. This is feeds into a diagonal feedhorn with a (1.556 × 1.556)-mm^2 square aperture at the end as shown in Figure 5.3.

In HFSS, the designed structure is treated as a closed model, in which the energy is totally confined within the model due to the perfect electric conducting boundary in the solution space, and it only escapes through an applied port. Thus, the behaviour of the electromagnetic field on the object interfaces and at the edges of the model needs to be defined using a specified boundary condition to create an open model. Therefore, the vacuumed rectangular waveguide and feedhorn antenna is placed inside a perfect electric conducting box surrounded by another box of air to define the radiation boundary as shown in Figure 5.3. This allows electromagnetic waves to radiate into space and thus getting the behaviour of the near-field beam profiling for the model. It is important to mention that a high-performance computer is needed to run such simulation to get high resolution by solving small meshes for the structure at THz frequency.

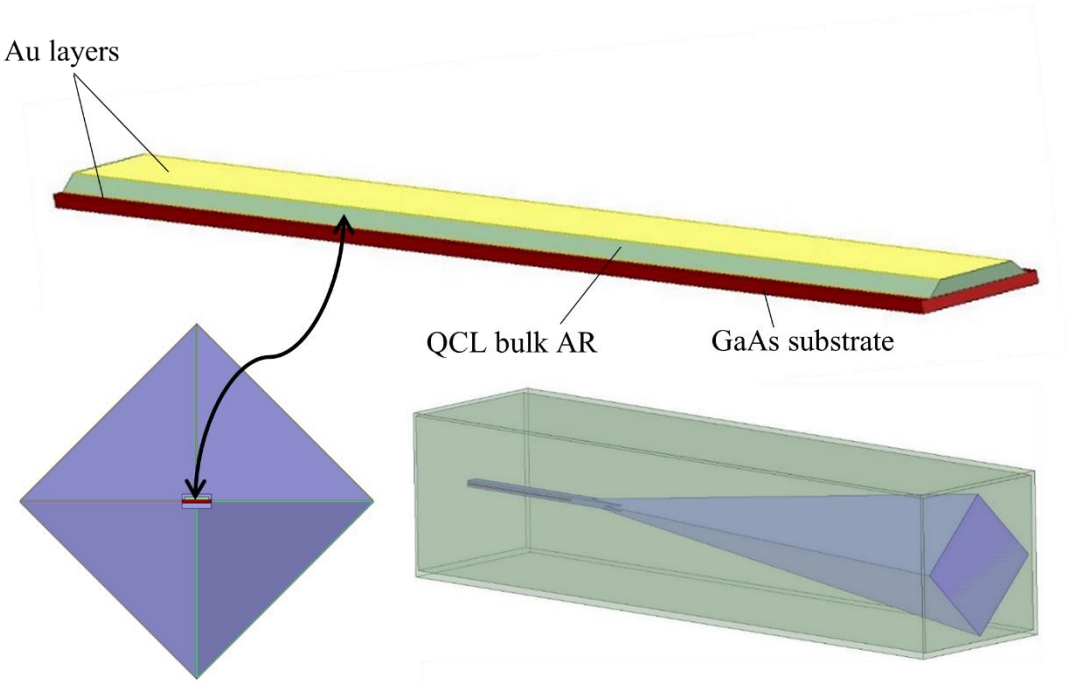

Figure 5.3 Side view of the model design in HFSS showing the bulk structure of the QCL integrated inside the waveguide, and the complete 3D diagonal feedhorn waveguide structure in the HFSS with a perfect electric conducting box surrounded a radiation box.

5.3.3 Analytical and semi-analytical Fourier transform simulation

A 2D Fourier transform is then used to find the corresponded far-field pattern based on the complex electric field from the HFSS model. To do this, we calculate the form-factor that describe the shape of the far-field for the aperture using the form-factor equation from Ulaby's textbook [122] as the following:

$$\tilde{\boldsymbol{h}}(\boldsymbol{\theta},\boldsymbol{\phi}) = \iint_{-\infty}^{\infty} \tilde{\boldsymbol{E}}_{\mathrm{a}}(\boldsymbol{x}_{\mathrm{a}},\boldsymbol{y}_{\mathrm{a}}) \,.\, \boldsymbol{e}^{[\mathrm{j}\boldsymbol{k}\sin\boldsymbol{\theta}(\boldsymbol{x}_{\mathrm{a}}\cos\boldsymbol{\phi}+\boldsymbol{y}_{\mathrm{a}}\sin\boldsymbol{\phi})]}\, \boldsymbol{dx}.\boldsymbol{dy} \tag{5.4}$$

Where $(\tilde{E}_{\mathrm{a}})$ is the complex electric field, $\tilde{h}$ is the form factor, (θ,ϕ) are the angles between the antenna and the far-field observation plane in the horizontal and vertical directions respectively, k is the wave vector, and $(x_{\mathrm{a}}, y_{\mathrm{a}})$ are respectively the horizontal and vertical coordinates across the antenna aperture. Therefore, the equation performs a 2D Fourier integral of the electric field across the whole of the aperture. Then, we find the angles between the antenna and the far-field observation plane (θ,ϕ) at a specific radiation frequency f with wave-vector given by $k = \frac{2\pi f}{c}$ as the following:

$$\boldsymbol{\theta} = \tan^{-1}\left(\frac{\sqrt{\boldsymbol{x}^2 + \boldsymbol{y}^2}}{\boldsymbol{d}}\right) \tag{5.5}$$

$$\boldsymbol{\phi} = \tan^{-1}\left(\frac{\boldsymbol{x}}{\boldsymbol{y}}\right) \tag{5.6}$$

$$\boldsymbol{R} = \sqrt{\boldsymbol{x}^2 + \boldsymbol{y}^2 + \boldsymbol{d}^2} \tag{5.7}$$

First, we define the observation plane location in which the far-field will be calculated. We used *d* = 70 mm. Where, d is the normal distance between the aperture and the observation plane as shown in Figure 5.4(a), (x,y) are the position of the detector, *R* is the slope distance between the centre of the aperture and the edge of the observation plane. Now, we solve the integration of the form-factor integration using Equation 5.4 as the following.

We suppose that $\tilde{E}_{\mathrm{a}}$ as a constant value of E_0 anywhere inside the aperture and zero outside, so we take it out of the integration:

$$\tilde{\boldsymbol{h}}(\boldsymbol{\theta},\boldsymbol{\phi}) = \boldsymbol{E_0} \iint_{-\infty}^{\infty} (\boldsymbol{x}_{\mathrm{a}},\boldsymbol{y}_{\mathrm{a}}) \,.\, \boldsymbol{e}^{[\mathrm{j}\boldsymbol{k}\sin\boldsymbol{\theta}(\boldsymbol{x}_{\mathrm{a}}\cos\boldsymbol{\phi}+\boldsymbol{y}_{\mathrm{a}}\sin\boldsymbol{\phi})]}\, \boldsymbol{dx}.\boldsymbol{dy} \tag{5.8}$$

Now, we change the integration boundaries by supposing a square aperture with side-lengths $(a_{\mathrm{x}}, a_{\mathrm{y}})$ points as shown in Figure 5.4(b) and expand the exponential equation in two terms based on the vertical and horizontal limits of the aperture as the following:

$$\tilde{\boldsymbol{h}}(\boldsymbol{\theta},\boldsymbol{\phi}) = \boldsymbol{E_o} \int_{\frac{-\boldsymbol{a_x}}{2}}^{\frac{\boldsymbol{a_x}}{2}} \boldsymbol{dx}_{\mathrm{a}}\, \boldsymbol{e}^{\mathrm{jk}(\sin\theta.\boldsymbol{x_a cos\phi})} \int_{\frac{-\boldsymbol{a_y}}{2}}^{\frac{\boldsymbol{a_y}}{2}} \boldsymbol{dy}_{\mathrm{a}}\, \boldsymbol{e}^{\mathrm{jk}(\sin\theta.\boldsymbol{y_a sin\phi})} \tag{5.9}$$

Now we put the integration of dy_a as *P* and solve it as the following:

$$\boldsymbol{P} = \int_{\frac{-\boldsymbol{a_y}}{2}}^{\frac{\boldsymbol{a_y}}{2}} \boldsymbol{dy}_{\mathrm{a}}\, \boldsymbol{e}^{\mathrm{jk}(\sin\theta.\boldsymbol{y_a sin\phi})} = \left[\frac{\boldsymbol{1}}{\boldsymbol{jk\, sin\theta\, sin\phi}}\, \boldsymbol{e}^{\mathrm{jk}(\sin\theta.\boldsymbol{y_a sin\phi})}\right]_{\frac{-\boldsymbol{a_y}}{2}}^{\frac{\boldsymbol{a_y}}{2}} \tag{5.10}$$

$$= \frac{1}{k\, sin\theta\, sin\phi}\left[\frac{e^{\mathrm{jk}\,\sin\theta.(\frac{a_y}{2}).sin\phi} - e^{\mathrm{jk}\,\sin\theta.(\frac{-a_y}{2}).sin\phi}}{j}\right]$$

To simplify the math, we put $u = k\sin\theta\sin\phi$ and multiplying the whole equation by $\frac{2}{2}$:

$$\boldsymbol{P = \frac{2}{u}\left[\frac{e^{\mathrm{ju}(\frac{a_y}{2})} - e^{\mathrm{ju}(\frac{-a_y}{2})}}{2j}\right] = \frac{2}{u}\sin\left(u\frac{a_y}{2}\right)} \quad (5.11)$$

Now, we substitute the *P* value back to equation 5.9 and solve the integration in terms of dx_a:

$$\boldsymbol{\tilde{h}(\theta,\phi) = E_o\int_{\frac{-a_x}{2}}^{\frac{a_x}{2}} dx_a\, e^{\mathrm{jk}(\sin\theta.x_a cos\phi)}.P = PE_o\int_{\frac{-a_x}{2}}^{\frac{a_x}{2}} dx_a\, e^{\mathrm{jk}(\sin\theta.x_a cos\phi)}} \quad (5.12)$$

$$\boldsymbol{\tilde{h}(\theta,\phi) = PE_o\frac{1}{jk\sin\theta\cos\phi}\left[e^{\mathrm{jk}(\sin\theta.x_a cos\phi)}\right]_{\frac{-a_x}{2}}^{\frac{a_x}{2}}} \quad (5.13)$$

To simplify the math, we put $v = k\sin\theta\cos\phi$ and multiply the equation by $\frac{2}{2}$:

$$\boldsymbol{\tilde{h}(\theta,\phi) = PE_o\frac{2}{v}\left[\frac{e^{\mathrm{jv}(\frac{a_x}{2})} - e^{\mathrm{jv}(\frac{-a_x}{2})}}{2j}\right] = PE_o\frac{2}{v}\sin\left(v\frac{a_x}{2}\right)} \quad (5.14)$$

Now, we put the *P* value again to obtain:

$$\boldsymbol{\tilde{h}(\theta,\phi) = \frac{2}{u}\sin\left(u\frac{a_y}{2}\right).E_o\frac{2}{v}\sin\left(v\frac{a_x}{2}\right)} \quad (5.15)$$

$$\boldsymbol{\therefore\ \tilde{h}(\theta,\phi) = \frac{4\tilde{E}_a}{uv}\sin\left(u\frac{a_y}{2}\right).\sin\left(v\frac{a_x}{2}\right)} \#(5.16)$$

The far-field pattern is found using:

$$\boldsymbol{\tilde{E}(R,\theta,\phi) = \frac{\mathrm{j}}{\lambda}\left(\frac{e^{-\mathrm{j}kR}}{R}\right)\tilde{h}(\theta,\phi)} \quad (5.17)$$

$$\boldsymbol{\therefore\ \tilde{E}(R,\theta,\phi) = \frac{\mathrm{j}}{\lambda}\left(\frac{e^{-\mathrm{j}kR}}{R}\right).\frac{4E_o}{uv}\sin\left(u\frac{a_y}{2}\right).\sin\left(v\frac{a_x}{2}\right)} \quad (5.18)$$

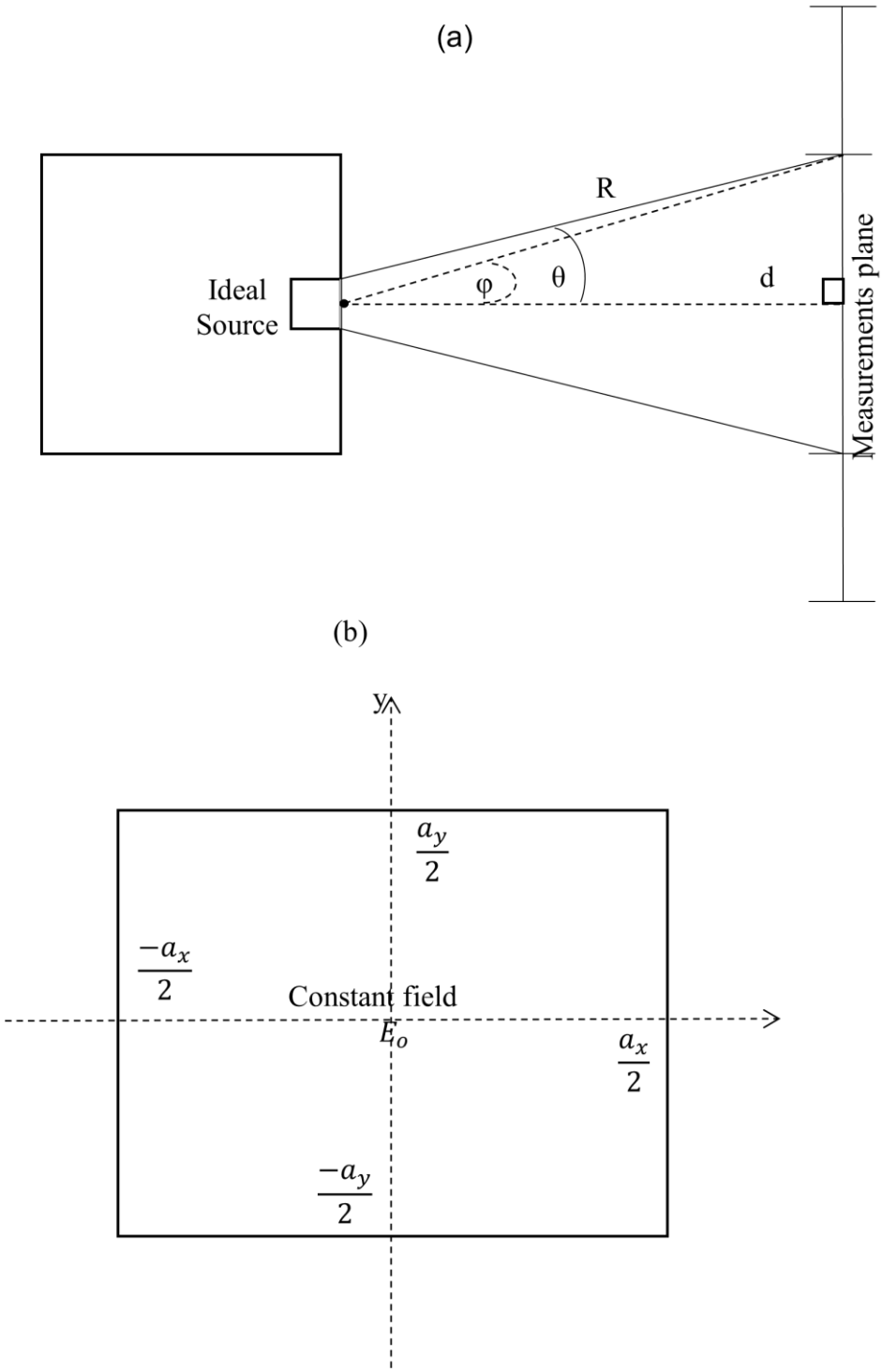

Figure 5.4 Schematic diagram of analytical feedhorn model (a) 2D illustration of the defined lengths and angles between the aperture and the observation plane. (b) Constant electric field across a square aperture with side-lengths $(\boldsymbol{a}_x, \boldsymbol{a}_y)$ points.

Based on equations 5.15 and 5.18, a MATLAB code has been written to obtain the form-factor and the electric near-field to far-field transformation. Now that we have calculated the far-field pattern for a single feedhorn as shown in Figure 5.5(a), a solution for a dual-feedhorn structure has been predicted using simple geometric transformations. Figure 5.5(b) shows an equivalent geometry for the simulation model. A second feedhorn has been added to the diagram, centred at a position (w, w). For the RAL waveguide

block, the feedhorns are at opposite sides of a cube with 15-mm sides, and a pair of reflectors are used to direct the beams forward. This gives an effective separation between the two apertures of 30 mm. The separation is then found using Pythagoras' theorem: $w = \frac{0.03}{\sqrt{2}}\ \mathrm{mm}$. We can also rotate this by 45°, so that the two feed-horns appear horizontally aligned in our results. To do this, we just need a 2D rotation, such that:

$$\boldsymbol{x'} = \frac{\boldsymbol{x} - \boldsymbol{y}}{\sqrt{\mathbf{2}}} \tag{5.19}$$

$$\boldsymbol{y'} = \frac{\boldsymbol{x} + \boldsymbol{y}}{\sqrt{\mathbf{2}}} \tag{5.20}$$

The electric fields of the two apertures can now be found using:

$$\boldsymbol{E_1}(\boldsymbol{x}, \boldsymbol{y}) = \boldsymbol{E}\left(\frac{\boldsymbol{x'} + \boldsymbol{w}}{\mathbf{2}}, \frac{\boldsymbol{y'} + \boldsymbol{w}}{\mathbf{2}}\right) \tag{5.21}$$

$$\boldsymbol{E_2}(\boldsymbol{x}, \boldsymbol{y}) = \boldsymbol{E}\left(\frac{\boldsymbol{x'} - \boldsymbol{w}}{\mathbf{2}}, \frac{\boldsymbol{y'} - \boldsymbol{w}}{\mathbf{2}}\right) \tag{5.22}$$

The far-field beam profile distribution has been obtained as shown in Figure 5.5 (c). The field for two diagonally oriented apertures is added coherently as both are excited by the same laser source. The simulated pattern shows both diffraction artefacts, and fine interference fringes. The principal diffraction effects are seen perpendicular to the aperture edges with a prominent central lobe within each aperture, in good agreement with the experimentally measured pattern. A beam divergence of 3.93° and a side-lobe ratio of -24 dB were computed.

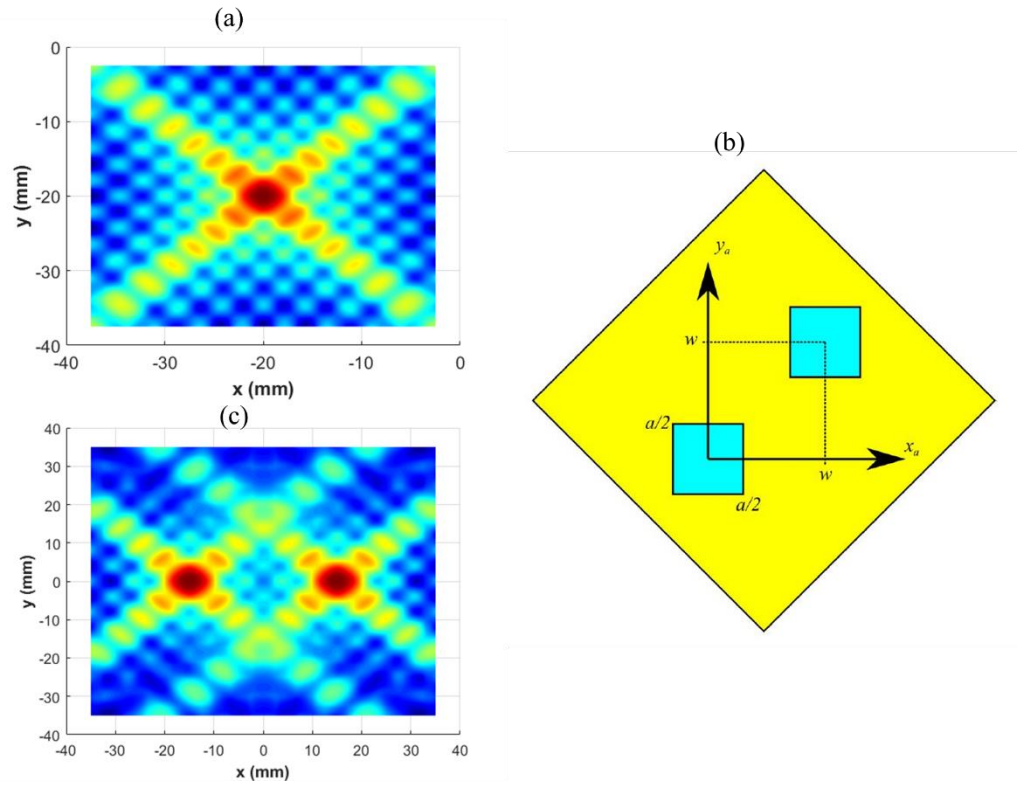

Figure 5.5 Simulated analytical far-field beam profiles at 70-mm screen distance (a) Simulated beam-profile for the emission from a single feedhorn. (b) Illustration of an equivalent dual-feedhorn structure. The two apertures (blue) have side-length and are separated by a distance accounting for the width of the block, and the position of the mirrors. They are arranged diagonally on the *x*–*y* axis to simplify the calculation. (c) Coherent far-field between the two apertures aligned diagonally with 30-mm effective separation.

Moving forward, instead of using a uniform electric field, we export the electromagnetic field at the end of the feedhorn from the HFSS by calculating the field at each point a in the *x*–*z* plane. Now we have the complex electric near field at the end of the aperture. Thus, the complex electric field, $\tilde{E}_{\mathrm{a}}$ across the antenna aperture (*i.e.*, the near-field excitation) is obtained from the HFSS simulation. This hybrid numerical/analytical modelling technique enables a rapid means of optimizing the coupling of THz radiation between the QCL and other system components.

5.3.4 Design analysis and results

As mentioned earlier in Section 5.1, the double-metal QCL provides very high beam divergence and poor far-field beam quality as a result of the sub-wavelength radiation confinement, a 3D simulation for the double-metal QCL has been done to have an overview on the beam-profile of the QCL and have a prediction of the divergence and radiated power as shown in Figure 5.6(a). One of the QCL facet has been excited as a waveport to analyse field across the QCL, the QCL beam profile has been observed with very high divergence at 49° as expected. Thus, the simulation moved forward to predict the performance of the QCL when integrated in the diagonal feedhorn structure. The excited field across the QCL propagates through the whole

design as shown in Figure 5.6(b). Figure 5.7(a and d) shows the simulated near-field and far-field (at 70-mm) beam patterns respectively for a single feedhorn. The simulation results for the experimentally fabricated feedhorn and integrated 3.3-THz QCL inside WM-130 rectangular waveguide, predict a 5.2° far-field divergence and 19.7-dB side-lobe suppression (*c.f.*, ~5.1–8.0° experimental value). Figure 5.7(c) shows the obvious difference between the unmounted and the integrated QCL in terms of beam divergence degree and total power intensity both at the same screen distance, which is 70-mm at the far-field area. Since an over-moded waveguide has been used as the feed for the horn, this yields a highly non-uniform near-field profile. However, the far-field pattern exhibits a well-defined central lobe, like that of an ideal feedhorn. This indicates that the beam pattern is only weakly dependent on the QCL waveguide. This has been investigated further by changing the dimensions of both the waveguide and the diagonal horn in the model.

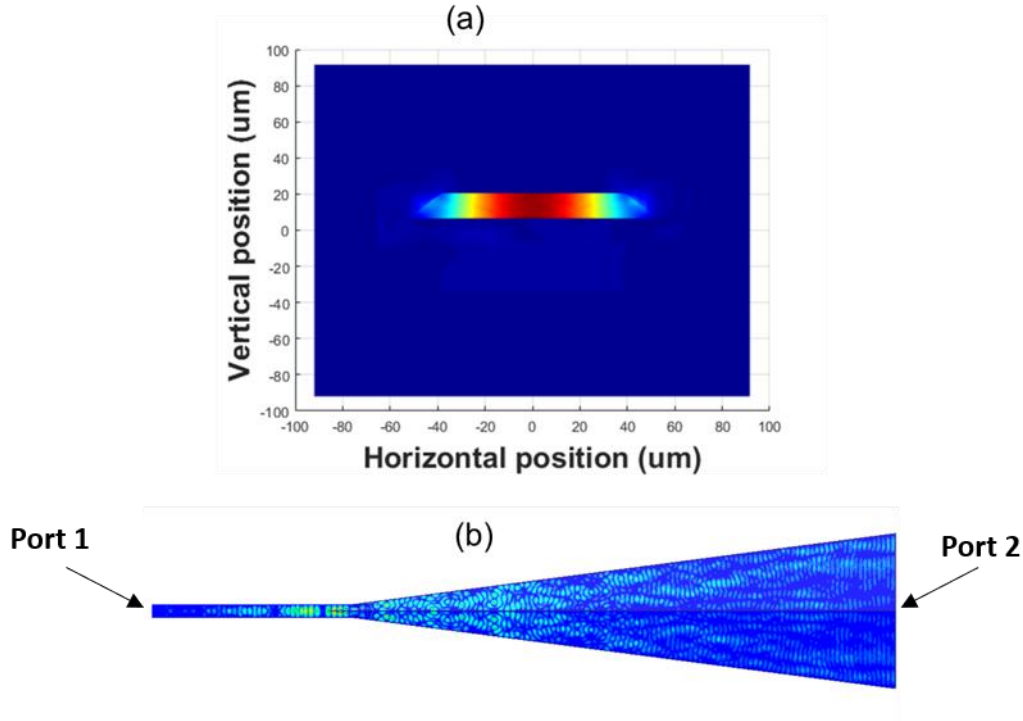

Figure 5.6 HFSS simulation of QCL mode within a waveguide (a) Au-based 3.3-THz DM-QCL beam-profile with waveport excitation from one of the QCL facet through a single feedhorn in the nearfield. (b) The propagation electromagnetic field through the whole design toward the aperture.

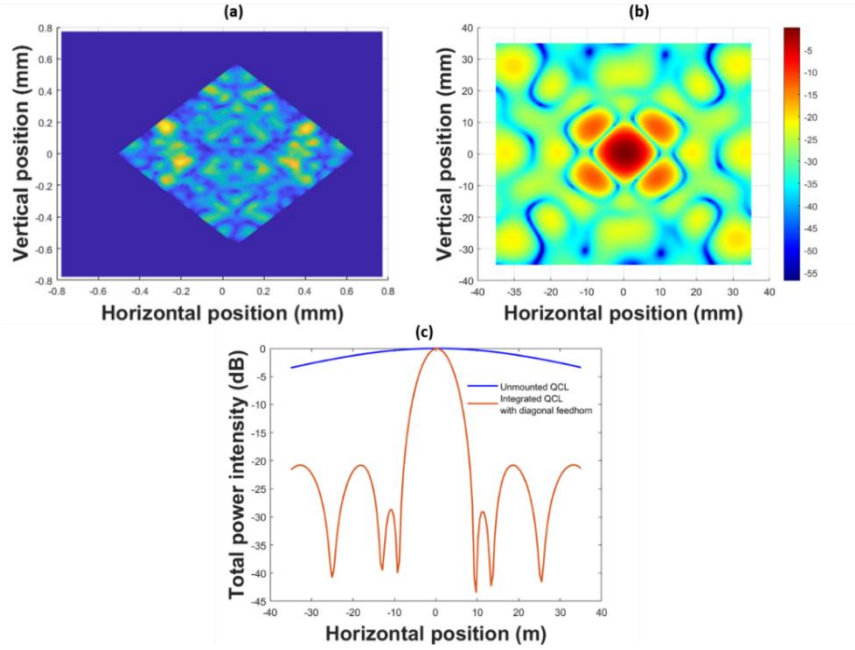

Figure 5.7 Simulated beam-profiles for QCL emission through a feedhorn (a) Simulated beam-profile for the emission from QCL facet through a single feedhorn in the nearfield, (b) simulated emission of the QCL facet beam-pattern obtained at 70 mm away from the Feedhorn aperture, (c) beam profile for the unmounted and the integrated QCL.

Table 5.2 The S_{21} power losses, Beam divergence, and side lobe ratio for a diagonal feedhorn with varying aperture size, fed by a WM-130 rectangular waveguide.

Aperture size (mm)	S_{21} (dB)	Divergence	Side-lobe ratio (dB)
0.389	15	16.2°	15.1
0.778	19	8.8°	16.7
1.167	19	6.2°	17.8
1.556	20	5.2°	19.7

Table 5.2 shows the beam-divergence angle and side-lobe ratio calculated for QCL radiation from one facet trough several feedhorn aperture sizes. Results are shown at the far-field region ($>2D^2/\lambda$) at 70-mm. Figure 5.8(a) shows an inverse-exponential relationship between the aperture size and the beam divergence, for feedhorns fed by a WM-130 waveguide, whereas Figure 5.8(b) shows that the divergence of a 1.556-mm feedhorn is only weakly dependent on the feed-waveguide dimensions. However, the optimum antenna aperture size for the beam divergence has the highest power loses with S_{21} -20 dB as shown in Figure 5.8(c), which has been calculated between the first port, which is the rear facet of the rectangular waveguide feed, and the second port at the feedhorn aperture to emerge all the power within the design. Also, an increase in aperture size leads to an increase in the side lobe ratio as shown in Figure 5.8(d).

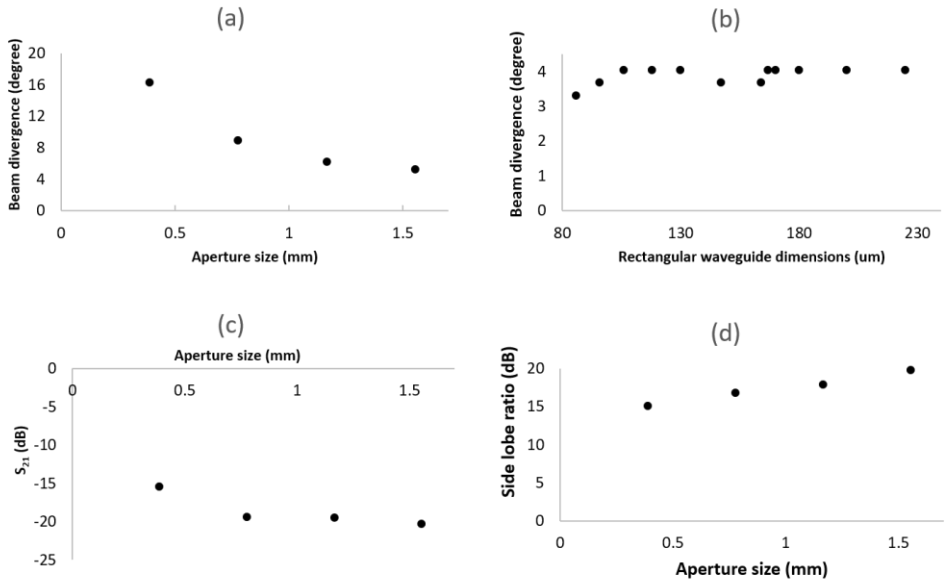

Figure 5.8 Beam divergence analysis for diagonal feedhorn (a) aperture size of a diagonal feedhorn fed by a WM-130 waveguide and (b) rectangular waveguide width, when feeding a 1.556-mm feedhorn. (c) Relationship between aperture size, which is the end of the horn, and the radiated power. (d) increasing in the Side lobe ratio with the larger apertures.

To obtain the maximum radiated power of the design, the position of the QCL inside the rectangular waveguide has been changed several times to see the effects of the QCL location on the beam divergence and the radiated power as shown in Figure 5.9. The results show that changing the position inside the rectangular waveguide away or close to the feedhorn affects the signal performance in terms of the radiated power, beam divergence, which are the minimum when the QCL is very close to the feedhorn (150 µm away from the feedhorn). These values are increasing when moving a little bit away from the feedhorn before starting to decrease again when the distance is about 1.15 mm as shown in Figure 5.9 (a and b). The side lobe ratio has also been obtained and has a minimum value at QCL distance about 450 µm away from the feed horn as shown in Figure 5.9(c).

Table 5.3 Radiated power, beam divergence, and side lobe ratio for a diagonal feedhorn with different QCL position inside the WM-130 rectangular waveguide.

QCL position away from the horn (mm)	**0.15**	**0.25**	**0.45**	**0.65**	**0.85**	**1.15**
S_{21} (dB)	22.9	20.3	20	20.4	20.6	20.9
Divergence (degree)	4.2	5.2	5.5	5.1	4.7	4.2
Side lobe ratio (dB)	22.1	19.7	19.4	19.8	20.3	22.1

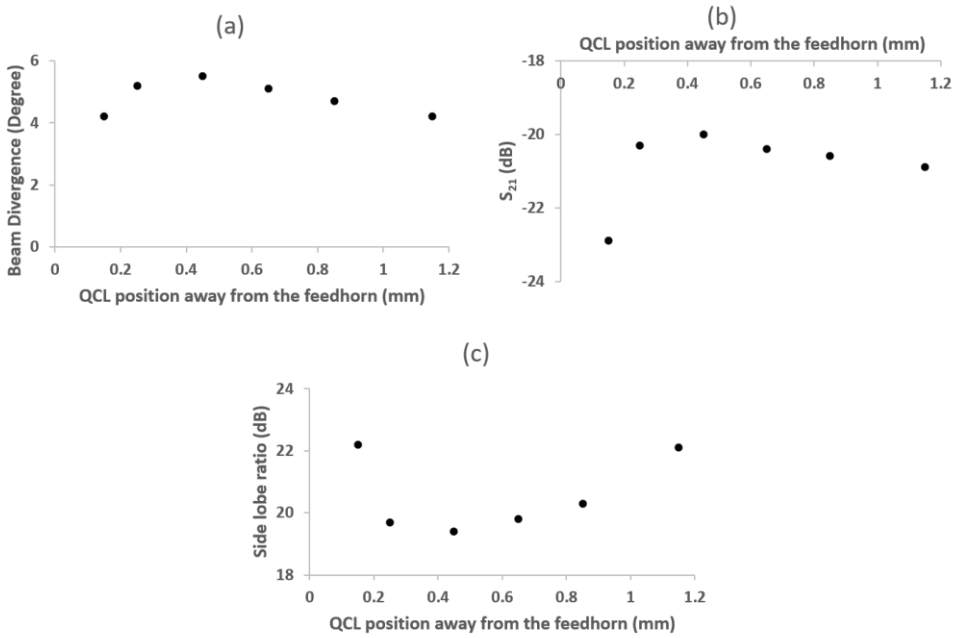

Figure 5.9 Integrated QCL signal performance based on its position inside the rectangular waveguide away from the feedhorn in terms of (a) beam divergence. (b) Radiated power. (c) Side lobe ratio.

With a view to make a complete comparison of all simulation settings, Figure 5.10 shows the relationship between beam divergence and aperture sizes for the analytical simulation, and hybrid modelling with and without QCL integration. The results show that the analytical simulation has the lowest beam divergence along all aperture sizes, and the maximum values has been obtained in the hybrid modelling with QCL integration. This means that the radiated QCL signal performance in terms of divergence and output power would be affected with a real experiment due to several factors such as the QCL operating temperature, antenna surface roughness and precision. Thus, the hybrid modelling with QCL integration is the best tool to be used to estimate how the real experimental result would be and hence can be used for further optimisation for the design.

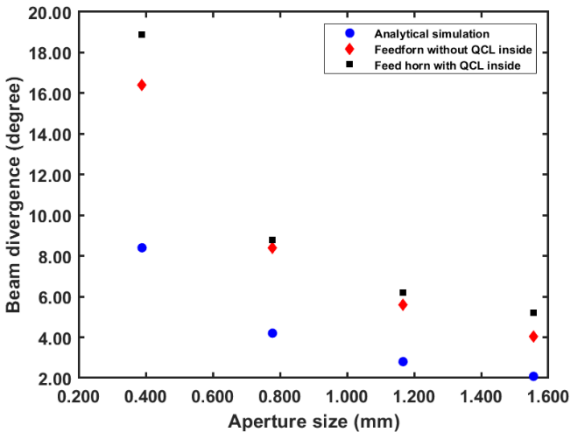

Figure 5.10 Relationship between the beam divergence and the aperture sizes for the analytical simulation without QCL, hybrid modelling with and without the QCL integration.

Therefore, the importance of this simulation lies in helping to find the most appropriate and efficient design, improve it and develop it through electromagnetic analysis of the design before the actual start of its manufacture, which will reduce the cost of the project and save time in manufacturing, and it will also help in finding the best position for the QCL within the design.

Accordingly, further measurements have been conducted in the University of Leeds by a PhD student Eleanor Nuttall to have a direct comparison between the simulation results and the experiment for a single-diagonal feedhorn with integrated QCL. The measurements were taken 30 mm, 55 mm and 70 mm away from the QCL aperture using an 800-µm pin hole coupled to a pyroelectric detector. The QCL was operated at a temperature of 10 K and a driving current of 208.4 mA. The pyroelectric detector was positioned at an angle to prevent reflections. The power was locked-in at a sensitivity of 1 mV. Each measurement was at a 2×2-mm step size except 70 mm which was at a 1×1-mm step size.

The results in Figure 5.11 show the formation of a dual lobe that becomes more defined the further into the far-field. What at first, we thought was reflection from the pyroelectric detector, we now believe to be two modes spatially separated. The experimental measurements below do not agree with simulations results produced previously. From the simulation data, the main power from the QCL is expected to be focused into a single lobe with two 45° planes of side lobe regions of weaker intensity. However, it was determined that the weaker side lobes would most likely not be detected using the pyroelectric detector. However, the beam divergence angle experimentally calculated agrees with the simulation calculation.

Moreover, measurements at 30 mm, 55 mm and 70 mm were repeated two more times and all show similar dual lobe behaviour with the pyro at a slight angle. When the pyro is at a very large angle, only one mode appears. This is determined to be because the pyroelectric detector is only ‘seeing’ one mode as the other mode is too far diverged to detect. Therefore, it was decided to keep the pyroelectric detector flat as these are additional modes from the laser and not reflections.

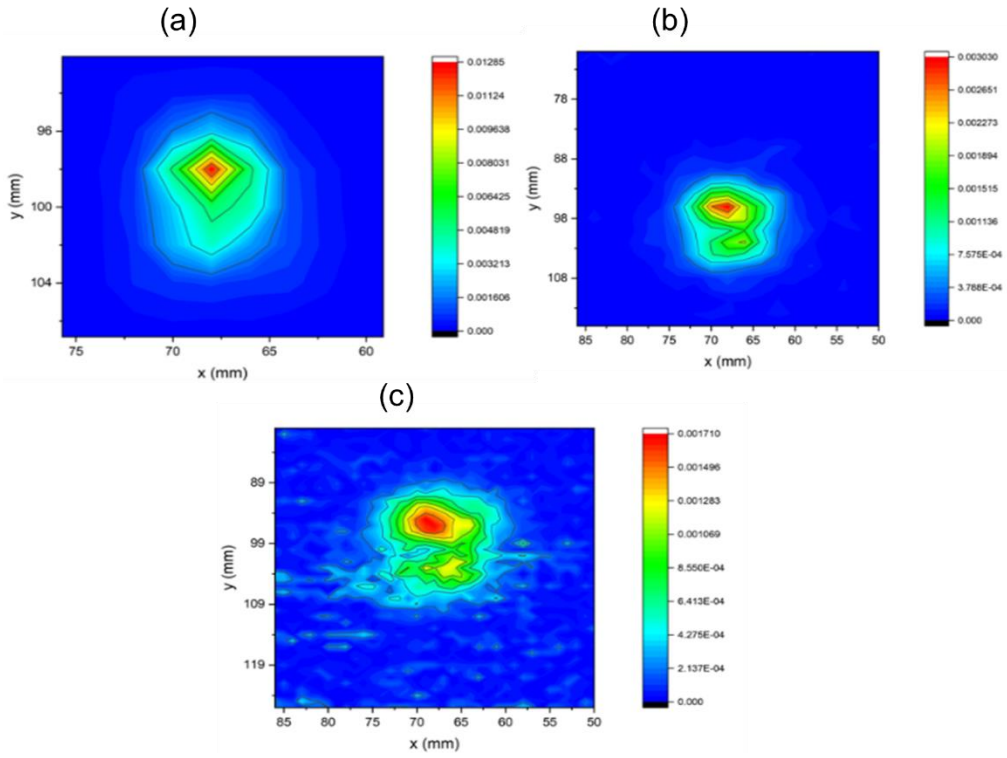

Figure 5.11 Experimental beam profile for a 3.5 THz with a 208.4 mA at: (a) 30-mm away from the cryostat window. (b) 55-mm distance. (c) 70-mm distance. Measurements were taken by Eleanor Nuttall.

Moving forward, The QCL was characterized at 10 K and a shows multi-mode correspond to the driving current as shown in Figure 5.12 and summarized in Table 5.4. Further measurements have been conducted to see the frequency dependent beam profiles of the collimated beam. The currents were 140 mA, 160 mA, 180 mA and 240 mA, these currents corresponded to different modes. Again, The QCL was operated at a temperature of 10 K.

However, no pinhole was used. The pyro was positioned straight and was not at an angle. The power was recorded at a sensitivity of 1 mV. The result appears on the upper lobe on 140 mA looks more intense, whilst it appears less intense on 160 mA. It appears that the lower lobe can be assigned to the 3.365-THz mode as it appears at all currents, (similarly to the heat map). The upper lobe can be assigned to the 3.428 THz mode as the intensity greatly increases with current.

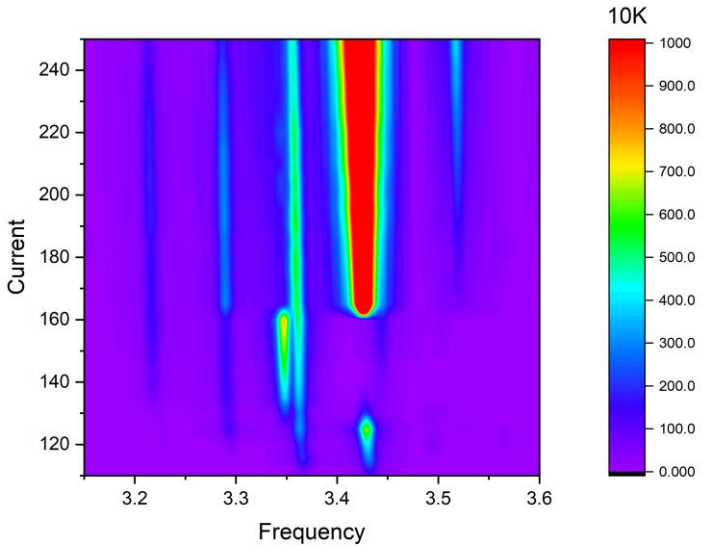

Figure 5.12 Multi-mode emission spectrum of QCL measured at different currents. Measurements were taken by Eleanor Nuttall at 10 K.

Table 5.4 Frequency range for multi-mode QCL at different currents with different intensities. The highlighted results show the maximum intensities of the detector output voltage (mV).

(Current) mA	Frequency [THz]/Intensity [a.u]				
140	3.221 (300.7)	3.294 (241.7)	**3.351 (2244)**	3.364 (927.5)	3.448 (113.1)
160	3.220 (346.7)	3.293 (565.6)	3.363 (827.4)	**3.429 (2844)**	3.497 (78.94)
180	3.219 (418.4)	3.292 (596.8)	3.362 (919.8)	**3.429 (3740)**	3.525 (201.70)
240	3.216 (319.7)	3.290 (388.9)	3.360 (989.2)	**3.426 (6338)**	3.522 (635.6)

To emphasize the frequency dependent beam profile, the measurements were obtained once again through the analytical model. Thus, the intensities and frequencies in Table 5.4 were used this time as the input parameters to the model, which will allow us to make a direct comparison between the simulation and the experiment. The aim from this were to calculate the power intensity at each frequency and hence calculate the total for the field power and compare this with what we obtained experimentally.

The beam divergence and the side lobe ratio have been observed at different screen distances with frequencies based on the experimental data range between 3.2 and 3.5 THz as shown in Figure 5.13. It seems that the beam divergence at higher frequency become less due to the short wavelength, but at 70-mm, which considered to be far-field distance, the beam divergence is almost the same. The side lobe ratio at all distance seems to be decreased if frequencies increase.

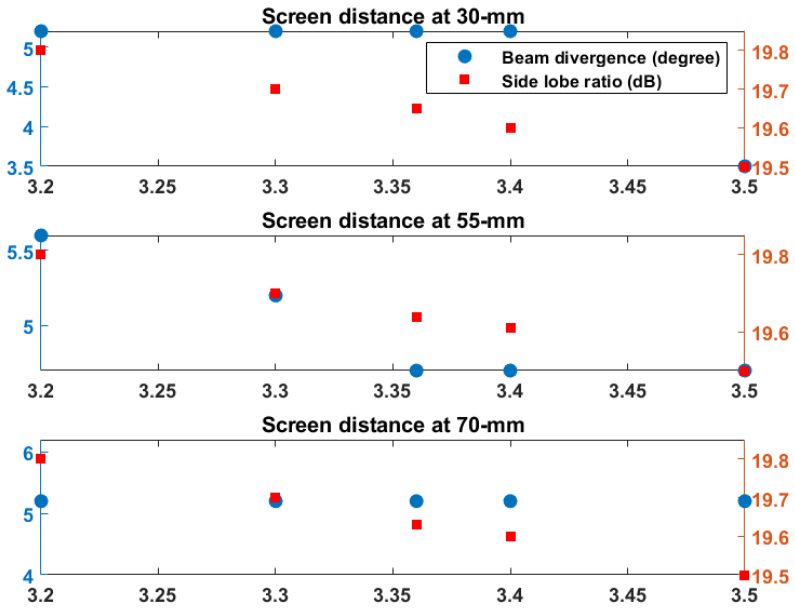

Figure 5.13 Simulated relationship between the frequency and the beam divergence at different screen distances.

The model that has been developed in this work to simulate the integration of the QCL within the waveguide and a dual diagonal feedhorn structure has been used to test the effectiveness of a diagonal feedhorn and demonstrates the QCL beam profile The resulting improvement in beam quality over the unmounted devices can be used as a starting point for other students to perform experimental check for various QCL devices within the dual feedhorn block, and proceed an initial alignment of an optical breadboard assembly that forms the basis of a future supra-THz space-borne atmospheric sounding payload. This would also support others to continue the research and development work in areas associated with precision mechanical integration, QCL semiconductor composition, and frequency stabilization techniques.

5.4 Summary

A new integration technique utilising both facets of a THz QCL simultaneously in a dual-feedhorn waveguide block has been demonstrated experimentally and analysed through an analytical simulation model. The experimental results exhibit a near-symmetrical diffraction pattern, as expected from the simulation, confirming that there is an equal power distribution between the two facets, and that each aperture is excited approximately uniformly by the QCL.

We have also presented a hybrid analytical/numerical electromagnetic model of a THz QCL coupled with a rectangular waveguide and a diagonal feedhorn, enabling rapid simulation of the impact of device geometry on the near- and far-field antenna patterns. The main purpose was to test the effectiveness of a diagonal feedhorn on the QCL beam profile when compared with unmounted devices. The calculated far-field divergence has been shown to depend only weakly on the geometry of the rectangular QCL waveguide and is therefore close to that of an ideal feedhorn, simplifying the optical

design of the receiver system. The divergence angle can be reduced by increasing the feedhorn aperture size, albeit at the expense of increased sidelobe content in the far-field pattern and obtained in the cost of giving up off some radiated power. All the simulation results have been obtained with the inclusion of an accurate electromagnetic model of the QCL itself, underpinning future waveguide-integration design of the receiver. Furthermore, to get the optimum integration of the QCL inside the rectangular waveguide, the QCL position has been located by changing the distance between the QCL radiated facet and the end of the horn several times. Although the beam divergence is not affected, the radiated power seems to be the lowest when placing the QCL near to the feedhorn, and it is increasing when moving far from it before it start fallen again. So, the optimum location has been obtained in place in which we got almost the peak of the radiated power. The results obtained represent a very substantial improvement in QCL output beam quality. This, in turn, demonstrates that a waveguide and diagonal feedhorn combination offers effictive method of propagating a supra-THz QCL output signal.

Chapter 6

Conclusions and future work

The main objective of the thesis was to produce desired performance and single mode emission from THz QCLs for satellite applications. To do that, we had to answer the question on what the requirement are needed to achieve a suitable THz QCL for satellite applications including, which needs different operational aspects including improvement on the operating temperatures, sufficient power. The other part of the thesis includes proposing a suitable waveguide design to produce an appropriate integration system in which the THz QCL will be integrated with other system components in a satellite mission.

Accordingly, to get the full understanding, the first two chapters were a general and fundamental reviews for the THz and laser technology. In Chapter 1, THz radiation and THz sensing technology have been introduced including a discussion about the various established THz sources, optical components, and detectors. After that, the two analytical methods of the THz spectroscopy system have been reviewed which are the frequency domain spectroscopy (FDS), and time domain spectroscopy (TDS). Then, because THz sensing technology has great importance in astronomy and atmospheric research, THz radiometry and its applications have been reviewed, along with highlights on a proposed satellite payload for Earth-observation. Following that, the project objectives and the structure of the thesis are discussed. Chapter 2 starts with an introductory to the laser technology and waveguide theory and designs, followed with a review on the quantum well heterostructure and the THz QCL. This would give full literature review of the developments of the THz-QCLs.

In Chapter 3, QCL fabrication have been explained, which includes THz SI-SP QCL and THz DM QCL. Investigating the performance of the QCL for each method gave us intelligible idea about the difference in performance between the two methods in terms of output power, operating temperature, and the frequency mode behaviour of the device along with the spectral resolution. This chapter gave a deep understanding on how to test the performance of the QCL, and what are the important factors that need to be observed to know whether the requirement of the proposed satellite mission have been achieved or not yet. The characterisation results for both SI-SP and DM QCL showed that when the device is been characterised in pulsed mode, more power can be observed, this is because the QCL is being turned on and off by a rate of 10 kHz from pulse generator and driving pulse of 2% duty cycle to the QCL. If the QCL work with 100% duty cycle, it means that it is operated in CW mode, in which there will be a self-heating coming from the active region will be added to the heat-sink temperature, which affect the operating temperature and the output power of the device. From that, results showed that the output power has an inverse relationship with heat sink temperature. For SI-SP QCL compared with DM QCL, The THz SI-SP QCL

results showed that it provides more power and multi-mode behaviour with wide range tunability around 200 GHz, while the 4.7-THz DM QCL emits lower power at few milliwatts, but higher resolution spectra and single mode behaviour, which makes the last more convenient for use as an LO for the proposed satellite mission.

Chapter 4 discussed optimisation methods that aims to improve the performance of the THz QCLs in terms of operating temperature and output power, by applying high reflectivity (HR) optical coatings to reduce the self-heating temperature and reduce the power dissipation of the device. This not only would improve the temperature performance of the device, but also would make it possible to reduce the cavity length to a smaller size and reduce the power consumption, which is desirable for the integration of the QCL for the proposed satellite payloads. Due to the long wavelength of the THz QCLs, metal-on-insulator coatings, either based on Al_2O_3/Ti/Au or the one that has been used in this thesis SiO_2/Au, that would provide about 99% reflectivity. The study that has been reviewed used such technique on a SI-SP QCL showed an increase emitted power in which they achieved a peak power ~1.01 W (at 10 K) by coating the rear face with a recipe based on SiO_2/Au. Based on that, the same technique has been used on a fabricated DM-QCL to investigate if the HR coating would have similar effect. The maximum power of the device that has been obtained from the coated device showed an increase in the output power by 8% compared with the uncoated device. However, this increase in power came at the cost of decreasing the maximum operating temperature of the device, which is for the uncoated device worked up to 80 K with 141 µW, while for HR coated device 18 µW at the same temperature. However, this change in power could be related to the change in thermal resistances of the two devices and therefore their active region temperatures. Therefore, further systematic study is needed to endorse these results study and to eliminate variation in thermal resistance between different fabrication runs.

Previous characteristic results that have been discussed confirm the suitability of the DM-QCL and its preference over the SI-SP QCL for the proposed satellite payload. Thus, changing the type of cladding metal surrounding the active region from the top and bottom has been investigated, by using silver as an alternative to gold due to its efficient electrical conductivity. Previous studies show that using the silver would increase the output power of the QCL by 40% and improve the maximum operating temperature by 5 K. Not only that, but also lower threshold current density compared with the Au-based one. Another study shows that the use of Ag-based QCL would reduce the losses by 2–4 cm^{-1} and 10-K higher operating temperature. Thus, Ag-based DM QCL has been fabricated and characterised. Compared with an identical Au-based device, the results agreed with what have been highlighted on the studies and show that the Ag-based device work up to 145 K, which is 5 K lasing temperature more than the Au-based one. It is also show 11.25% increase on the output power. However,

it is important to note that difficulty on the detector alignment with the THz QCL inside the cryostat makes it difficult to have a direct power comparison. Thus, threshold current density is a better measure factor for the improvement on the performance. The threshold current density of the Ag-based device is 40% less than the Au-based device at 10 K and 30% less at 60 K, which means that Ag-based waveguides exhibit lower losses than Au-based waveguides.

In Chapter 5, an integration technique for the QCL inside a proposed design that would improve the beam divergence and the far-field pattern of the device have been investigated by presenting a multi-scale electromagnetic model of a THz QCL coupled with a rectangular waveguide and a diagonal feedhorn, enabling rapid simulation of the impact of device geometry on the antenna patterns. In addition, utilising both facets of a THz QCL simultaneously in a dual-feedhorn waveguide block would enable access to radiation emitted from both facets of the QCL simultaneously, which opens the way towards simultaneous integration of the QCL with a frequency stabilisation system and a supra-THz mixer. Accordingly, the far-field beam profile distribution has been obtained from the analytical simulation shows a beam divergence of 3.93-degrees and a side-lobe ratio of -24 dB, in good agreement with the experimentally measured pattern from RAL, in which fine interference fringes and diffraction artefacts is obtained from the pattern and central lobe within each aperture.

After that, the simulation was further developed by using the HFSS, which is a 3D design program that simulates electromagnetic radiation to obtain more accurate results. previous studies show that unmounted double-metal QCL provides very high beam divergence and poor far-field beam quality because of the sub-wavelength radiation confinement. Accordingly, a 3D simulation was made to have a prediction of the divergence and radiated power for the unmounted devices. The obtained results show very high divergence at 49°, which in turn led to low radiated power which predicted to be 960 µW. these results compared with what was obtain from the analytical simulation is very high, meaning that the feedhorn design would improve the divergence and hence improve the power. Thus, the diagonal feedhorn structure has been designed with QCL integrated in it to simulate and predict the performance of the QCL for the design. The results show a prediction of a 5.2° far-field divergence and 19.7-dB side-lobe suppression compared with ~5.1–8.0° experimental value. Obviously, the beam divergence degree and total power intensity from the integrated QCL is much better than the unmounted one, in which the far-field pattern exhibits a well-defined central lobe, like that of an ideal feedhorn. Further analysis for the design has been made by changing the dimensions of both the waveguide and the diagonal horn in the model, the results indicate that the beam pattern is only weakly dependent on the QCL waveguide. Moreover, a PhD student Eleanor Nuttall from the same team at the University of Leeds have done further measurements for a single-diagonal feedhorn with integrated QCL, in which she obtained a dual lobe that becomes more defined the further into the far-

field, and the characterized QCL shows multi-mode correspond to the deriving current. These results suggest that the beam divergence is frequency dependent. Thus, the measurements were obtained once again through the analytical model to emphasize the frequency dependent beam profile. Results show that beam divergence at higher frequency become less due to the short wavelength.

6.1 Future work

The performance of the double-metal QCL devices can be investigated by changing the method of the fabrication, using dry etching to form the laser ridges might improve the laser width and length precision and hence more precise results. Thus, a systematic study based on a comparison between the dry etching process against the wet chemical etching with different lengths and widths would give us the answer whether a further optimisation can be applied on the double metal QCL using such technique or not. In addition, the number of the QCL devices that have been optimised and investigated in this study is limited due to the lack in in the provided materials and the limitation to access the lab during the pandemic of COVID-19, so fabricating more devices and optimise them using the same techniques which include the HR coating and Ag-based waveguide would help to understand whether is it possible to ensure the reproducibility of the devices with the same performance, this also would help to verify the results presented in this study and make them publishable.

The waveguide design that has been analysed in this study to integrate the QCL and improve the quality of the beam profile can have more work by proposing a complete design to couple the radiation from the QCL to the mixer. Simulating such design using HFSS would help to optimise the dimensions of the waveguide, and the position of the QCL and the mixer inside the waveguide and proposing a solution to couple the radiation coming out from the QCL that has vertical polarity with the horizontal polarisation of the mixer. Further simulation work can be made on the distribution of the optics for the proposed satellite mission that would detect the signals coming out from the space and direct it to heterodyne receiver for signal processing. doing such simulation would help to have the optimum optics locations and angles to make sure best detection for the incoming signal. In addition, a thermal simulation for all the components included in the proposed satellite payload would help to get the best distribution for the system equipment’s.

References

[1] A. Y. Pawar, D. D. Sonawane, K. B. Erande, and D. V. Derle, “Terahertz technology and its applications,” *Drug Invent. Today*, vol. 5, no. 2, pp. 157–163, Jun. 2013, doi: 10.1016/j.dit.2013.03.009.

[2] S. Kumar, “Recent progress in terahertz quantum cascade lasers,” *IEEE J. Sel. Top. Quantum Electron.*, vol. 17, no. 1, pp. 38–47, Jan. 2011, doi: 10.1109/JSTQE.2010.2049735.

[3] Y. He, Y. Chen, L. Zhang, S.-W. Wong, and Z. N. Chen, “An overview of terahertz antennas,” *China Commun.*, vol. 17, no. 7, pp. 124–165, Jul. 2020, doi: 10.23919/J.CC.2020.07.011.

[4] J. Grade, P. Haydon, and D. van der Weide, “Electronic Terahertz Antennas and Probes for Spectroscopic Detection and Diagnostics,” *Proc. IEEE*, vol. 95, no. 8, pp. 1583–1591, Aug. 2007, doi: 10.1109/JPROC.2007.898900.

[5] H. Tabata, “Application of Terahertz Wave Technology in the Biomedical Field,” *IEEE Trans. Terahertz Sci. Technol.*, vol. 5, no. 6, pp. 1146–1153, Nov. 2015.

[6] D. R. Bacon, “Time-Resolved Pump-Probe Investigation of the Terahertz Quantum Cascade Laser,” p. 194.

[7] A. G. Davies, E. H. Linfield, and M. B. Johnston, “The development of terahertz sources and their applications,” *Phys. Med. Biol.*, vol. 47, no. 21, p. 3679, 2002.

[8] D. H. Auston, “Picosecond optoelectronic switching and gating in silicon,” *Appl. Phys. Lett.*, vol. 26, no. 3, pp. 101–103, Feb. 1975, doi: 10.1063/1.88079.

[9] M. Tani *et al.*, “Photoconductive Emission and Detection of Terahertz Pulsed Radiation Using Semiconductors and Semiconductor Devices,” *J. Infrared Millim. Terahertz Waves*, vol. 33, no. 4, pp. 393–404, Apr. 2012, doi: 10.1007/s10762-012-9882-1.

[10] P. U. Jepsen, R. H. Jacobsen, and S. R. Keiding, “Generation and detection of terahertz pulses from biased semiconductor antennas,” *JOSA B*, vol. 13, no. 11, pp. 2424–2436, 1996.

[11] S. S. Dhillon *et al.*, “The 2017 terahertz science and technology roadmap,” *J. Phys. Appl. Phys.*, vol. 50, no. 4, p. 043001, Feb. 2017, doi: 10.1088/1361-6463/50/4/043001.

[12] R. A. Lewis, “A review of terahertz sources,” *J. Phys. Appl. Phys.*, vol. 47, no. 37, p. 374001, Sep. 2014, doi: 10.1088/0022-3727/47/37/374001.

[13] A. Rostami, H. Rasooli, and H. Baghban, *Terahertz Technology: Fundamentals and Applications*. Springer Science & Business Media, 2010.

[14] “Field Guide to Terahertz Sources, Detectors, and Optics | (2012) | O’Sullivan | Publications | Spie.” https://spie.org/publications/book/952851?SSO=1 (accessed Feb. 20, 2018).

[15] B. Ferguson and X.-C. Zhang, “Materials for terahertz science and technology,” *Nat. Mater.*, vol. 1, no. 1, pp. 26–33, 2002.

[16] M. Tonouchi, “Cutting-edge terahertz technology,” *Nat. Photonics*, vol. 1, pp. 97–105, Feb. 2007, doi: 10.1038/nphoton.2007.3.

[17] A. Maestrini *et al.*, “A 540-640-GHz high-efficiency four-anode frequency tripler,” *IEEE Trans. Microw. Theory Tech.*, vol. 53, no. 9, pp. 2835–2843, Sep. 2005, doi: 10.1109/TMTT.2005.854174.

[18] A. Maestrini *et al.*, “A Frequency-Multiplied Source With More Than 1 mW of Power Across the 840–900-GHz Band,” *IEEE Trans. Microw. Theory Tech.*, vol. 58, no. 7, pp. 1925–1932, Jul. 2010, doi: 10.1109/TMTT.2010.2050171.

[19] J. V. Siles and J. Grajal, “Physics-Based Design and Optimization of Schottky Diode Frequency Multipliers for Terahertz Applications,” *IEEE Trans. Microw. Theory Tech.*, vol. 58, no. 7, pp. 1933–1942, Jul. 2010, doi: 10.1109/TMTT.2010.2050103.

[20] L.-A. Yang, Y. Hao, Q. Yao, and J. Zhang, “Improved Negative Differential Mobility Model of GaN and AlGaN for a Terahertz Gunn Diode,” *IEEE Trans. Electron Devices*, vol. 58, no. 4, pp. 1076–1083, Apr. 2011, doi: 10.1109/TED.2011.2105269.

[21] L. Li *et al.*, “Threading dislocation reduction in transit region of GaN terahertz Gunn diodes,” *Appl. Phys. Lett.*, vol. 100, no. 7, p. 072104, Feb. 2012, doi: 10.1063/1.3685468.

[22] L. Yang, S. Long, X. Guo, and Y. Hao, “A comparative investigation on sub-micrometer InN and GaN Gunn diodes working at terahertz frequency,” *J. Appl. Phys.*, vol. 111, no. 10, p. 104514, May 2012, doi: 10.1063/1.4721667.

[23] S. Pérez, T. González, D. Pardo, and J. Mateos, “Terahertz Gunn-like oscillations in InGaAs/InAlAs planar diodes,” *J. Appl. Phys.*, vol. 103, no. 9, p. 094516, May 2008, doi: 10.1063/1.2917246.

[24] W. Knap *et al.*, “Terahertz emission by plasma waves in 60 nm gate high electron mobility transistors,” *Appl. Phys. Lett.*, vol. 84, no. 13, pp. 2331–2333, Mar. 2004, doi: 10.1063/1.1689401.

[25] N. Dyakonova *et al.*, “Room-temperature terahertz emission from nanometer field-effect transistors,” *Appl. Phys. Lett.*, vol. 88, no. 14, p. 141906, Apr. 2006, doi: 10.1063/1.2191421.

[26] J. Lusakowski *et al.*, “Voltage tuneable terahertz emission from a ballistic nanometer InGaAs/InAlAs transistor,” *J. Appl. Phys.*, vol. 97, no. 6, p. 064307, Mar. 2005, doi: 10.1063/1.1861140.

[27] M. S. Shur and Jian-Qiang Lu, “Terahertz sources and detectors using two-dimensional electronic fluid in high electron-mobility transistors,” *IEEE Trans. Microw. Theory Tech.*, vol. 48, no. 4, pp. 750–756, Apr. 2000, doi: 10.1109/22.841969.

[28] A. El Fatimy *et al.*, “AlGaN/GaN high electron mobility transistors as a voltage-tunable room temperature terahertz sources,” *J. Appl. Phys.*, vol. 107, no. 2, p. 024504, Jan. 2010, doi: 10.1063/1.3291101.

[29] S. Preu, G. H. Döhler, S. Malzer, L. J. Wang, and A. C. Gossard, “Tunable, continuous-wave Terahertz photomixer sources and applications,” *J. Appl. Phys.*, vol. 109, no. 6, p. 061301, Mar. 2011, doi: 10.1063/1.3552291.

[30] D. J. Ironside, R. Salas, P.-Y. Chen, K. Q. Le, A. Alú, and S. R. Bank, “Enhancing THz generation in photomixers using a metamaterial approach,” *Opt. Express*, vol. 27, no. 7, p. 9481, Apr. 2019, doi: 10.1364/OE.27.009481.

[31] P. H. Siegel, “Terahertz technology,” *IEEE Trans. Microw. Theory Tech.*, vol. 50, no. 3, pp. 910–928, 2002.

[32] M. Razeghi, “Semiconductor Lasers,” in *Technology of Quantum Devices*, Springer US, 2010, pp. 209–270.

[33] J. Faist, F. Capasso, D. L. Sivco, C. Sirtori, A. L. Hutchinson, and A. Y. Cho, “Quantum Cascade Laser,” *Science*, vol. 264, no. 5158, pp. 553–556, Apr. 1994, doi: 10.1126/science.264.5158.553.

[34] R. Köhler *et al.*, “Terahertz semiconductor-heterostructure laser,” *Nature*, vol. 417, no. 6885, Art. no. 6885, May 2002, doi: 10.1038/417156a.

[35] H. B. Ye, Y. H. Zhang, and W. Z. Shen, “Carrier transport and optical properties in GaAs far-infrared/terahertz mirror structures,” *Thin Solid Films*, vol. 514, no. 1, pp. 310–315, Aug. 2006, doi: 10.1016/j.tsf.2006.03.009.

[36] N. Krumbholz *et al.*, “Omnidirectional terahertz mirrors: A key element for future terahertz communication systems,” *Appl. Phys. Lett.*, vol. 88, no. 20, p. 202905, May 2006, doi: 10.1063/1.2205727.

[37] H. D. Hristov, J. M. Rodriguez, and W. Grote, “The grooved-dielectric Fresnel zone plate: An effective terahertz lens and antenna,” *Microw. Opt. Technol. Lett.*, vol. 54, no. 6, pp. 1343–1348, 2012, doi: 10.1002/mop.26812.

[38] X.-Y. Jiang *et al.*, “An ultrathin terahertz lens with axial long focal depth based on metasurfaces,” *Opt. Express*, vol. 21, no. 24, pp. 30030–30038, Dec. 2013, doi: 10.1364/OE.21.030030.

[39] B. Scherger, C. Jördens, and M. Koch, “Variable-focus terahertz lens,” *Opt. Express*, vol. 19, no. 5, pp. 4528–4535, Feb. 2011, doi: 10.1364/OE.19.004528.

[40] R. A. Lewis, “A review of terahertz detectors,” *J. Phys. Appl. Phys.*, vol. 52, no. 43, p. 433001, Aug. 2019, doi: 10.1088/1361-6463/ab31d5.

[41] F. Alves, D. Grbovic, B. Kearney, and G. Karunasiri, “Microelectromechanical systems bimaterial terahertz sensor with integrated metamaterial absorber,” *Opt. Lett.*, vol. 37, no. 11, pp. 1886–1888, Jun. 2012, doi: 10.1364/OL.37.001886.

[42] B. T. Kearney, F. Alves, D. Grbovic, and G. Karunasiri, “Al/SiOx/Al single and multiband metamaterial absorbers for terahertz sensor applications,” *Opt. Eng.*, vol. 52, no. 1, p. 013801, Jan. 2013, doi: 10.1117/1.OE.52.1.013801.

[43] F. Alves, D. Grbovic, B. Kearney, N. V. Lavrik, and G. Karunasiri, “Bi-material terahertz sensors using metamaterial structures,” *Opt. Express*, vol. 21, no. 11, pp. 13256–13271, Jun. 2013, doi: 10.1364/OE.21.013256.

[44] A. D. Rakić *et al.*, “Sensing and imaging using laser feedback interferometry with quantum cascade lasers,” *Appl. Phys. Rev.*, vol. 6, no. 2, p. 021320, Jun. 2019, doi: 10.1063/1.5094674.

[45] H.-W. Hübers, R. Eichholz, S. G. Pavlov, and H. Richter, “High Resolution Terahertz Spectroscopy with Quantum Cascade Lasers,” *J. Infrared Millim. Terahertz Waves*, vol. 34, no. 5–6, pp. 325–341, Apr. 2013, doi: 10.1007/s10762-013-9973-7.

[46] M. Tani, Zhiping Jiang, and X.-C. Zhang, “Photoconductive terahertz transceiver,” *Electron. Lett.*, vol. 36, no. 9, pp. 804–805, Apr. 2000, doi: 10.1049/el:20000611.

[47] Q. Chen, Z. Jiang, M. Tani, and X.-C. Zhang, “Electro-optic terahertz transceiver,” *Electron. Lett.*, vol. 36, no. 15, pp. 1298–1299, Jul. 2000, doi: 10.1049/el:20000945.
[48] C. Jördens *et al.*, “Fibre-coupled terahertz transceiver head,” *Electron. Lett.*, vol. 44, no. 25, pp. 1473–1475, Dec. 2008.
[49] S. Busch, T. Probst, M. Schwerdtfeger, R. Dietz, J. Palací, and M. Koch, “Terahertz transceiver concept,” *Opt. Express*, vol. 22, no. 14, pp. 16841–16846, Jul. 2014, doi: 10.1364/OE.22.016841.
[50] W. Withayachumnankul and M. Naftaly, “Fundamentals of Measurement in Terahertz Time-Domain Spectroscopy,” *J. Infrared Millim. Terahertz Waves*, vol. 35, no. 8, pp. 610–637, Aug. 2014, doi: 10.1007/s10762-013-0042-z.
[51] P. Y. Han, M. Tani, M. Usami, S. Kono, R. Kersting, and X.-C. Zhang, “A direct comparison between terahertz time-domain spectroscopy and far-infrared Fourier transform spectroscopy,” *J. Appl. Phys.*, vol. 89, no. 4, pp. 2357–2359, Feb. 2001, doi: 10.1063/1.1343522.
[52] H.-W. Hubers, “Terahertz Heterodyne Receivers,” *IEEE J. Sel. Top. Quantum Electron.*, vol. 14, no. 2, pp. 378–391, 2008, doi: 10.1109/JSTQE.2007.913964.
[53] A. Valavanis *et al.*, “Feedhorn-integrated THz QCL local oscillators for the LOCUS atmospheric sounder,” Copenhagen, Denmark, Sep. 2016, pp. 1–2, doi: 10.1109/IRMMW-THz.2016.7758687.
[54] “WMAP Observatory: Mission Overview.” https://map.gsfc.nasa.gov/mission/observatory.html (accessed Sep. 14, 2020).
[55] “ESA Science & Technology - Herschel.” https://sci.esa.int/web/herschel/ (accessed Sep. 14, 2020).
[56] “ESA Science & Technology - Planck.” https://sci.esa.int/web/planck/ (accessed Sep. 14, 2020).
[57] V. M. Pillet, A. Aparicio, and F. Sánchez, *Payload and Mission Definition in Space Sciences*. Cambridge University Press, 2005.
[58] M. A. Janssen *et al.*, “MWR: Microwave Radiometer for the Juno Mission to Jupiter,” *Space Sci. Rev.*, vol. 213, no. 1, pp. 139–185, Nov. 2017, doi: 10.1007/s11214-017-0349-5.
[59] “ESA Science & Technology - Orbiter Instruments.” https://sci.esa.int/web/rosetta/-/35061-instruments (accessed Sep. 17, 2020).
[60] S. P. Rea *et al.*, “The Low-Cost Upper-Atmosphere Sounder (LOCUS),” *26th International Symposium on Space Terahertz Technology*, Jul. 15, 2015. https://www.cfa.harvard.edu/events/2015/isstt2015/proceedings/files/ISSTT2015_M1-3_Gerber_Abstract.pdf (accessed Apr. 28, 2017).
[61] “ESA Science & Technology - JUICE.” https://sci.esa.int/web/juice (accessed Sep. 17, 2020).
[62] “Metop — EUMETSAT.” https://www.eumetsat.int/website/home/Satellites/CurrentSatellites/Metop/index.html (accessed Sep. 17, 2020).
[63] “LOCUS Satellite,” *LOCUS Satellite*. http://www.locussatellite.com/ (accessed Sep. 11, 2017).

[64] H. Zell, “Graphic of the Upper Atmosphere,” *NASA*, Mar. 02, 2015. http://www.nasa.gov/mission_pages/sunearth/science/upper-atmosphere-graphic.html (accessed Sep. 13, 2017).

[65] G. Savini *et al.*, “Recent progress in the Elegant Breadboard supra-THz activities for LOCUS and a view to an astronomy application,” in *Millimetre Waves and Terahertz Technologies (UCMMT), 2016 IEEE 9th UK-Europe-China Workshop on*, 2016, pp. 1–5, Accessed: Sep. 15, 2017. [Online]. Available: http://ieeexplore.ieee.org/abstract/document/7873956/.

[66] J. W. Waters *et al.*, “The Earth observing system microwave limb sounder (EOS MLS) on the aura Satellite,” *IEEE Trans. Geosci. Remote Sens.*, vol. 44, no. 5, pp. 1075–1092, May 2006, doi: 10.1109/TGRS.2006.873771.

[67] H. Richter *et al.*, “THz quantum-cascade laser as a local oscillator for SOFIA,” in *2011 International Conference on Infrared, Millimeter, and Terahertz Waves*, Oct. 2011, pp. 1–2, doi: 10.1109/irmmw-THz.2011.6104814.

[68] L. Proudfit, “SOFIA Overview,” *NASA*, Apr. 21, 2015. http://www.nasa.gov/mission_pages/SOFIA/overview/index.html (accessed Nov. 20, 2020).

[69] H.-W. Hübers, H. Richter, and M. Wienold, “High-resolution terahertz spectroscopy with quantum-cascade lasers,” *J. Appl. Phys.*, vol. 125, no. 15, p. 151401, Apr. 2019, doi: 10.1063/1.5084105.

[70] “Wiley-IEEE Press: Introduction to Laser Technology, 4th Edition - C. Breck Hitz, James J. Ewing, Jeff Hecht.” http://www.wiley.com/WileyCDA/WileyTitle/productCd-0470916206,miniSiteCd-IEEE2.html (accessed Apr. 12, 2020).

[71] S. O. Kasap, *Principles of electronic materials and devices*. Tata McGraw-Hill, 2006. 978-1-107-39346-2

[72] “Quantum Wells, Wires and Dots: Theoretical and Computational Physics of Semiconductor Nanostructures, 4th Edition | Wiley,” *Wiley.com*. https://www.wiley.com/en-us/Quantum+Wells%2C+Wires+and+Dots%3A+Theoretical+and+Computational+Physics+of+Semiconductor+Nanostructures%2C+4th+Edition-p-9781118923368 (accessed Apr. 14, 2020).

[73] B. S. Williams, “Terahertz quantum-cascade lasers,” *Nat. Photonics*, vol. 1, pp. 517–525, Sep. 2007, doi: 10.1038/nphoton.2007.166.

[74] S. K. Selvaraja and P. Sethi, “Review on Optical Waveguides,” in *Emerging Waveguide Technology*, K. Y. You, Ed. InTech, 2018.978-1-78923-493-0

[75] C. Sirtori, C. Gmachl, F. Capasso, A. L. Hutchinson, and A. Y. Cho, “Long-wavelength (l ο 8–11.5 mm) semiconductor lasers with waveguides based on surface plasmons,” p. 3.

[76] Tredicucci A, Gmachl C, Capasso F, Hutchinson AL, Sivco DL, Cho AY. *Single-mode surface-plasmon laser*. Applied physics letters. 2000 Apr 17;76(16):2164-6.

[77] L. V. Blake and M. W. Long, *Antennas: Fundamentals, design, measurement*. IET Digital Library, 2009. 978-1-61353-104-4

[78] “IEEE Standard for Rectangular Metallic Waveguides and Their Interfaces for Frequencies of 110 GHz and Above–Part 1: Frequency

Bands and Waveguide Dimensions," *IEEE Std 17851-2012*, pp. 1–22, Mar. 2013, doi: 10.1109/IEEESTD.2013.6471987.

[79] "Waveguide Modes: TE TM TEM » Electronics Notes." https://www.electronics-notes.com/articles/antennas-propagation/rf-feeders-transmission-lines/waveguide-modes-te-tm-tem.php (accessed Apr. 12, 2020).

[80] J. H. Davies, *The Physics of Low-dimensional Semiconductors: An Introduction*. Cambridge University Press, 1997. 978-1-107-39346-2

[81] Y. Zeng, B. Qiang, and Q. J. Wang, "Photonic Engineering Technology for the Development of Terahertz Quantum Cascade Lasers," *Adv. Opt. Mater.*, vol. 8, no. 3, p. 1900573, 2020, doi: 10.1002/adom.201900573.

[82] G. Liang, T. Liu, and Q. J. Wang, "Recent Developments of Terahertz Quantum Cascade Lasers," *IEEE J. Sel. Top. Quantum Electron.*, vol. 23, no. 4, pp. 1–18, Jul. 2017, doi: 10.1109/JSTQE.2016.2625982.

[83] S. Kumar, C. W. I. Chan, Q. Hu, and J. L. Reno, "Two-well terahertz quantum-cascade laser with direct intrawell-phonon depopulation," *Appl. Phys. Lett.*, vol. 95, no. 14, p. 141110, Oct. 2009, doi: 10.1063/1.3243459.

[84] M. Franckié, L. Bosco, M. Beck, E. Mavrona, and J. Faist, "Optimization and Fabrication of Two-Quantum Well THz QCLs Operating Above 200 K," in *2019 Conference on Lasers and Electro-Optics (CLEO)*, May 2019, pp. 1–2, doi: 10.1364/CLEO_SI.2019.SW4F.1.

[85] C. Gmachl, F. Capasso, D. L. Sivco, and A. Y. Cho, "Recent progress in quantum cascade lasers and applications," *Rep. Prog. Phys.*, vol. 64, no. 11, pp. 1533–1601, Oct. 2001, doi: 10.1088/0034-4885/64/11/204.

[86] M. S. Vitiello, G. Scalari, B. Williams, and P. De Natale, "Quantum cascade lasers: 20 years of challenges," *Opt. Express*, vol. 23, no. 4, p. 5167, Feb. 2015, doi: 10.1364/OE.23.005167.

[87] M. Razeghi, "Quantum Cascade Lasers," in *Technology of Quantum Devices*, Springer US, 2010, pp. 271–319.

[88] L. Li *et al.*, "Terahertz quantum cascade lasers with> 1 W output powers," *Electron. Lett.*, vol. 50, no. 4, pp. 309–311, 2014.

[89] B. S. Williams, S. Kumar, Q. Hu, and J. L. Reno, "High-power terahertz quantum-cascade lasers," *Electron. Lett.*, vol. 42, no. 2, pp. 89–91, Jan. 2006, doi: 10.1049/el:20063921.

[90] X. Wang *et al.*, "High-power terahertz quantum cascade lasers with ~0.23 W in continuous wave mode," *AIP Adv.*, vol. 6, no. 7, p. 075210, Jul. 2016, doi: 10.1063/1.4959195.

[91] L. H. Li *et al.*, "Multi-Watt high-power THz frequency quantum cascade lasers," *Electron. Lett.*, vol. 53, no. 12, pp. 799–800, Jun. 2017, doi: 10.1049/el.2017.0662.

[92] S. Fathololoumi *et al.*, "Terahertz quantum cascade lasers operating up to ~200 K with optimized oscillator strength and improved injection tunneling," *Opt. Express*, vol. 20, no. 4, pp. 3866–3876, Feb. 2012, doi: 10.1364/OE.20.003866.

[93] Q. Lu and M. Razeghi, "Recent Advances in Room Temperature, High-Power Terahertz Quantum Cascade Laser Sources Based on Difference-Frequency Generation," *Photonics*, vol. 3, no. 3, Art. no. 3, Sep. 2016, doi: 10.3390/photonics3030042.

[94] C. Deutsch *et al.*, “Terahertz quantum cascade lasers based on type II InGaAs/GaAsSb/InP,” *Appl. Phys. Lett.*, vol. 97, no. 26, p. 261110, Dec. 2010, doi: 10.1063/1.3532106.

[95] M. Fischer *et al.*, “Scattering processes in terahertz InGaAs/InAlAs quantum cascade lasers,” *Appl. Phys. Lett.*, vol. 97, no. 22, p. 221114, Nov. 2010, doi: 10.1063/1.3504251.

[96] K. Ohtani, M. Beck, G. Scalari, and J. Faist, “Terahertz quantum cascade lasers based on quaternary AlInGaAs barriers,” *Appl. Phys. Lett.*, vol. 103, no. 4, p. 041103, Jul. 2013, doi: 10.1063/1.4816352.

[97] D. J. Paul, “The progress towards terahertz quantum cascade lasers on silicon substrates,” *Laser Photonics Rev.*, vol. 4, no. 5, pp. 610–632, 2010, doi: 10.1002/lpor.200910038.

[98] A. Khalatpour, A. K. Paulsen, C. Deimert, Z. R. Wasilewski, and Q. Hu, “High-power portable terahertz laser systems,” *Nat. Photonics*, pp. 1–5, Nov. 2020, doi: 10.1038/s41566-020-00707-5.

[99] M. Brandstetter *et al.*, “High-power THz quantum cascade lasers,” in *High Power Diode Lasers and Systems Conference (HPD), 2015 IEEE*, 2015, pp. 5–6, Accessed: May 22, 2017. [Online]. Available: http://ieeexplore.ieee.org/abstract/document/7439667/.

[100] A. W. M. Lee, Q. Qin, S. Kumar, B. S. Williams, Q. Hu, and J. L. Reno, “High-power and high-temperature THz quantum-cascade lasers based on lens-coupled metal-metal waveguides,” *Opt. Lett.*, vol. 32, no. 19, pp. 2840–2842, 2007.

[101] L. Ajili *et al.*, “Continuous-wave operation of far-infrared quantum cascade lasers,” *Electron. Lett.*, vol. 38, no. 25, pp. 1675–1676, Dec. 2002, doi: 10.1049/el:20021143.

[102] S. Fan, Y. He, B. S. Ung, and E. Pickwell-MacPherson, “The growth of biomedical terahertz research,” *J. Phys. Appl. Phys.*, vol. 47, no. 37, p. 374009, 2014, doi: 10.1088/0022-3727/47/37/374009.

[103] Han YJ, Li LH, Zhu J, Valavanis A, Freeman JR, Chen L, Rosamond M, Dean P, Davies AG, Linfield EH. *Silver-based surface plasmon waveguide for terahertz quantum cascade lasers*. Optics express. 2018 Feb 19;26(4):3814-27.

[104] Kundu I. *Frequency tunable terahertz quantum cascade lasers* (Doctoral dissertation, University of Leeds).

[105] C. D. Farmer, C. R. Stanley, C. N. Ironside, and M. Garcia, “Improved GaAs-based quantum cascade laser (∼11 [micro sign]m) using high-reflectivity metal facet coating,” *Electron. Lett.*, vol. 38, no. 23, p. 1443, 2002, doi: 10.1049/el:20020988.

[106] B. S. Williams, S. Kumar, H. Callebaut, Q. Hu, and J. L. Reno, “Terahertz quantum-cascade laser at λ≈100 μm using metal waveguide for mode confinement,” *Appl. Phys. Lett.*, vol. 83, no. 11, pp. 2124–2126, Sep. 2003, doi: 10.1063/1.1611642.

[107] R. Khabibullin *et al.*, “Silver-based double metal waveguide for terahertz quantum cascade laser,” p. 35, Mar. 2019, doi: 10.1117/12.2521774.

[108] “Quantum-limited frequency fluctuations in a terahertz laser | Nature Photonics.” https://www.nature.com/articles/nphoton.2012.145 (accessed Jun. 18, 2021).

[109] A. J. L. Adam *et al.*, “Beam patterns of terahertz quantum cascade lasers with subwavelength cavity dimensions,” *Appl. Phys. Lett.*, vol. 88, no. 15, p. 151105, Apr. 2006, doi: 10.1063/1.2194889.

[110] A. Valavanis *et al.*, “Mechanically robust waveguide-integration and beam shaping of terahertz quantum cascade lasers,” *Electron. Lett.*, vol. 51, no. 12, pp. 919–921, Jun. 2015, doi: 10.1049/el.2015.1137.
[111] M. I. Amanti, M. Fischer, G. Scalari, M. Beck, and J. Faist, “Low-divergence single-mode terahertz quantum cascade laser,” *Nat. Photonics*, vol. 3, no. 10, Art. no. 10, Oct. 2009, doi: 10.1038/nphoton.2009.168.
[112] N. Yu *et al.*, “Designer spoof surface plasmon structures collimate terahertz laser beams,” *Nat Mater*, vol. 9, no. 9, pp. 73–735, 2010, doi: 10.1038/nmat2822.
[113] A. Wei Min Lee, Q. Qin, S. Kumar, B. S. Williams, Q. Hu, and J. L. Reno, “High-power and high-temperature THz quantum-cascade lasers based on lens-coupled metal-metal waveguides,” *Opt. Lett.*, vol. 32, no. 19, p. 2840, Oct. 2007, doi: 10.1364/OL.32.002840.
[114] M. I. Amanti, M. Fischer, C. Walther, G. Scalari, and J. Faist, “Horn antennas for terahertz quantum cascade lasers,” *Electron. Lett.*, vol. 43, no. 10, pp. 573–574, May 2007, doi: 10.1049/el:20070450.
[115] B. N. Ellison *et al.*, “3.5 THz quantum-cascade laser emission from dual diagonal feedhorns,” *Int. J. Microw. Wirel. Technol.*, vol. 11, no. 9, pp. 909–917, Nov. 2019, doi: 10.1017/S175907871900028X.
[116] “Microwave Horn Antenna » Electronics Notes.” https://www.electronics-notes.com/articles/antennas-propagation/horn-antenna/basics-primer.php (accessed Aug. 05, 2020).
[117] Z. Dong, H. Lu, Y. Liu, B. Li, and X. Lv, “Designs of Multilayer Corrugated Horn for Terahertz Application,” in *2018 International Conference on Microwave and Millimeter Wave Technology (ICMMT)*, Chengdu, May 2018, pp. 1–3, doi: 10.1109/ICMMT.2018.8563508.
[118] D. A. Montofré *et al.*, “High-Performance Smooth-Walled Horn Antennas for THz Frequency Range: Design and Evaluation,” *IEEE Trans. Terahertz Sci. Technol.*, vol. 9, no. 6, pp. 587–597, Nov. 2019, doi: 10.1109/TTHZ.2019.2938985.
[119] B. N. Ellison *et al.*, “3.5-THz quantum-cascade laser emission from dual diagonal feedhorns,” in *12th European Conference on Antennas and Propagation (EuCAP 2018)*, London, UK, 2018, p. 248 (4 pp.)-248 (4 pp.), doi: 10.1049/cp.2018.0607.
[120] M. A. Belkin *et al.*, “Terahertz quantum cascade lasers with copper metal-metal waveguides operating up to 178 K,” *Opt. Express*, vol. 16, no. 5, pp. 3242–3248, Mar. 2008, doi: 10.1364/OE.16.003242.
[121] “- ANSYS Help.” https://ansyshelp.ansys.com/ (accessed Jan. 07, 2020).
[122] F. T. Ulaby, *Fundamentals of applied electromagnetics*. Upper Saddle River, N.J: Prentice Hall, 1997.
[123] K. Okamoto, *Fundamentals of Optical Waveguides*. Academic Press, 2006.